THE DEVELOPMENT OF PVD COATINGS FOR PEM FUEL CELL BIPOLAR PLATES

by

PHILIP JOHN HAMILTON

A thesis submitted to the University of Birmingham for the degree of

DOCTOR OF PHILOSOPHY

School of Chemical Engineering

College of Engineering & Physical Sciences

University of Birmingham

B15 2TT, United Kingdom

September 2013

ABSTRACT

This work investigated the suitability of thin film, single and multi-layered coatings, by a Physical Vapour Deposition (PVD) process for polymer electrolyte membrane fuel cell bipolar plates. Due to the multifunctional nature of this particular component a comprehensive approach was used where several key properties were examined for coatings including: ZrN, TiN, CrN, Graphit-iC™, CrN+C, TiN+C and Au.

Chemical etching and surface roughness were found to influence the Interfacial Contact Resistance (ICR) of the substrate; however, any observed effect was negated with the addition of a conductive coating. CrN+C and TiN+C multi-layer coatings showed a striking reduction in the ICR compared with the nitride only equivalents.

The suitability of pre-coated PVD coatings for serial production via stamping was assessed in collaboration with an industrial partner. The coating durability was found to be influenced by several factors including coating type, thicknesses and position on stamped plate. The multi-layered TiN+C coating was found to noticeably improve the stampability compared to the TiN only coating.

The corrosion resistance of the coatings was evaluated under simplified corrosion conditions. Under these conditions TiN+C was found to have two beneficial effects, improving the free corrosion potential and the stability of the carbon topcoat under startup/shutdown potentials.

ACKNOWLEDGEMENTS

There are a number of individuals, organisations and companies that I would like to acknowledge and express my appreciation to, without whom, it would not have been possible to submit this work.

I would like to thank my various academic and industrial supervisors for their guidance and encouragement over the course of my PhD; Kevin Cooke, Waldemar Bujalski, Hanshan Dong and Bruno Pollet. My thanks also to Alison Davenport for her helpful discussions.

My thanks to Birmingham University and the Engineering and Physical Sciences Research Council (EPSRC) for their generous financial support. To the Hydrogen & Fuel Cells Doctoral Training Center (DTC) research group for providing an enjoyable atmosphere to study in and an insightful forum for discussion from differing disciplinary points of view. To Leeds EPSRC Nanoscience and Nanotechnology Research Equipment Facility (LENNF), particularly Alex Walton for his invaluable experience in the interpretation of XPS and the National EPSRC XPS Users' Service (NEXUS). To the Midlands Energy Graduate School (MEGS) for travel grant funding. The Confocal Raman Microscope, Atomic Force Microscope, and Interferometer used in this research were obtained, through Birmingham Science City: Innovative Uses for Advanced Materials in the Modern World (West Midlands Centre for Advanced Materials Project 2), with support from Advantage West Midlands (AWM) and part funded by the European Regional Development Fund (ERDF). My special thanks to James Bowen for his assistance with this equipment and helpful conversations. To

David Aspinwall, Leung Sein Soo, Richard Hood and Richard Fasham from the Micromachining group.

My thanks to various companies; first and foremost, to Teer Coatings Ltd. (part of the Miba Coatings Group) for their sponsorship and facilities. Particularly Kevin Cooke, Hailin Sun, Sue Fields and Shicai Yang for their helpful discussions and providing a range of coated samples. To Graham Murray and the staff at Bac2 Ltd. for the use of their facilities. To Mick Taylor from Precision Micro Ltd. for organising some photochemically etched samples and to Rowan Crozier and Mark Fenney from Brandauer Ltd. for organising the stamping work.

Penultimately, I would also thank my family and friends for their support and encouragement throughout the years. Particularly to my wife, who has always helped put things in perspective in the turbulent days of my PhD. Finally, and most importantly my thanks to God, for there is nothing that I have done that He has not graciously enabled me to achieve.

LIST OF PUBLICATIONS & PRESENTATIONS

P.J. Hamilton & B.G. Pollet, *Review of Polymer Electrolyte Membrane Fuel Cell (PEMFC) Flow Field Plates: Design, Materials and Characterisation*. Fuel Cells, 2010, 10, 4, 489-509.

P.J. Hamilton, B.G. Pollet & K. Cooke, *Development of Bipolar Plate Coatings for PEM Fuel Cell Applications*, 7th Annual International Conference Partnering & Exhibition: Generating the Hydrogen & Fuel Cell Society, 30th March 2011, NEC, Birmingham, UK

(P.J. Hamilton & B.G. Pollet), L. Kühnemann, T. Derieth, P. Beckhaus, A. Heinzel, *PEM Fuel Cell Failure mode analysis, Ch 6 - Degradation of Bipolar Plates and Its Effect on PEM Fuel Cells*. Edited by Xiao-Zi Yuan, CRC Press, 2011, ISBN: 978-1-4398-3917-1, 143-150.

P.J. Hamilton, W. Bujalski, H. Dong and K. Cooke, *The Development of Bipolar Plate Coatings for PEM Fuel Cell Applications*, 8th Annual International Conference Partnering & Exhibition: Generating the H_2 & Fuel Cell Society, 29th March 2012, NEC, Birmingham, UK

H. Sun, K. Cooke, G. Eitzinger, P. Hamilton, B. Pollet, *Progress towards, thin, cost-effective coatings for PEMFC metallic Bipolar Plates by closed field unbalanced magnetron sputter ion plating,* Technoport - Bipolar Plates for PEM fuel cells, 15-17th April 2012, Trondheim, Norway

P.J. Hamilton, W. Bujalski, H. Dong and K. Cooke, *Factors affecting the Interfacial Contact Resistance and the corrosion resistance of PVD coated Bipolar Plates for PEM Fuel Cells*, 19th World Hydrogen Energy Conference, 3-7th June 2012, Toronto, Canada

H. Sun, K. Cooke, G. Eitzinger, P. Hamilton & B. Pollet. *Development of PVD coatings for PEMFC metallic bipolar plates.* Thin Solid Films, 2012, 528, 199-204.

K. Cooke, H. Sun, S. Field, G. Eitzinger & P. Hamilton, *Closed Field Unbalanced Magnetron Sputter Ion Plating of high performance coatings on PEMFC metallic bipolar plates,* 13th International Conference on Plasma Surface Engineering, 10-14th September 2012, Garmisch-Partenkirchen, Germany

GLOSSARY OF TERMS AND ABBREVIATIONS

AFM

Atomic Force Microscopy

AST

Accelerated Stress Test (used to reduce the time needed for screening materials)

BOP

Balance of Plant. This includes other components needed to operate a PEMFC stack such as humidifiers, blowers and gas controllers etc.

BPP

Bipolar Plate (also known as a flow field plate, separator plate or current collector)

CFUBMSIP

Closed Field Unbalanced Magnetron Sputter Ion Plating

E_{corr} (V)

The potential difference of a metal in solution where the rate of anodic metal dissolution is equal to the rate of the cathodic reduction reactions of hydrogen and/or oxygen.

EDX / EDS

Energy dispersive X-ray Spectroscopy

***η* (V)**

Overpotential. The difference between the observed potential and the reversible potential.

GDL

Gas Diffusion Layer

***F* (C mol^{-1})**

Faraday Constant (96485 C mol^{-1})

GDOES / GDS

Glow Discharge Optical Emission Spectroscopy

HOR

Hydrogen Oxidation Reaction, $H_2 \rightarrow 2H^+ + 2e^-$

I_{corr} (A cm^{-2})

Corrosion current density

ICR (mΩ cm^2)

Interfacial Contact Resistance

LSV

Linear Sweep Voltammogram

MEA

Membrane Electrode Assembly

MSE

Mercury Sulphate Electrode (MSE) (0.68 V/RHE)

Nafion®

A sulfonated tetrafluoroethylene based fluoropolymer-copolymer that is conductive to cations, but not to anions or electrons. Nafion® is widely seen as the 'standard' polymer electrolyte membrane material for PEMFCs.

ORR

Oxygen Reduction Reaction, $\frac{1}{2}O_2 + 2H^+ + 2e^- \rightarrow H_2O$

PEMFC

Polymer Electrolyte Membrane Fuel Cell also known as a Proton Exchange Membrane Fuel Cell

PVD

Physical Vapour Deposition

SEM

Scanning Electron Microscope

RHE

Reversible Hydrogen Electrode

XPS

X-Ray Photoelectron Spectroscopy

TABLE OF CONTENTS

INDEX OF FIGURES

INDEX OF TABLES

CHAPTER 1
INTRODUCTION

Includes extracts from P.J. Hamilton, M. Res. Thesis – *Hydrogen sorption in palladium doped microporous materials*, University of Birmingham. Reprinted by permission.

1 INTRODUCTION

This chapter examines the growing pressures to transition from an energy economy fundamentally based on fossil fuels, towards one based on low carbon technologies and sustainability. The challenge of implementing hydrogen in such an energy economy and its utilisation via fuel cells is then discussed. Finally, the state of the art of automotive Polymer Electrolyte Membrane Fuel Cells (PEMFCs) is outlined and current targets are highlighted, including those of the bipolar plate.

1.1 The Necessity of an Energy Economy Transition

There is a diverse range of drivers for a fundamental change in the way we use energy.

First, there is the issue of resource depletion. World oil consumption continued to increase in 2010 and was ~87 million barrels per day. There are many “peak oil” models that predict the maximum rate of global oil production, after which, the production enters into terminal decline. Many of these suggest that we are already at, or have very nearly reached peak oil. A report in 2009 by the UK Energy Research Council (UKERC) reviewed over 500 studies, analyses of industrial databases and comparisons of global supply forecasts. They proposed that a peak in conventional global oil production before 2030 appears likely and there is a significant risk of a peak before 2020 [1]. A process called “fracking” has recently been proposed as an alternative solution to retrieve significant quantities of gas and oil reserves from shale deposits, which were previously considered to be unreachable. However, even if this route should provide significant quanities, it would only appear to postpone the inevitable and does little to address the other drivers for change.

A second issue which is linked to the first, is the issue of security of supply. Fossil fuel resources such as coal, gas and oil are not uniformly distributed across the world. This creates a dependence of some countries on others for energy. The changeable energy policies of distributing governments are not conducive for a long term and secure supply of fossil fuels. Historical instability in oil rich countries and the arguable use of resources for political influence encourage feelings of energy insecurity and increase cost.

Thirdly, climate change. The intergovernmental panel on climate change (IPCC) has suggested that global green house gas (GHG) emissions due to human activities have grown since pre-industrial times by 70% between 1970 and 2004 [2]. Although the atmospheric CO_2 levels do naturally rise and fall, the current concentrations of 387 ppm determined from ice cores far exceed the natural range of the past 750,000 years [3]. While climate predictions are dependent on the climate model used and assumptions made about future global emissions, the IPCC estimates a global average temperature rise of 1.8 - 4°C this century [2] and suggests increasing statistical confidence in projected increases in extremes of weather such as droughts, heat waves and floods. Consequently in the UK, the Climate Change Act of 2008 has put GHG emission reductions into law. CO_2 emissions make up the majority (85%) of the UK GHG emissions and this bill includes a commitment to reduce them by 60% by 2050 and 26-32% by 2020 compared with 1990 levels [4]. All other GHGs are to be reduced by 32-37% by 2020. This legislation should drive investment in low carbon technologies and in a low carbon energy economy.

Penultimately, there are concerns, especially in cities, over the impacts on health from air pollution caused by fossil fuel combustion. Air pollution including carbon monoxide (CO), sulphur oxides (SO_x), nitrogen oxides (NO_x), ozone (O_3) and particulate matter (PM) have been linked to cardiovascular and respiratory illnesses [5]. Continued global warming may increase the spread of disease due to elevated temperatures and through damaged sanitation systems by extreme weather events. As a result global warming, rising sea levels would pose a serious risk to both developed and undeveloped coastal populations alike.

Finally, economics. In 2007, the UK government conducted the Stern Review [6] on the economics of climate change. It concluded firstly that the benefits of strong, early action on climate change outweigh the financial costs of doing nothing now, and secondly that the worst economic impacts of climate change can only be avoided if strong action is taken immediately. Furthermore, due to resource depletion, the cost of fossil fuel resources is very likely to increase, promoting the adoption of alternative options which have previously been hindered by the high cost associated with new technology.

1.2 The Suitability of Hydrogen?

Many have long proposed using hydrogen as an energy vector in a future energy economy. This is because there are potentially abundant supplies and it can be used to store large amounts of energy, which can be released cleanly without harmful emissions through fuel cells. These qualities make hydrogen particularly attractive when considering the drivers for change as previously mentioned. The adoption of hydrogen from production to utilisation in the energy economy is dependent on overcoming a number of interdisciplinary challenges.

Although there are large quantities of hydrogen in the world, this resource naturally exists being bonded to other elements, rather than as a free gas. There are a variety of ways in which hydrogen can be produced. The production of hydrogen is currently achieved primarily through the steam reformation of natural gas, although other heavier hydrocarbons can also be used via gasification processes. Whilst this process is relatively cheap, it also produces carbon monoxide and carbon dioxide as well as maintaining our dependence on fossil fuels. Further purification of the hydrogen may be required as particular types of hydrogen fuel cells such as PEMFC need very high purity hydrogen because impurities such as carbon monoxide or sulphur will poison the catalyst membrane. Electrolysis of water to produce oxygen and very pure hydrogen is now commercially available, although the source of the electricity (i.e. renewables or fossil fuels) is fundamental in determining whether this route will actually reduce our dependence on fossil fuels and carbon emissions. Biological methods such as photosynthesis and anaerobic digestion can also be used although these methods tend to need vast surface areas, carefully controlled conditions, have low production rates and are not generally carried out on an industrial scale. Finally, hydrogen can also be produced as a by-product from industrial processes, such as those used in the chlor-alkali sector.

Hydrogen has an excellent gravimetric energy density of 120 MJ/kg due to its nature as gas at room temperature. However, the volumetric energy density under these conditions is substantially poorer with 1 kg of H_2 occupying ~11 m^3. To put this in perspective, about 4 kg (i.e. 44 m^3) of stored hydrogen would be necessary to fuel a small car for 400 km. As a result, a means by which the hydrogen molecules can be packed more closely is needed. The ideal hydrogen storage solution would have good gravimetric and volumetric density, equilibrium properties near ambient temperature and pressure, reversibility over many cycles and fast transfer rates. Further storage material considerations are stability in air, recycling and cost. Current solutions include storing hydrogen as a compressed gas, a super cooled liquid or by ad/absorbing in solids such as high surface area materials or metal hydrides. An alternative to the direct storage of hydrogen has been suggested by Zuttel et al. [7] who have proposed the development of higher energy density synthetic fuels based on hydrogen such as NH_3 or C_8H_{18} which would be easier to store as liquids but may require further processing before being used in fuel cells.

The UK currently uses a centralised distribution system for natural gas where it is produced and stored at comparatively few sites and then distributed to many consumers via gas pipelines. This is an option for hydrogen, but only at relatively low concentrations (~4%). Currently, hydrogen is primarily transported via the transport network, but this adds to the carbon cost. Alternatively, a more decentralised model could be used where hydrogen is produced on-site where it is needed from either the reformation of natural gas from existing pipelines or via electrolysis of water. The carbon footprint of these two methods would obviously depend on the source of the natural gas and electricity.

As with all fuels that are capable of carrying large amounts of energy, there are important safety concerns that need to be addressed. The disadvantages of hydrogen as a fuel are it has very wide explosive limit in air, a low ignition energy, it burns with a clear flame in daylight and has high leak rates. The advantages of hydrogen are that it has a very low density that means it will disperse rapidly away from the source of a leak and will not pool as a liquid or heavier gas fuels would. Hence, the concentration levels for ignition or detonation are less likely to be reached provided adequate ventilation is provided. Additionally, sociologically speaking, the ‘Hindenburg’ and ‘Hydrogen bomb’ still often come to the mind of the general public when thinking of hydrogen. Changing public perception by increasing awareness of the different dangers associated with hydrogen still needs to be properly addressed before hydrogen is likely to be widely accepted.

Currently, the vast majority of hydrogen is either used in agriculture in the production of ammonia for fertilizer or in the oil industry to convert heavy crude oil distillation fractions to lighter hydrocarbons via hydrocracking. The use of hydrogen in the future may include long-term energy storage for balancing varying supply and demand of electricity from low carbon/renewable energy sources using an electrolyser. Additionally, it could also be used as a replacement for fossil fuels in the transport and domestic sectors through the implementation of hydrogen fuel cells. Fuel cells are electrochemical devices that continuously convert chemical energy (from fuel and oxidant) into electrical energy without the production of harmful emissions. There are multiple types of fuel cell, which are distinguished by their use of different electrolyte materials as shown in Table 1.1 below.

Table 1.1 Types of fuel cell

Type	Electrolyte	Anode / Cathode Gas	Operating Temperature (°C)	Efficiency (%)
Proton Exchange Membrane (PEMFC)	Polymer Membrane (water based)	H_2 / O_2	75	35 - 60
High Temperature PEMFC (HT-PEMFC)	Polymer Membrane (acid based)	H_2 / O_2	120-200	60
Alkaline (AFC)	Potassium Hydroxide	H_2 / Pure O_2	<80	50 - 70
Direct Methanol (DMFC)	Polymer Membrane	Methanol / O_2	75	35 - 40
Phosphoric Acid (PAFC)	Phosphoric Acid	H_2 / O_2	210	35 - 50
Molten Carbonate (MCFC)	Alkali Carbonates	H_2 / O_2	650	40 - 55
Solid Oxide (SOFC)	Ceramic Oxides	H_2 / O_2	600-1000	45 - 60

The selection of the fuel cell type is broadly dependent on the application and requirements such as start up times, load profile, availability/purity of fuel and so forth. This work will focus exclusively on PEMFCs and the development of PVD coated metal bipolar plates, which are particularly suited to automotive applications where power density is paramount.

1.3 Polymer Electrolyte Membrane Fuel Cells

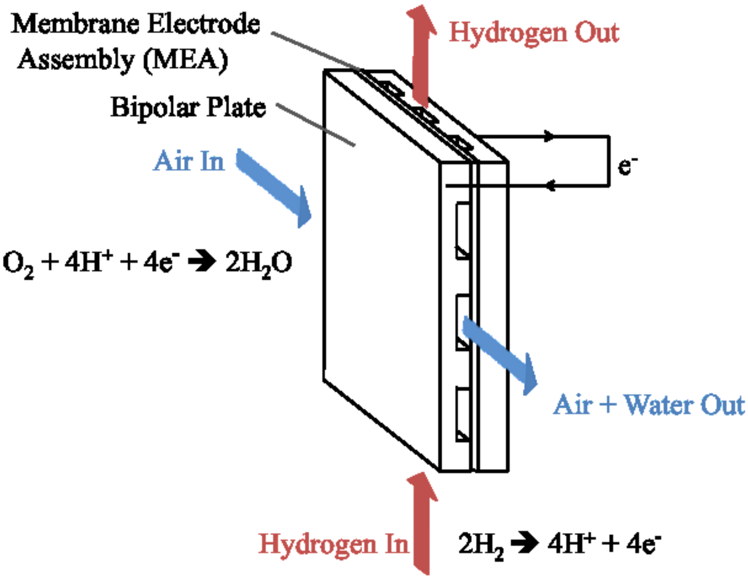

Figure 1.1 A simplified hydrogen fuel cell

At the core of a Polymer Electrolyte Membrane Fuel Cell (PEMFC) is the Membrane Electrode Assembly (MEA). It consists of a sandwich of three different types of materials. The polymeric proton exchange membrane is located in the middle and is typically made from a perfluorosulfonic acid (PFSA) such as Nafion®. These membranes require humid conditions to function as proton conductivity decreases with decreasing humidity. Two catalyst layers (historically made from platinum) are situated immediately either side of the membrane to carry out the hydrogen oxidation reaction (HOR) and oxygen reduction reactions (ORR). Due to the scarcity and cost of platinum, much work has been carried out to reduce the loading required and develop alternative catalysts such as bimetallic core-shell structured nanoparticles. The final component of the MEA is the gas diffusion layer (GDL) which is normally made of carbon paper or carbon cloth. They allow the flow of reactants to the catalysts, electrically connecting the carbon supported catalyst with the bipolar plate and facilitating water management. The thickness, porosity, permeability and the wetting characteristics of the pores are important parameters that affect the performance of the cell. The two traditional approaches of manufacturing the MEA are the Catalyst Coated Membrane (CCM) and Catalyst Coated Substrate (CCS) techniques.

With zero emissions in an emissions conscious climate and low operating temperatures, one of the most promising applications for PEMFC technology is in the automotive sector where trials of buses, cars and motorcycles are becoming increasingly common. Global automotive companies including Daimler-Mercedes, Honda, Toyota, Hyundai-Kia, General Motors, Ford, Nissan-Renault, are all carrying out extensive research and development [8].

Figure 1.2 The 5th Fuel Cell Electric Vehicle Drive 'n' Ride in Strasbourg demonstrating six different models of fuel cell electric cars by Daimler, Honda, Hyundai, Intelligent Energy, General Motors and Toyota. Photo courtesy of FTI Consulting

There is also some collaboration between companies such as the Automotive Fuel Cell Cooperation (AFCC) between Daimler, Ford, Ballard and NuCellSys. This is likely to be due to the perception that mass-market volumes and returns on investment are still some way off and consequently that collaboration enables the risk and cost of entering the market to be shared. Other automotive companies appear to importing fuel cell expertise such as SMILE

FC System Corporation, a joint venture between Suzuki and Intelligent Energy Ltd. Most automotive manufacturers have stated their intention to release commercial hydrogen fuel cell cars by the thousands in 2015-17 in areas with sufficient infrastructure. Smaller UK companies also involved in the integration of fuel cells for transport applications include Riversimple LLP and Microcab. In the UK, the H_2 Mobility Project which is a collaboration between three UK government departments and industrial participants from the utility, gas, infrastructure and global car manufacturing sectors has recently started to investigate the potential for hydrogen as a fuel for ultra-low carbon vehicles in the UK before continuing to develop an action plan for an anticipated roll-out to consumers in 2015.

As the performance of PEMFCs for automotive applications is now sufficient, the remaining challenges are cost and durability which still need to be improved if they are to compete successfully with the incumbent combustion technology. In 2010, the projected cost (production of 500,000 units) of an 80 kW hydrogen fuel cell power system for transportation was 51 $\$kW^{-1}$, which is an 80% drop from 2005 [9]. The target for 2015 aims to match the current figure for a conventional internal combustion engine of 30 $\$kW^{-1}$. In terms of durability, the current DoE target for automotive applications is 5000 hrs (equivalent to 150,000 miles) which includes an estimated 17,000 start/stop cycles, 1,650 frozen cycles and 1,200,000 load cycles [10]. Obviously the bipolar plate, as an essential part of the fuel cell, must also be both cost effective and sufficiently durable in order to meet these requirements as well. Therefore this work will focus on the development and characterisation of suitable coatings by physical vapour deposition (PVD) for PEM fuel cell metal bipolar plates.

CHAPTER 2

BIPOLAR PLATES

Includes extracts from P.J. Hamilton & B.G. Pollet, *Review of Polymer Electrolyte Membrane Fuel Cell (PEMFC) Flow Field Plates: Design, Materials and Characterisation*. Fuel Cells, 2010, 10, 4, 489-509. Reprinted by permission.

2 BIPOLAR PLATES

This chapter examines the importance of the bipolar plate in a Polymer Electrolyte Membrane Fuel Cell (PEMFC). The bipolar plate design, materials, manufacture and characterisation are all addressed. This section culminates with a particular focus on coated metallic bipolar plates and the role of PVD coatings. Based on this review chapter the aims of this work are then put forward.

2.1 Introduction to Bipolar Plates

The bipolar plate is also known as the flow field plate or the separator plate. In a traditional stack arrangement the bipolar plates are located either side of the Membrane Electrode Assembly (MEA). They have numerous functions to perform which have a dramatic impact on PEMFC performance. These include:

- Separating gases between cells
- Providing a conductive medium between the anode and cathode
- Providing a flow field channel for even distribution of reaction gases (and potentially coolant)
- Providing a solid structure for the stack
- Facilitating water and heat management

Due to the multifunctional nature of the bipolar plate, suitable properties such as electrical conductivity, corrosion resistance, mechanical strength, gas impermeability, ease of manufacture and low cost are required. The US Department of Energy (DoE) has proposed performance targets for flow field plate properties as listed in Table 2.1.

Table 2.1 US Department of Energy (DoE) Targets for Bipolar Plates [11]

Properties	Units	2011 status	2017	2020
Cost (based on 2002 \$, 500,000 stacks per year)	\$/kW	5-10	3	3
H_2 Permeability (at 80 °C & 3 atm.)	Std $cm^3/(sec\ cm^2Pa)$ @ 80°C, 3 atm, 100% RH	N/A	$<1.3\ x10^{-14}$	$<1.3\ x10^{-14}$
Corrosion, Anode	$\mu A/cm^2$	<1	<1	<1
Corrosion, Cathode	$\mu A/cm^2$	<1	<1	<1
Electrical conductivity	S/cm	>100	>100	>100
Area specific resistance at 200 psi (138 N/cm^2)	$m\Omega\ cm^2$	30	20	10
Flexural strength	MPa	>34	>25	>25
Forming elongation	%	20-40	40	40

Whilst it is helpful to have target properties relating to the bipolar plate function, the methodology or conditions under which these targets are to be met has not always been clearly defined such as the corrosion conditions. Forming elongation has only recently been added to the DoE bipolar plate targets and corresponds to materials' suitability for stamping. The mechanical properties of materials and especially any surface coatings, has typically not been addressed in the literature.

2.1.1 *Fuel cell stack contribution*

The cost, weight and volume of the bipolar plate as a proportion of a fuel cell stack is highly sensitive to large number of factors not only of the plate itself but also the other components of the stack. Due to the wide range of factors, studies are not easily comparable and there is a wide range in relative cost and weight in the literature, as shown in Table 2.2.

Table 2.2 Bipolar plate relative cost and weight as a percentage of a PEMFC stack

Authors	Material	% of Stack Cost	% of Stack Weight	Stack Power (kW)
Woodman et al. [12]	Graphite	-	88	33
	Coated metal	-	81	33
Bar-On et al. [13] (ADL & DTI cost models)	Injection moulded graphite composite	15	-	50
	Stamped stainless steel	29	-	63
Jeong & Oh [14]	Not specified	68	90	-
Tsuchiya & Kobayashi [15]	Not specified (\$1650/m^2)	45	79	50
Jayakumar et al.[16]	Graphite (\$500/m^2)	37	55	1
	Graphite (\$100/m^2)	11	53	1
Kamarudin et al.[17]	Not specified \$1650/m^2	38	-	5
Average	-	34.7	74.3	-

Although these studies differ by some degree, all of them show that both the bipolar plate cost and weight are significant proportions of the stack. However, perhaps the most comprehensive work has been carried out by the US DoE, specifically for automotive applications. Both Directed Technologies Inc. (DTI) (now called Strategic Analysis) and TIAX LLC (TIAX) were contracted to examine the projected cost of an 80 kW$_{net}$ PEM fuel cell system manufactured at a rate of 500,000 systems per year as shown in Figure 2.1. The DTI study from 2010 estimated stack cost from stamped 316L with a proprietary coating whereas the TIAX study was based on metal bipolar plates Fe–20 Cr–4V 0.1 mm foil manufactured by progressive stamping with thermally grown chromium nitride. The TIAX scenario preliminary estimated the bipolar plate to cost to be \$6.2 kW^{-1}, however this value is still significantly higher than the 2015 DoE target of \$3 kW^{-1}.

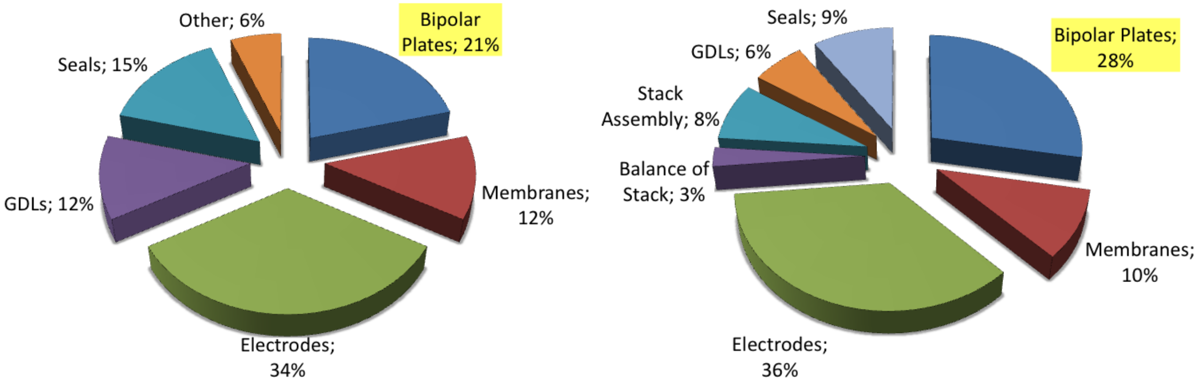

Figure 2.1 Cost distribution estimates of stack components from DTI (left) [18] and TIAX (right) [19]

2.1.2 Contribution to fuel cell losses

Although the theoretical open circuit voltage (OCV) is around 1.2 V, the actual performance of an operational fuel cell is always lower due to a number of factors as illustrated in Figure 2.2. These include activation losses, fuel crossover, internal currents, ohmic losses and mass transport losses. Activation losses are caused by the voltage required to drive the hydrogen oxidation reaction (HOR) and oxygen reduction reactions (ORR) at the anode and cathode respectively. Fuel crossover and internal currents are caused when a very small amount of hydrogen diffuses through the electrolyte from the anode to the cathode or when electron conduction occurs through the electrolyte. Both of these scenarios result in no current being produced. Ohmic losses are caused by the electrical resistance of the bipolar plate and by the resistance of ions passing through the electrolyte. Mass transport or concentration losses occur when there is reduction in the reactant concentration. This may happen as a result of the pressure drop due to the fluid resistance of gas passing along a flow channel, the reactants being drawn into the MEA or if water flooding occurs.

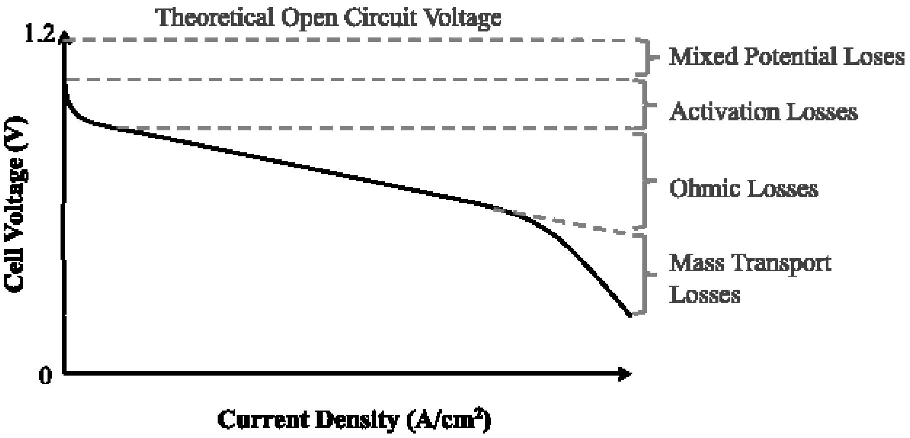

Figure 2.2 A typical I-V curve for a PEMFC showing voltage loss contributions

A practical indication of the relative contributions to the overall losses in an operating state-of-the-art automotive PEM fuel cell is shown in Figure 2.3. Although the voltage losses are dominated by the oxygen reduction reaction, the voltage losses from the interfacial contact resistance between the bipolar plate and GDL are the next most significant. Futhermore, these losses may increase over time for metal based bipolar plates as discussed later.

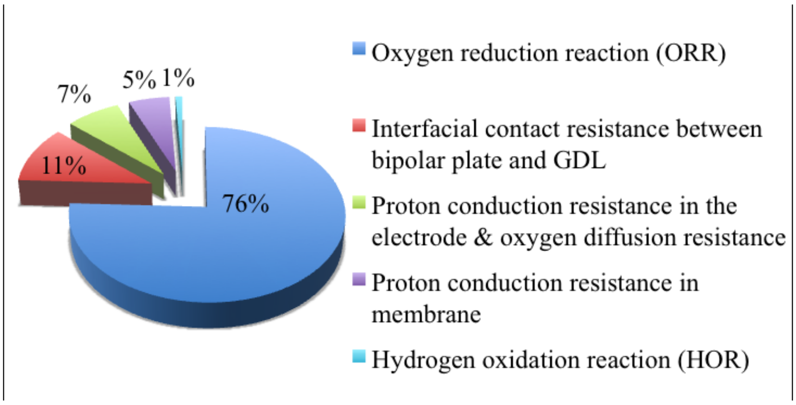

Figure 2.3 Voltage losses for Automotive PEM Fuel Cell when operating at 1.5 Acm^{-2}. 0.2/0.3 mg cm^{-2} (anode/cathode) Pt coated on an 18 µm PFSA membrane with SGL 25BC GDLs. Data from [20]

2.2 Flow Field Design

In this work it was necessary to create a flow field design for the in-situ testing of bipolar plates shown in Section 4.3. Therefore, it was important to understand how the flow field design influences the performance of a single cell. As previously mentioned, the role of the bipolar plate includes uniformly distributing the reactant gases over the MEA, providing good electrical contact with the MEA and facilitating water management. If any of these functions are impaired by the flow field design the performance of the cell will be reduced. There are three aspects to flow field design; the distribution pattern, the cross section shape and the "land" and "channel" dimensions. An review of flow field designs has been carried out by Li & Sabir [21] and more recently by Hamilton & Pollet [22].

2.2.1 Open Channel Designs

Most open channel plate designs are variations on the flow fields shown in Figure 2.4. They may also have multiple flow fields on one plate with multiple inlets and outlets. Common designs include grid/pin, spiral, straight-parallel, serpentine, and multiple serpentine.

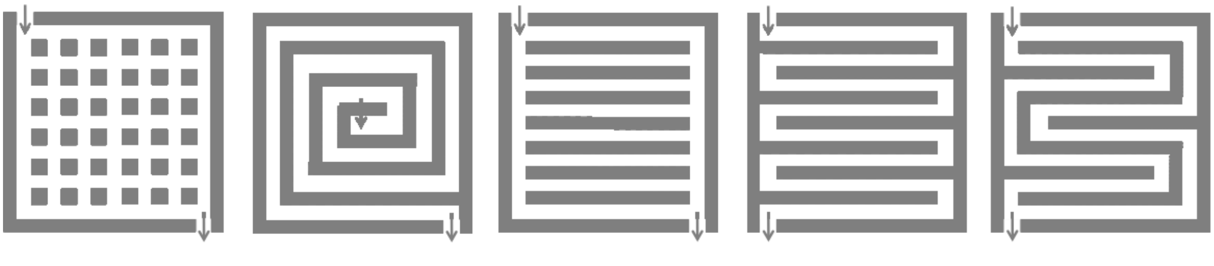

Figure 2.4 Typical flow field designs; grid/pin, spiral, straight-parallel, serpentine, and multiple serpentine

In all plate designs there is a reactant pressure drop along the direction of flow from inlet to outlet as the reactants also also move into the gas diffusion layer (GDL) by diffusion and are consumed in the MEA causing the concentration of gas along the flow channel to be reduced.

As discussed by Li & Sabir [21], using the grid/pin and parallel designs (and multiple serpentine to a certain degree), the reactant is easily distributed across the surface of the membrane because they have many paths from input to output. Hence, a low pressure is required to push the reactants through which results in lower parasitic power losses from air compression. However, this multiple path design also causes gas to flow preferentially along the path of least resistance. Any blockage, such as the formation of water droplets, may not be removed due to insufficient pressure along the blocked channel to force the water out. This blockage will result in uneven reactant distribution across the plate and reduce fuel cell performance.

In contrast, the single serpentine design only has one long flow channel with a series of alternating 180° turns for the gas to flow through. The primary benefit to this design is provided by the single channel which ensures that any water formed will be removed due to the higher pressure. Li et al. [23] have discussed some of the problems with single serpentine flow field configuration. Firstly, higher air compression pressures are required to push the gas through the long single channel resulting in high parasitic power losses. This long channel can also result in a large decrease in reactant concentration from inlet to outlet causing fluctuation in current density across the MEA area. It has also been suggested by Wang [24] that the high pressure can lead to dehydration of the membrane at the entrance of the field due to high gas pressure and flooding near the channel exit due to excessive liquid water carried downstream by the reactant gas stream.

The pressure of reactants plays a crucial role in the performance of the fuel cell. On the one hand, low air pressure is preferred to avoid to high parasitic losses. On the other, higher air pressures are preferred to ensure flooding does not occur and gas concentration remains sufficient event at the end of the flow field. The optimum pressure and best trade off is therefore the minimum pressure required to remove condensate, whilst at the same time as ensuring even reactant distribution. Variations of the serpentine pattern seem to have been developed with this trade off in mind. These consist of multiple shorter serpentine channels connected at inlet and outlet as shown previously in Figure 2.4.

2.2.2 Interdigitated Designs

An alternative "interdigitated" design has been devised by Wood et al. [25]. This flow field does not have directly connected inlet and outlet channels, but instead relies entirely on a convection mechanism where gas crosses over/under the 'land' or 'rib' of the bipolar plate and though the gas diffusion layer (GDL) into the outlet channel as shown in Figure 2.5.

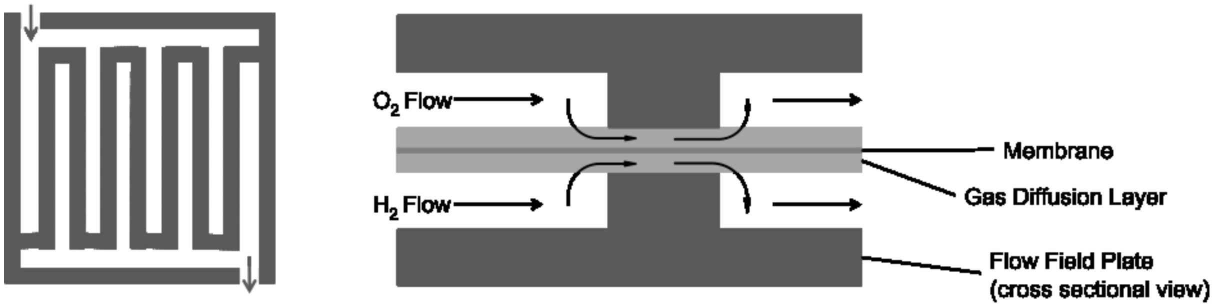

Figure 2.5 Interdigitated flow field with closed channels (left) and its convection mechanism (right)

The principal advantage of this convection mechanism also known as gas shorting is that it forces water out of the gas diffusion layer and prevents the MEA from flooding. The characteristics of the GDL such as permeability and thickness obviously have a significant impact on the effectiveness of this convection mechanism. It also requires high compression to force the gas through which may result in higher parasitic losses if used for the cathode flow field. Zhang et al. [26] compared the current distribution in standard interdigitated and single serpentine flow fields. The results showed that current distributions across the interdigitated flow field were more uniform under several different operating conditions; at very low gas flow rates, during dry gas feeding or when using over humidified reactant gases. Interdigitated flow fields performed better than serpentine flow fields with over-humidification of reactant gases but performed more poorly when the air was insufficiently humidified. The stronger water removal capability of interdigitated designs led to a higher optimum reactant gas humidification temperature compared with the serpentine design.

Park & Li [27] have identified this same convection mechanism, used by interdigitated designs, to be a significant contributor in the performance of conventional open channel serpentine flow field patterns. This mechanism occurs because the design uses a long channel with many turns which creates a high pressure gradient between adjacent channels. This in turn promotes crossover of reactants through the GDL from channel to channel. The authors also found that crossover flow was highly dependent on the GDL properties and that 3D modelling suggested that the two most important factors influencing cross flow were permeability and thickness of the GDL. This finding has also led to design of convection enhanced serpentine designs to take advantage of this effect [28].

2.2.3 Water Management

Whilst water flooding of the fuel cell is catastrophic to cell performance due to disrupted reactant flow, it is also important to take into account that the membrane must be sufficiently hydrated for proton transport to function effectively. A review of water flooding issues has been carried out by Li et al. [29] which states that water transport is affected by various operating conditions including the flow field design, gas humidification, pressure and temperature. The material wettability also plays a significant role in water management. Figure 2.6 shows typical hydrophilic and hydrophobic surfaces on which a water droplet of the same volume is placed. The hydrophilic surface with a contact angle of less than 90° takes up much more surface area, whereas the hydrophobic surface has a contact angle of more than 90° and takes up less surface area.

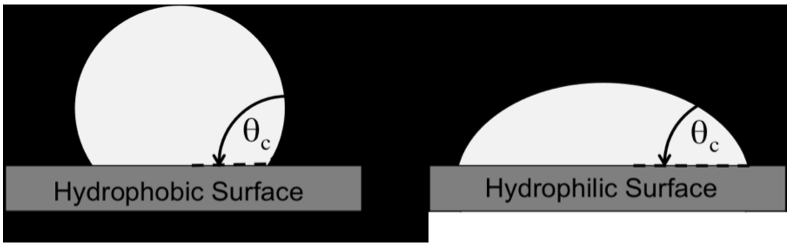

Figure 2.6 Illustration showing the difference in contact angle of two water droplets of the same volume on hydrophobic (left) and hydrophilic (right) surfaces

There have been mixed reports in the literature for the ideal water contact angle for bipolar plates. Owejan et al. [30] investigated the in-situ performance of hydrophilic (gold coated) and hydrophobic (gold coated with PTFE) bipolar plates. They found that although flow field channels with the hydrophobic coating retained more water, the distribution of smaller droplets in the channel area was found to give improved fuel cell performance especially at high current densities. In contrast, Yang et al. [31] have suggested that a hydrophilic surface may help to remove water from the GDL. As the droplet grows big enough to touch the more hydrophilic channel walls, a liquid film is formed as a result of lower surface contact angle. This water then migrates to the base of the channel and along toward the exit. Given the significant discrepancies between many studies, it seems plausible that the flow field design may play a major role in determining the best contact angle. Surface roughness has also been shown to have a significant effect on the water contact angle with pioneering work done by Wenzel [32]. Clearly both the bipolar plate manufacturing method and any applied coatings are likely to have a significant affect on this value.

2.3 Materials & Manufacture

2.3.1 Overview

There have been several reviews on the materials and manufacturing of bipolar plates, namely by Borup & Vanderborgh [33] Mehta & Cooper [34, 35] Hermann et al. [36] Yuan et al. [37], Brett & Brandon [38], de las Heras [39] and Hamilton & Pollet [22]. At present, no single material has all the attributes to perfectly satisfy the diverse property requirements of a bipolar plate as described earlier in Table 2.1. Consequently, trade-offs must be made between properties to yield the most favourable material for the intended application. For example, the high volumetric and gravimetric power densities provided by thin metallic plates for automotive applications still holds the interest of large auto manufacturers. The materials under consideration can be broadly grouped into two categories, metallic or carbon based as shown in Figure 2.7 and the relative advantages and disadvantages are shown in Table 2.3.

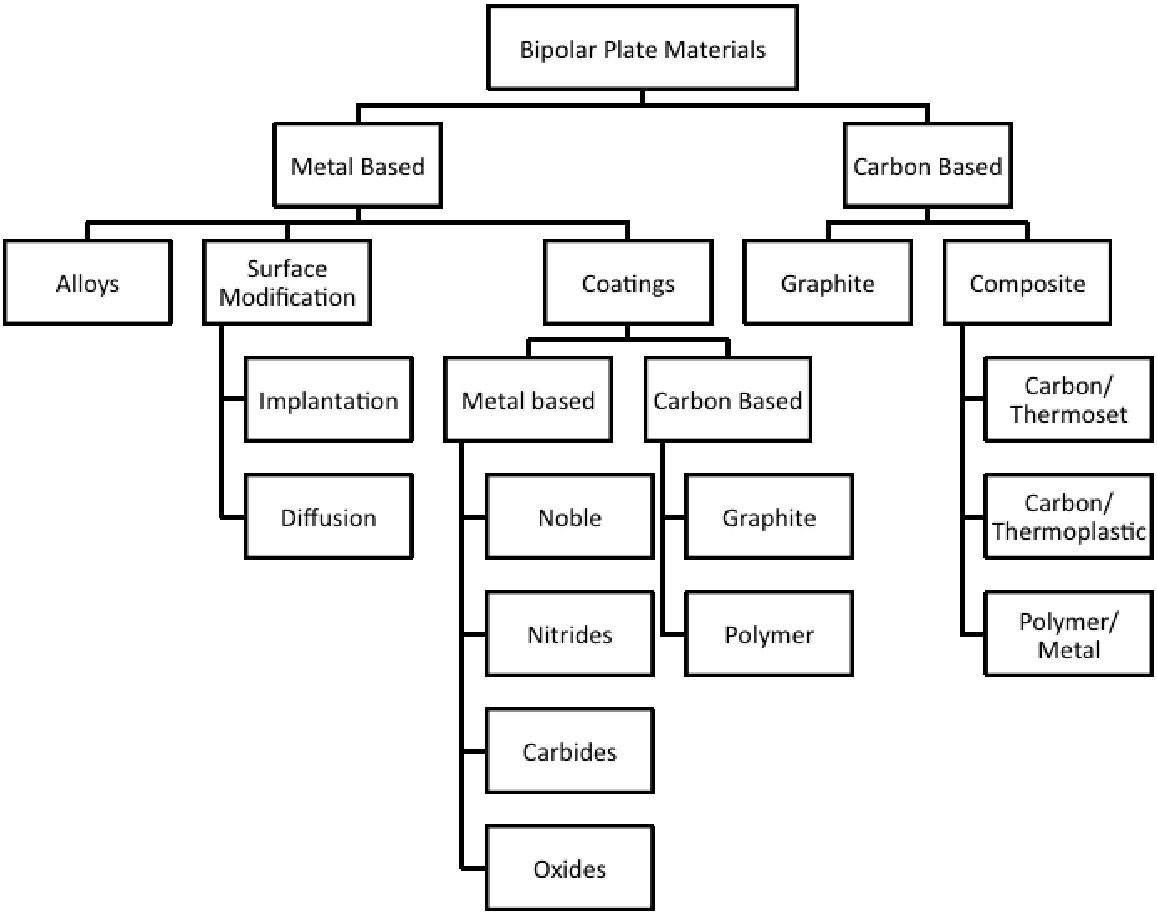

Figure 2.7 Overview of metal and carbon based bipolar plate materials

Table 2.3 Overview of bipolar plate materials advantages & disadvantages (adapted from [38])

Bipolar Plate Material	Advantages	Disadvantages	Processing Options
Metallic			
Non Coated Stainless Steel, Aluminium, Titanium, Nickel alloys	• Higher electrical and thermal conductivity • Higher strength, very thin plates possible • Higher temperature operation • Impermeable • Easily recyclable • Wide range in processing	• Poorer corrosion resistance • Form insulating oxides which may resut in high contact resistance • Ion leaching • Corrosion resistant alloys are expensive	• Computer Numerical Control (CNC) milling • Stamping/Embossing • Foaming • Die forging • Etching • Hydroforming • Depend on metal and size of plate
Coated	• As for non coated metallic above • Better corrosion resistance • Lower contact resistance	• Different thermal expansions can cause delamination • Extra processing and expense	• PVD • Electrodeposition/plating • Thermal Nitridation
Graphite			
Natural/Electro Graphite	• Good electrical and thermal conductivity • Corrosion resistant • Low contact resistance • Potentially high temperature operation	• Flow field machining required • Brittle, thick plates required • Gas permeable - requires impregnation	• CNC • Electroetch™
Flexible or Expanded Graphite	• As for natural graphite above • Flow field can be introduced during moulding • Lower density than natural graphite	• Brittle/ thick plates • Highly gas permeable - requires impregnation	• Compression Moulding
Composites			
Carbon-Carbon composite	• As for flexible graphite	• Potentially long and expensive process	• Slurry moulding, pressing, stamping • Potential for laminate addition
Thermosetting Epoxy, Phenolic, Vinyl esters	• Higher temperature operation • Lower contact resistance	• Lower bulk electrical conductivity • Slower production	• Compression Moulding
Low Temperature Thermoplastics Polypropylene (PP), Polyester (PE), Polyvinylidene fluoride (PVDF),	• Injection moulding is suited for rapid and continuous automated manufacturing • Flow field can be introduced during molding • Lower contact resistance	• Lower bulk electrical conductivity • Lower operational temperatures	• Injection Moulding • Compression Moulding
High Temperature Thermoplastics Polyphenylene sulfide (PPS), Polyether sulfone (PES) Liquid crystal polymer (LCP)	• As for low temperature thermoplastic • Higher temperature operation	• Lower bulk electrical conductivity	• Injection Moulding • Compression Moulding

2.3.2 Global Manufacturers

Table 2.4 shows some of the current bipolar plate manufacturers and material providers.

Table 2.4 Global Bipolar Plate Material Providers and Manufacturers

Bipolar Plate Material Providers	Company Information
Graphite or Composite	
Superior Graphite USA [40]	Developed FormulaBT™ for BPP applications
Timcal Graphite & Carbon, Switzerland [41]	Produce TIMREX® Graphite and carbon blacks for composite BPPs
Entegris (Poco Graphite), USA [42]	Poco Graphite was purchased by Entegris in 2008. Poco AXF-5Q has often been used as a benchmark material for BPP comparisons.
GrafTech International, USA [43]	Claim that their GrafCell® BPPs are found in 85% of fuel cell vehicles and 12 out of 14 bus programmes worldwide.
Mersen, France [44]	Formerly known as Carbon Lorraine until 2010. Produces resin impregnated isotropic graphite.
Huntsman Advanced Materials GmbH, Switzerland[45]	Awarded the JEC Award for innovative materials for developing a high temperature composite BPP based on Kerimid® polymer with GrafTech
Ticona [46]	Produce Vectra® liquid crystal polymer (LCP) and Fortron® polyphenylene sulfide (PPS) for composite bipolar plates
SGL Carbon Group [47]	SGL Group is one of the world's leading manufactures of carbon-based products. They produce composite Sigracet bipolar plates.
Schunk GmbH [48]	Manufactures high graphite content composite bipolar plates using a compression moulding process for low and high temperature PEMFCs.
Bac2 Ltd., UK [49]	Manufactures composite BPPs using a conductive polymer, Electrophen®.
ZBT GmbH [50]	Zentrum für Brennstoffzellen Technik Duisburg focus on the manufacture and composite bipolar plates and composite coatings for metallic plates.
Graphtek LLC, USA [51]	Produces compression molded plates from carbon loaded composites
Nisshinbo, Japan [52]	Developed a high strength flexible carbon material for bipolar plates
AEG, USA [53]	Elastomer-carbon fibre composite bipolar plate
Bulk Moulding Compounds Inc. USA [54]	The largest producer of thermoset bulk moulding compounds in North America. Vinyl ester composites have been developed for bipolar plates.
Engineered Fibers Technology, USA [55]	Manufactures Spectracarb 550, a thermoset molding compound
Metal	
Dana Holding Corporation [56]	Produce composite graphite-based and metallic bipolar plates. Also developing advanced coatings and cell gaskets.
Daido Steel, Japan	Nanoclad™ coating of mechanically clad 10 nm thick gold coating
Sumitomo Metals, Japan [57]	Developed stainless steel foil material with a conductive metal inclusion
Teer Coatings Ltd. (Miba Coating Group), UK [58]	Offer PVD coatings for bipolar plates
Precision Micro Ltd., UK [59]	Specialise in photochemical etching of stainless steels, titanium, nickel and other alloys for bipolar plate manufacture.
C. Brandauer & Co Ltd., UK [60]	Manufactures stamped metallic bipolar plates
Cellimpact, Sweden [61]	Have patented a high energy stamping process for stainless steel, titanium and graphite bipolar plates capable of producing 1 plate/sec/machine.
Sandvik AB, Sweden [62]	Offer roll to roll continuous carbon based PVD coatings for bipolar plates
Impact Coatings AB, Sweden [63]	Specialise in PVD MAXPhase™ coatings
Tech-Etch Inc., USA [64]	Specialise in photochemical etching of stainless steels and titanium for bipolar plate manufacture
Borit NV, Belgium [65]	Manufactures metallic bipolar plates via a hydroforming process

2.4 Graphite & Composite Bipolar Plates

2.4.1 Materials

Graphite has several suitable properties relevant for bipolar plates including excellent electrical conductivity, corrosion resistance and low density. However, there are some significant disadvantages such as brittleness and porosity which require the plates to be thicker (several millimetres) and to be sealed to make them impermeable to reactant gases. As a result of this, the plates are not so lightweight, despite graphite having a low density. Finally, a lengthy and expensive CNC (computer numerically controlled) machining process is typically needed to make the intricate flow field channels. Therefore, the combined costs of the raw material and further processing result in an expensive material that limits its usage to prototype flow fields and single test cells. In this work Toyo Tanso impregnated with phenolic resin was used as a benchmark for the in-situ fuel cell testing.

Composite materials, which consist of a conducting carbon filler (such as graphite) dispersed through an insulating polymer matrix, trade the excellent electrical conductivity of graphite for better physical properties and ease of manufacture. Composites can also be used as coatings for metallic plates and as such are investigated in this literature review to aid comparisons with PVD coatings.

Both thermoplastics and thermosetting polymers have been used for composite plates. Thermoplastics, which generally have low glass transition temperatures, include polypropylene (PP), polyethylene terephthalate (PET) and polyvinylidene fluoride (PVDF). In contrast thermosets are irreversibly cured using heat or via chemical reactions and include vinyl esters, epoxy and phenolic resins (resole and novolac types). Intrinsically conducting polymers (ICPs) such as polyaniline (PANI), polypyrrole and polyphenylene have also been used on account of their much improved conductivity compared to conventional polymers. They are often mixed with other polymers as investigated by Taipalus et al. [66] and Totsra & Friedrich [67]. The company Bac2 Ltd, UK is currently the only manufacturer to use a patented electrically conductive polymer called ElectroPhen® in their composite plates. In this work Bac 2 EP1109 was used as a benchmark for the in-situ fuel cell testing.

A wide range of carbon fillers for composite materials are available which include carbons of different sizes and dimensional forms such as graphites, carbon blacks, carbon fibres or carbon nanotubes. A review of typical carbon materials has been carried out recently by Antunes et al. [68]. It is well established in studies by Thongruang et al. [69], Dhakate et al. [70], Mathur et al. [71] and King et al. [72] that mixtures of carbon can be used in composites for improved electrical properties. They suggest that a synergistic effect occurs between different fillers where smaller particles may form bridges between the larger particles, enhancing electrical percolation through the composite.

When graphite is used in polymer composites it generally acts as a conducting material rather than a reinforcing material. This behaviour causes two effects as previously described by Lee et al. [73]. Firstly, the flexural strength of the composite decreases with increasing graphite content and secondly the conductivity of the composite increases with graphite content, but only up to a point (~75%). The decrease occurs when there is insufficient polymer to ensure that the graphite is adequately bonded together for electrical conductivity and voids are formed. High loadings may also lead to brittleness and cracking. The influence of graphite particle shape has been explored by Heo et al. [74] who found that flake shaped graphite had superior flexural strength and electrical conductivity compared to spherical graphite when used in a polymer composite.

Another popular form of graphite for bipolar plates is 'Flexible' or expanded graphite which was first developed by GrafTech International Ltd. (previously UCAR) in 2000 [75]. It is made by the chemical intercalation of natural graphite at high temperatures, which causes an expansion between the graphite planes and forms a highly networked structure. This expanded material can then be impregnated with resin and compressed to form the bipolar plate complete with flow channels. In the past, GrafTech has claimed that their GrafCell® plates were found in 85% of fuel cell vehicles and 12 out of 14 bus programmes worldwide [76], which was primarily due to their extensive use by Ballard Power Systems Inc. Expanded graphite has also been used as a coating material for graphite/phenolic composite plates by Li et al. [77] in order to decrease contact resistance. The most significant effect was found with low graphite/high polymer composites. Current research [78] at the time of writing by the US Department of Energy (DOE) in conjunction with companies Ballard, GrafTech and Huntsman is focussed on optimization of flexible graphite polymer composites for high temperature operation and reduced part thickness.

Fibrous carbons have frequently been used in the manufacture of conductive composite plates. These include carbon fibres (CF), single wall carbon nanotubes (SWCNT), multiwall carbon nanotubes (MWCNT) and vapour grown carbon nanofibres (VGCNF). The effect of different carbon fillers (CF, CB, MWCNT) on a graphite/epoxy composite has been investigated recently by Lee et al. [73] who found the individual additions of a specific amount of CF, CB, or MWCNT to the graphite/epoxy composite were all found to improve the electrical conductivity of the composite. The order of electrical conductivity enhancement was CB<CF<MWCNT and the order of flexural strength enhancement was CB<MWCNT<CF. However, the high cost of CNTs (or even graphene [79]) seems likely to restrict their use due to the demands of a low cost mass producible material.

Table 2.5 shows some of the materials and their relative proportions used in the literature for the manufacture of polymer/carbon composite bipolar plates. The conductivity values are intentionally not stated as they have been measured under a range of conditions (such as different compression), which can give a misleading indication of comparative performance.

Table 2.5 Polymer Composite Bipolar Plate Materials

Polymer Matrix	Carbon Filler	Processing	Reference
Thermoplastics			
Thermoplastic	Carbon	Injection moulded	Heinzel et al. [80]
PET/PVDF	CNT (6%)	Injection moulded	Wu & Shaw [81]
PP (20%)	Graphite (55%), Carbon Black (25%)	Compression moulded	Dweiri & Sahari [82]
PET (70%)	Carbon Black (18%), Graphite (12%)	Compression moulded	Bouatia et al. [83]
PPS (43.7%)	Graphite (43.8%), Carbon Black (8.5%), Carbon fibre (4%)	Injection moulded	Mighri et al.[84]
PET (23%) or PPS (23%)	Graphite (70%), Carbon Fibre (7%)	Slurry moulding	Huang et al. [85]
PPS	Graphite	Slurry moulding with laminate	Cunningham et al. [86]
PES/PPS	Graphite, Carbon Black (5%)	Compression moulded	Radhakrishnan et al. [87]
PPS (20%)	Graphite (80%)	Compression moulded	Xia et al.[88]
PPS	Carbon based	Compression moulded	Derieth et al. [89]
Thermosets			
Epoxy	Expanded Graphite 20%	Compression moulded	Blunk et al. [90]
Epoxy (50%)	Expanded Graphite (50%) or Expanded Graphite (45%) & Carbon Black (5%)	Compression moulded	Du & Jana [91]
Epoxy	Carbon Fibre Prepreg	Compression moulded	Hwang et al. [92]
Epoxy (25%)	Graphite (73%) MWCNT (2%)	Compression moulded	Lee et al. [73]
Epoxy (30%)	Expanded Graphite	Compression moulded	Du et al. [93]
Phenolic (Novolac) (25%)	Graphite Flake (67.5%) Expanded Graphite (7.5%)	Compression moulded	Heo et al. [94]
Phenolic 25%	Natural Graphite (65%) Carbon fibre and Carbon Black (10%)	Compression moulded	Maheshwari et al. [95]
Phenolic (Novolac) (35%)	Natural Graphite (40%), Synthetic Graphite (10%), Carbon Black (10%), Carbon Fibre (5%)	Compression moulded	Kakati & Mohan [96]
Phenolic (35%)	Natural graphite (35%), Carbon Black (25%), Carbon fibre (5%)	Compression moulded	Mathur et al. [71]
Phenolic (Novolac)	Natural graphite, Carbon Black, Carbon Fibre	Compression moulded	Dhakate et al. [70]
Phenolic (Novolac) (50%)	Expanded Graphite (50%)	Compression moulded	Dhakate et al. [97]
Phenolic (Novolac) (15%)	Natural graphite, Carbon Black	Compression moulded	Hui et al. [98]
Phenolic (Resole) (25%)	Natural Graphite (75%)	Compression moulded	Kakati et al. [99]

It has been well observed by Du [100] that through plane conductivity and in plane flexural strength are potentially opposing properties in composite materials. The orientation of carbon fillers in plane will generally result in good flexural strength, but poor through plane conductivity and vice versa when carbon fillers are orientated through plane. The alignment of the filler in the composite depends somewhat on the nature of the filler, but also the method of manufacture.

2.4.2 Methods of Manufacture

There are two main methods of manufacturing carbon/polymer composite bipolar plates: (i) injection moulding and (ii) compression moulding (a combination of these processes called injection-compression can also be used). Importantly, both of these methods offer the key advantage of moulding the gas flow channels directly into the plate. This eliminates the need for an additional costly flow field machining process and results in a cheaper and faster processing route, which is more suited for mass production.

Injection moulding has been used to manufacture bipolar plates from carbon fillers and primarily thermoplastic polymers. The process illustrated in Figure 2.8 involves feeding the granulated composite mixture into a heated barrel that contains a rotating screw. The polymer is softened by heating and the shear forces within the barrel and is driven into the mould by a hydraulic ram. Cycle time is mainly dependent on the time taken for the polymer to cool below its glass transition temperature (T_g), which in turn is governed by the part thickness.

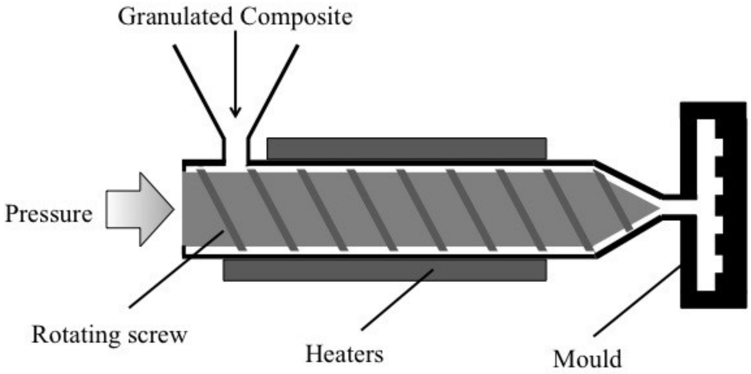

Figure 2.8 Illustration of the injection moulding process

The advantages of injection moulding include short process cycle times of 30-60 seconds and potentially low manufacturing costs of 2-10 €/kg as reported by Heinzel et al. [80]. It has been shown by Mighri et al. [84] and Derieth et al. [89] that there are two distinct orientations of carbon filler at the core and the surface for injection moulded bipolar plates. The core is the larger domain of the two and is where graphite particles primarily orientate themselves along the constant velocity flow lines during injection. This orientation also happens to also be the direction of current flow in a fuel cell. The smaller surface layer domain has graphite particles which are mainly orientated parallel to the surface.

This orientation may be an important benefit of the injection process as graphite fillers are often electrically anisotropic showing good conductivity in plane, but poorer conductivity through plane. It has been suggested by Derieth et al. [89] that injection moulded plates have higher values of through plane conductivity compared to compression moulded plates with the same filler loading. However, the main disadvantage of injection moulding is that limited amounts of carbon fillers can be used because lower viscosities are required for the injection of the composite. This is slightly problematic given that high percentages of carbon filler are preferable to give the composites sufficient conductivity. This process has also been linked extensive carbon fibre breakage by Taipalus et al. [66] which seems likely to reduce the physical and electrical properties of the composite. It has been reported by Immonen et al. [101] that increased resistivity at the surface of the composite may occur when injection moulding composites due to a polymer “skin” formed during manufacturing. Consequently, additional processing may be necessary to remove this polymer insulating film.

Compression moulding has generally been used to form thermosetting polymer composites using various carbon fillers and polymers. The process involves mixing the polymer and filler, placing the mixture in a heated mould and then compressing using a hydraulic piston as shown in Figure 2.9.

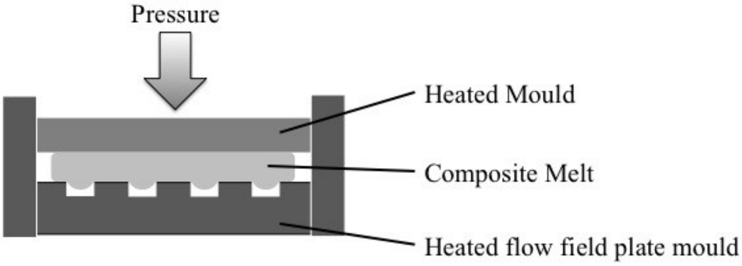

Figure 2.9 Illustration of the compression moulding process

Compressive pressure has a significant impact on the conductivity and flexural strength of the composite, which have both been found to increase with pressure [98]. Cycle time is largely dependent on the curing time of the polymer, but is significantly quicker than CNC machining and the plate can be removed whilst still hot. Bulk Molding Compounds Inc., US who manufacture composite bipolar plates have achieved curing times of 15 seconds in their compression moulding process.

The primary advantage of compression moulding over injection moulding is that higher proportions of carbon fillers can be used in the composite, as lower viscosities are not as essential to the compression process. Hence, higher contents of carbon filler may result in improved electrical conductivity. The disadvantages of compression moulding are firstly, the mechanical compression of composite plate causes the filler to align predominantly in plane rather than through plane according to Blunk et al. [90] which is contrary to the direction of electrical flow in fuel cells. Secondly, as with injection moulding, a surface polymer skin is formed [102] which may need to be removed.

Other manufacturing techniques that have been proposed include slurry moulding by Besmann et al. [103], wet lay laminating by Cunningham et al. [86], UV lithography by Hsieh et al. [104] and carbon sintering by Luo et al. [105]. As previously mentioned the same composite materials can also be used as a coating for metallic plates via spray coating.

2.5 Metallic Bipolar Plates

Initially, metals may seem to be the most obvious candidate for bipolar plates. They generally have excellent bulk electrical and thermal conductivity, low gas permeability, potentially low cost, high vibration and shock resistance, are easy to manufacture and can be made very thin (typically ~100 μm). Consequently, they are currently favoured for applications where power density and high volumes are paramount such as in automotive applications. However, the main disadvantage of metals is their potential chemically instability in the corrosive internal environment of the fuel cell – low pH, high humidity and temperatures of ~80°C. In this environment metals may firstly form electrically insulating surface layers which increase the interfacial contact resistance with the GDL, and secondly may leach metal ions which poison the proton exchange membrane and electrocatalyst [106].

2.5.1 Corrosion Theory

This section on corrosion theory is based on a helpful introduction to the electrochemistry of corrosion by Hinds [107]. The corrosion of metal involves the transport of metal ions and electrons associated with a metal surface and a solution. When a metal surface is exposed to a solution, there will be the dissolution of some positively charged metal ions into the solution, resulting in an increased negative charge at the metal surface. However, the reverse reaction, from the resulting potential difference between the metal and the solution, will then promote the deposition of metal ions back to the surface as shown in Equation 1.

$$\mathbf{M \rightleftarrows M^{n+} + n^{e-}} \qquad \textbf{Equation 1}$$

The potential at which the rates of dissolution and deposition reach equilibrium is called the reversible potential, E_r, and is dependent on the concentration of dissolved metal ions and the standard reversible potential E^0 for unit activity of dissolved metal ions, $a_M{}^{n+}$ as shown in equation (2) below

$$\mathbf{Er,}_{\,M+/M} = \mathbf{E^0}_{\,M+/M} + \frac{\boldsymbol{R}\mathbf{T}}{\mathbf{n}\boldsymbol{F}}\ \mathbf{ln\ a_{Mn+}} \qquad \textbf{Equation 2}$$

where R is the universal gas constant, T the absolute temperature, F the Faraday constant and n the number of electrons transferred per ion. However, the reversible potential of a metal in solution is not normally obtained as electrons are removed via alternative reactions. In this case, as the metal is in an acidic solution, the reaction with H^+ adsorbed on the surface of the metal to form H_2 gas as shown below.

$$2H^+ + 2e^- \rightarrow H_2 \qquad \textbf{Equation 3}$$

The loss of electrons via this process, allows the continued loss of metal ions into the solution. However, this reaction is also reversible as shown in the equation (3) below.

$$E_{r,\, H+/H2} = E^0_{\ H+/H2} - \frac{RT}{F} \ln \frac{p^{1/2}_{H2}}{a_{H^+}} \qquad \textbf{Equation 4}$$

where p_{H2} is the partial pressure of hydrogen gas. However, as hydrogen typically escapes from the environment the partial pressure of hydrogen does not build up which allows the continued corrosion of the exposed metal surface.

Hence, corrosion involves both anodic and cathodic reactions; oxidation of the metal and reduction of hydrogen ions. The rate of these reactions is driven by the potential of the metal in a solution. An increase in the potential increases the reaction promoting the anodic dissolution of the metal, whilst decreasing the cathodic reactions, and vice versa when the potential decreases. The interaction between the potential difference of a metal and the currents caused by the anodic and cathodic reactions enables the corrosion behaviour to be quantitatively characterised.

A potentiostat can be used to displace the potential of the corroding metal and measure the resultant current. If the displacement is small (<10 mV), then the potential is a linear function of the measured current density. The slope of the polarisation curve is defined as the polarisation resistance (Rp), which is also inversely proportional to the rate of corrosion or equivalent corrosion current density (I_{corr}). If the potential displacement is increased further (>10 mV), then the polarisation curve begins to show a linear relationship to the logarithm of the current density as shown in Figure 2.10.

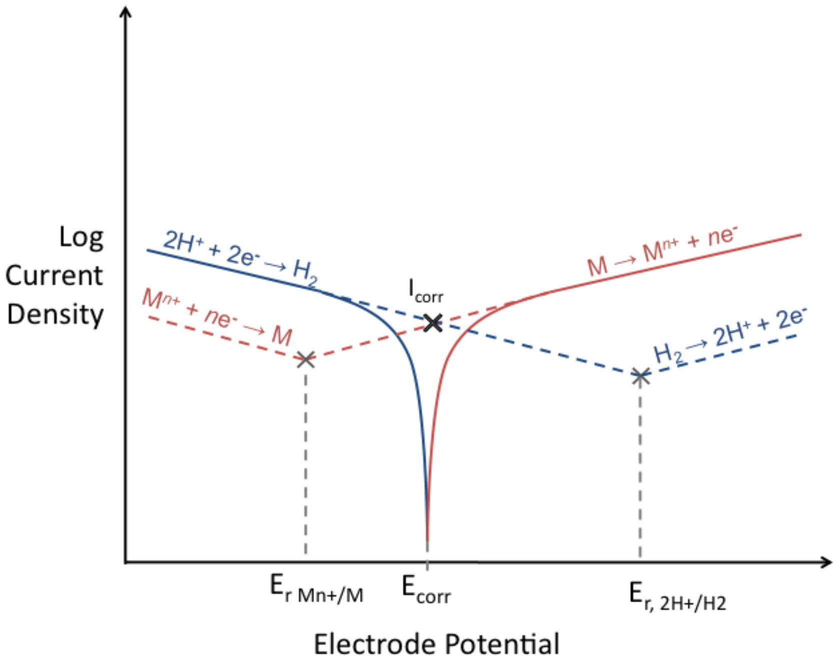

Figure 2.10 Diagram showing the cathodic (left) and anodic (right) polarisation curves for a metal corroding in an acidic solution

In this region the observed current density is dominated by one reaction on the metal surface, to the extent that the opposing anodic or cathodic reaction rate can be considered to be neglible. Here, the relationship between the overpotential (η), which the difference between observed potential and the reversible potential, and the current density can be shown by

$$\eta = i_o + b \log i \qquad \textbf{Equation 5}$$

where i_o is the exchange current density (current density at E_r) and the constant b is the 'Tafel' slope of the cathodic or anodic polarisation curve and is associated with the kinetics of the corrosion reaction taking place.

As the potential polarisation increases further, metals that form a passive layer, such as stainless steels or titanium, show an active peak followed by a passive region as shown in Figure 2.11. This is due to a reaction between the metal surface and water to form an oxide, which then obstructs the movement of metal ions in to the solution. The stability of the oxide is dependent on its solubility in the solution, the critical passivation potential (E_{pp}) and the presence of any aggressive ions.

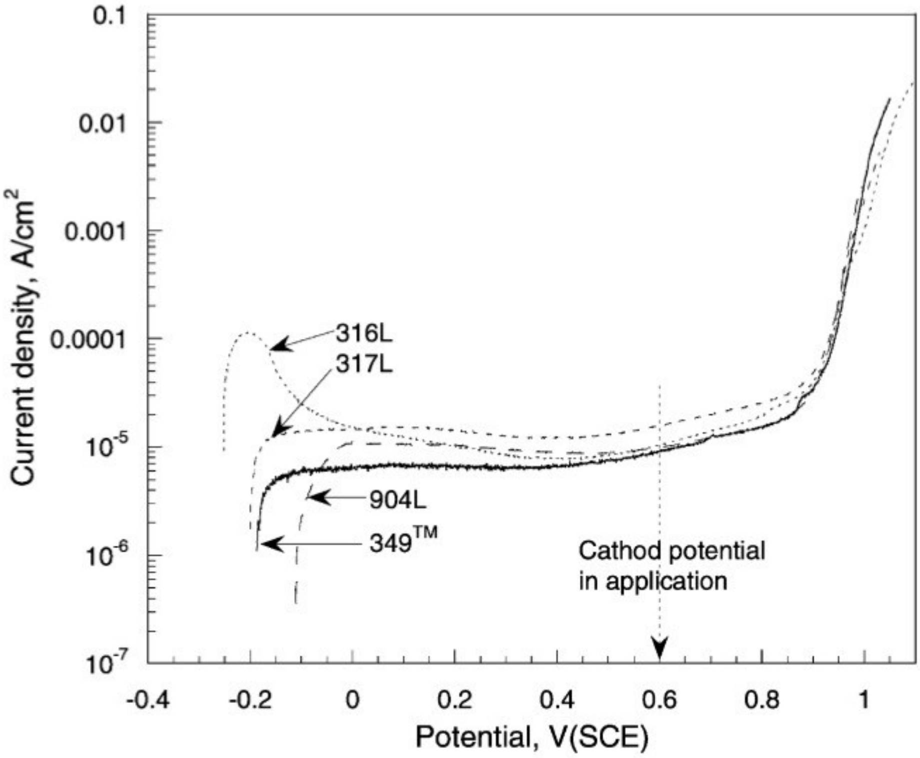

Figure 2.11 Example from the literature [108] of anodic polarisation curves (at 1 mV/s) obtained for various grades of stainless steel 316 SS in 1 M H_2SO_4 and 2 ppm F^- at 70°C purged with air

At still higher potentials the breakdown of the passive film may occur via a process of transpassive dissolution. In the case of stainless steel, chromium may be oxidised to form soluble dichromate ions as shown in equation 5 below.

$$\mathbf{2\ Cr + 7\ H_2O \rightarrow Cr_2O_7^{2-} + 14\ H^+ + 12\ e^-} \qquad \textbf{Equation 6}$$

If the potential is increased further, the current density can continue to increase due to the evolution of oxygen from water as shown in equation 6 below, although these will not be reached during the normal operation of a fuel cell.

$$\mathbf{2\ H_2O \rightarrow O_2 + 4\ H^+ + 4\ e^-} \qquad \textbf{Equation 7}$$

2.5.2 Substrate Material Candidates

Historically, substrate metal bipolar plate materials that have been investigated include a range of stainless steels (SS), aluminium, titanium and Ni-Cr based alloys, as recently reviewed by Wang & Turner [109]. Generally, both density and bulk conductivity increase in the order Al < Ti < SS, whereas cost normally increases Al < SS < Ti (ignoring specialist alloys).

Titanium bipolar plates are the least well documented in the literature, possibly due to its high material cost. It is generally considered to have excellent corrosion resistance due to its passive oxide layer; however, an early study by Davies et al. [110] showed an unacceptably high increase in interfacial contact resistance after 400 h of in-situ testing which was attributed to the further growth of the electrically insulating oxide film. Consequently, to lower the contact resistance several authors have suggested that the surface should modified by nitridation [111] or coated in some other way [112, 113]. Uncoated aluminium is an attractive option due to its low cost and has been more widely documented, however, the corrosion resistance is generally considered to be quite poor which would make it vulnerable to any defects in a coating [111, 114]. Furthermore, Sulek et al. [115] have identified that even low concentrations of ions in the membrane can have a significant effect on fuel cell performance. The greatest reduction from several transition metal ions was in the order of $Al^{3+} >> Fe^{2+} > Ni^{2+}, Cr^{3+}$. This suggests that aluminium may not be a suitable substrate as any defects in the coating or surface modification will have a more detrimental effect than other substrates such as stainless steels.

Stainless steels (especially 316L) are by far the most commonly studied bipolar plate material. However, from the quantity of coating studies in the literature it can be inferred that the corrosion resistance and contact resistance are not sufficient for bipolar plates (see Section 2.6). There are only a very small number of studies which suggest that uncoated 316L is suitable. Possibly the most notable example is a study by Davies et al. [116] who conducted a >3000 h stack test using 316L bipolar plates and saw no evidence of corrosion or cell performance decay (relative to equivalent graphite plates). Accordingly, they concluded that with slight optimization of the alloy (to improve ICR), it would be feasible to use uncoated stainless steel bipolar plates. However there were some notable limitations to the validity of their conclusion. Namely that the stack was tested under fairly amicable steady state conditions with 100% RH of reactants, no load cycling, no startup/shutdowns and a cell temperature of 50°C which is significantly lower than conventional values. Wang et al. [108] examined the corrosion resistance and ICR of several types of stainless steels. They found that increased Cr content in stainless steels reduces both the corrosion (in simulated anode and cathode conditions) and the contact resistance in the order 316L > 317L > 904L > 349™. It has been suggested that the bulk composition of stainless steels alters the surface passive oxide film which becomes thicker as alloying content decreases [110]. The type of stainless steel has also been shown to play a role as the substrate of any applied coatings protective efficiency. Wang & Northwood [117] investigated the effects of the two types of stainless steel substrate (SS410 and SS316L) on the corrosion resistance of a 15 μm TiN coating in simulated anode and cathode environments. They found the substrate had no effect on the ICR after TiN coating. However, with regards to corrosion the substrate did have an effect on corrosion, particularly under the simulated anode working conditions where the dissolution of Ti ions from the TiN coating was far greater with the less alloyed 410 substrate.

Recently, the role of surface roughness in altering the ICR has also been highlighted. It has been found by a number of studies [118-120] that a very smooth plate surface may actually increase the ICR at the GDL interface. Andre et al. [120] investigated uncoated 316L and 904L SS samples and the impact of surface roughness, bulk composition and passive film structure on ICR with a H2315 T10A Freudenberg GDL. ICR was generally stable over a large range of surface roughnesses (Rk) but a sharp increase was noted when it was reduced to < 1 μm (using SiC 2400 paper).

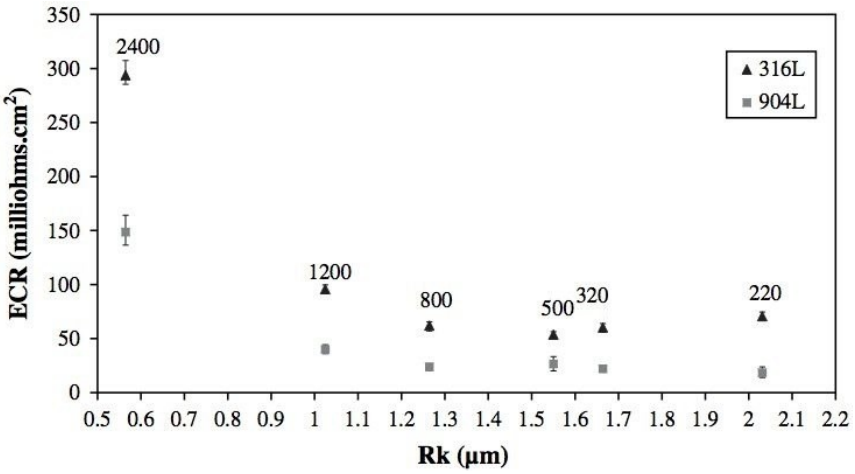

Figure 2.12 Electrical Contact Resistance (ECR) vs Rk (2D roughness parameter) obtained from polishing 316L and 904L with different SiC papers) [120]

2.5.3 Corrosion Characterisation

The US Department of Energy (DoE) 2015 target for the corrosion of bipolar plates operating in fuel cells is <1 μA/cm^2. However, there is no universally accepted ex-situ standard accelerated stress test (AST) for the evaluation of corrosion resistance of bipolar plates that the author is aware of from the EU (FCTES^{QA}), US (USFCC) or Japan (JARI). In the research literature, typically the bipolar plate is immersed in 0.1 – 1 M H_2SO_4 with 0 – 5 ppm of HF at 60 – 80 °C, whilst being bubbled with air or hydrogen and held at a particular potential (0.84 V/RHE or 0.1 V/RHE) to simulate the cathode and anode potentials respectively. These potentials are chosen to simulate those experienced by the cathode and anode in an operational fuel cell as shown below in Figure 2.13.

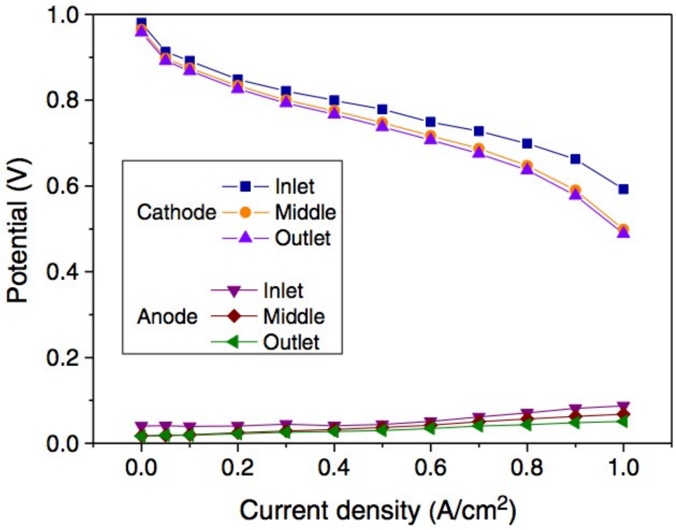

Figure 2.13 Polarisation curves for cathode and anode measured *in-situ* with respect to a reversible hydrogen electrode (RHE) [121]

Extensive tables showing the corrosion test protocols vary from study to study, however comprehensive tables showing a range of coated metallic bipolar plates in the literature have been compiled by Tawfik et al. [122] and Antunes et al. [123]. These corrosion test conditions are intended to mimic the degradation of the Nafion® membrane with SO_4^- and F^- ions at fuel cell operating temperatures. However, corrosion is far from a simple process and the fuel cell creates an environment with a considerable range of conditions of varying heat, acidity, humidity and electrical potential. It is questionable how realistic these typical ex-situ test conditions are to in-situ testing for several reasons as follows.

The vast majority of studies only examine the corrosion conditions under fuel cell operating cathodic potentials. However, Andre et al. [124] have simulated idle fuel cell operations on various stainless steels and identified cathodic stand-by conditions of 1 V/RHE resulted in excessive cation release compared to operating conditions of 0.8 V/RHE. They suggested that chromium oxide alone would not provide protection at this higher potential. This is an important finding as the fuel cell load cycle may well include periods of these higher potential stand-by conditions. However, the situation may even be more severe than this. A reverse-current mechanism has been identified by Reiser et al. [125] which describes the corrosion of the catalyst carbon support at 1.44 V when both hydrogen and oxygen are both present in the anode flow field, but physically separate producing a hydrogen-air front. This situation may arise when the fuel cell starts up or shuts down where oxygen is present on both the anode and cathode sides until hydrogen starts to be supplied to the anode, and after shut down, when air slowly leaks back into the anode. Localized fuel starvation is another situation when this may occur when oxygen diffuses through the membrane from the cathode side to the anode side in areas where there is a reduced hydrogen supply. The in-situ observation of the reverse-current mechanism has recently been demonstrated in-situ by Hinds & Brightman [121]. From the literature, potentials of 1.4 V are not typically applied to stainless steel bipolar plate, which is electrically connected to the GDL and the carbon supported catalyst. From Andre et al. [124] work, it would seem highly improbable that stainless steel would be stable at this potential. However, Yu et al. [126] have suggested that system mitigation strategies may be easier to implement than the development of new materials capable of being electrochemically stable at high potentials. They reviewed the latest strategies from the literature and patents to prevent an air/hydrogen interface at the anode. They generally focused on minimising the time that the interface exists or reducing the potential. A summary of these strategies included; a gas purge to anode before startup and after shutdown, exhaust gas recycle as purging gas or reaction gas, an electronic short to eliminate high potential at the cathode or applying an auxiliary load to consume residual oxygen at the cathode with potential control. It is interesting to note that some manufacturers, such as Hydrogenics, are now offering unlimited startup/shutdowns suggesting that some of these strategies are suitably effective. In light of this stainless steels may still be a suitable substrate material provided that effective mitigation strategies are put in place at a system level.

There seems to be some conflict in the literature over which environment, the cathode or anode is most severe in terms of corrosion. Ex-situ tests have generally suggested that in potentiostatic tests the cathodic environment is most severe with greater concentrations of metal ions being found on the cathode side in some studies [127, 128]. However, some in-situ tests have suggested that the anodic environment causes the greatest release of metal ions despite the lower potential. Agneaux et al. [129] measured the metal ion concentrations in the cathode and anode outlet water after 500 h of fuel cell operation, although the exact conditions were not stated. They found that the concentration of metal ions from the anodic water outlet was significantly greater than that of the cathode side decreasing in the order of 316L > 904L > 254SMO > Graphite. It is unclear what affect the load profile would have on metal ion release.

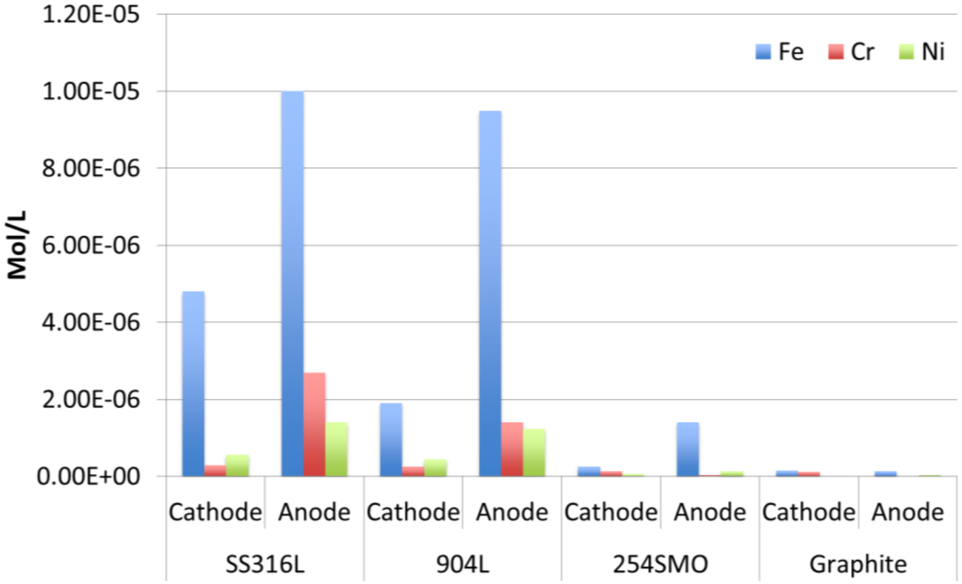

Figure 2.14 Graph of metal ion concentration at the anode and cathode after 500hrs. Data extracted from Agneaux et al. [129]

It is also of interest to note that a patent from GM (US 2011/0104589A1) also suggests that the corrosion is greater at the anode side and consequently proposes the arrangement of a carbon composite anodic plate with a metallic cathodic plate has been suggested.

Although an accelerated stress test electrolyte is not necessarily supposed to exactly mimic the conditions in a fuel cell, it should include the key elements that cause degradation of the bipolar plate. However, the current test protocol does not consider the significance of other corrosive agents (excluding HF) formed in the fuel cell environment such as H_2O_2 and its associated radicals. According to Curtin et al. [130] and Inaba et al. [131] either the cross-over of either reactant gases through the membrane or the agglomeration of the Pt catalyst promote the production of H_2O_2 which may decompose (catalysed by Fe^{2+}, potentially from the corrosion of a stainless steel) to form hydroxy or peroxy radicals which may degrade the membrane and bipolar plate. Lui & Zuckerbrod [132] have demonstrated the in-situ detection of H_2O_2 and found the concentration produced depended primarily on membrane thickness, with H_2O_2 concentration increasing with decreasing membranes thickness. The rate of formation of hydrogen peroxide on the cathode side has been estimated by Sethuraman et al. [133] to be three orders of magnitude higher than on the anode side at 0.6V load.

The literature also does not generally take into account the contact between the metallic bipolar plate and a carbon GDL. Mele & Bozzini [134] have reported that localised corrosion occurred on a metal bipolar plate (AISI 304) due to the combination of two mechanisms. Firstly, galvanic coupling between the metal plate and carbon material, and secondly the introduction of a crevice caused by the tight interface between the two materials. These galvanic and crevice forming mechanisms are not considered in the overwhelming majority of the literature investigating bipolar plate corrosion.

In summary, the corrosion of bipolar plates is clearly a complex issue. A summary of some of the variables affecting the corrosion in fuel cells is shown in Table 2.6. This shows the breadth of factors that need to be considered when investigating the corrosion of bipolar plates. It also shows the need for a range of corrosion mitigation strategies including the careful consideration of materials, manufacturing method, design and system operating conditions.

Table 2.6 Summary of variables affecting bipolar plate corrosion in fuel cells

Category	Variable	Effect on corrosion rate
Materials	Substrate	The corrosion rate of different materials differs e.g. increasing the Cr, Mo, N, Ni content improves corrosion resistance of stainless steels. Wang et al. [117] found the corrosion current density of two SS substrates differed despite having the same PVD coating.
	Surface Roughness	Rougher surfaces have a larger surface area for corrosion to take place. The type of roughness is also important factor eg. crevices or undulating surface. Surface modification methods can also result in chemical changes. Electropolishing has been shown to improve corrosion resistance due to the formation of a thick Cr rich passive film [135]
	Surface Coating	Different coatings have different corrosion resistances; however, imperfections in coatings may expose the substrate material create a galvanic couple. Quality of coating will be affected by the method of deposition. Multilayer coatings are less likely to have through coating defects [136].
Manufacture	Method of Manufacture	Stamping and hydroforming conditions have been shown to increase the corrosion rate [137]. Etching alters the surface roughness and chemistry.
Design	Flow Field Design	Poor design can lead to uneven water distribution which can result in more acidic regions of the plate increasing corrosion [138] Alternatively blockage of reactants can result in hydrogen starvation, which can cause high localised voltages [125]
	Contact with GDL	Introduces additional galvanic and crevice corrosion mechanisms [134] Product water tends to break through the GDL in the same place
Operating Conditions	Cathode or Anode	Plates are exposed to either reducing or oxidising gases and water. At differing electrode potentials the corrosion current density will vary.
	MEA Operation and Degradation	Operation of MEA produces H_2O_2 [131] which may decompose to form hydroxy or peroxy radicals which in turn may degrade the PFSA membrane and release SO_4^{2-} and F^- ions. All of these products will increase the corrosion rate. Aged MEAs have been shown to produce more acidic product water [53].
	Temperature	Increased temperatures increase the rate of corrosion and further the rate of MEA degradation. Fluctuations in local plate temperature will also cause areas which are more prone to corrosion. Thermogalvanic corrosion
	Relative Humidity	Low gas humidity has been found to result in more acidic water product being generated which will increase the corrosion rate [53]
	Stack Compression	Increased compression will reduce the porosity of the GDL and result in a tighter crevice between bipolar plate and GDL and seems likely to increase localized corrosion.
	Cell Load	Long periods of time under standby conditions may exacerbate corrosion on the cathode side.
	Start up/Shut down Procedure	Reverse current mechanism leads to high potentials on the cathode side. Hydrogen/air fronts in the flow field at start up/shut down can cause localised high voltages (linked to carbon corrosion) which will increase the corrosion rate [125]. Residual water after shutdown may facilitate corrosion when not in operation.

2.5.4 Methods of Manufacture

The three most common processing options available for metal bipolar plates include etching, stamping and hydroforming. The finished plate must have very high geometrical accuracy to ensure uniform compression and gas tightness when encorportated into a fuel cell stack. Presently, two popular processes for mass manufacture of bipolar plates are photochemical etching and stamping as carried out by UK companies such as Precision Micro Ltd. and Brandauer Ltd. respectively, as referenced later in this work.

Photo-chemical etching, also known as photochemical milling, involves coating the metal plate (typically stainless steel) with a UV sensitive polymer called a photoresist, which hardens after exposure to UV light. A CAD designed negative image ‘phototool’ can then be created which acts as stencil. Subsequently, when the metal is exposed to UV light, it leaves the hardened photoresist design pattern on the surface of the metal. The metal sample is then developed by washing away the unexposed resist and etched by spraying with heated acid such as ferric chloride to corrode away the unprotected metal. After etching, the chemically inert photoresist can then be removed to leave the finished part. The advantages of this process include low tooling cost, high tolerances, stress/deformation free components and multiple parts per sheet. Additionally, different anode and cathode flow fields can be used on the same bipolar plate. Potential limitations include longer production times. The effect chemical and physical surface changes on the ICR and corrosion resistance after etching is unclear.

Alternatively, stamping can be used to rapidly deform the plate materials to form the flow field channels. The formed channels can also be the lands of an adjacent cell reducing cell width and increasing power density. The primary advantage of the stamping process is its very short production times and low overall costs. However, limitations include higher tooling cost and non-stress free components in which recoiling, local thinning or spring-back may occur. The plate design is also restricted in that the radial geometry and depth of the channels must be considered to avoid puncturing the plate. A variation of this stamping process is hydroforming, which uses high pressure water to form the flow field rather than a male stamping tool. The effect of these two manufacturing methods on corrosion resistance of uncoated material has been investigated by Dur et al. [137] who have found an increase in the corrosion rate in the order of unformed < hydroformed < stamped which was attributed to increased surface roughness. Manufacturing variables such as pressure and pressure rate were have also been found to have an impact on the corrosion resistance of final plate. Ideally any necessary coatings should be applied before stamping to increase process efficiency, but this requires coatings with excellent adhesion and a certain degree of flexibility. Given the brittle nature of carbon polymer composites it seems unlikely that this type of coating would be appropriate; however, thin film PVD coatings may be more suitable, although further work needs to be done.

2.6 Surface Engineering Techniques

There are a range of surface engineering approaches that can be used to address the issues of corrosion and interfacial contact resistance. There are an extensive range of options for metal based bipolar plates as reviewed by Tawfik et al. [122], Wu et al. [139], Antunes et al. [123] and Wang & Turner [109]. This section categorises the available options into substrate surface modification, metallic and carbon based (including polymer) thin film coatings.

2.6.1 Surface Modification

Surface modification techniques include diffusion based methods such as thermal nitridation or the implantation of a small amount of corrosion resistant and conductive metal particles as shown in Table 2.7. Thermal nitridation of stainless steel alloys, Ni/Cr alloys and Cr electroplated steels [140] has been shown to improve the ICR and corrosion resistance to varying degrees depending on the degree of the nitride surface continuity. Initial work nitriding an expensive Ni–50Cr alloy at 1100 °C for 2 h [141] resulted in the creation of a continous CrN/Cr_2N nitride layer with excellent corrosion resistance and conductivity, whereas the same treatment on austenitic 349™ resulted in discontinous layer which had improved ICR but poorer corrosion resistance. The authors also investigated high-Cr superferritic AISI446 [142] which also resulted in a discontinuous layer with internal Cr nitride precipitation. Subsequent work by Yang et al. [143] found that it was actually possible to form a continuous, protective CrN/Cr_2N) surface layer on Fe-base stainless steel alloys. A pre-oxidation of the surface to form Cr_2O_3 was found to keep the nitrogen at the surface, resulting in a Cr_xN layer after nitriding. The addition of V to the alloy was also found to assist the conversion to nitride. The resulting Cr_xN layer was found to have excellent corrosion and ICR properties. As higher Cr content alloys are susceptible to forming a brittle sigma phase a lower Cr content alloy (Fe–20Cr–4V) has been explored in order to improve formability for stamping [144]. This enabled the in-situ performance of the materials to be tested in the second part of this work [145]. A recent presentation by More [146] which summarized work from ORNL and NREL on thermal nitridation expressed some concern for nitrided surfaces if frequently exposed to operational voltages of >1V. A potentially more economical method with respect to thermal nitridation has been suggested by Wang & Turner [147] who carried out electrochemical nitridation of AISI446 which should avoid material deformation, phase changes and costs associated with high temperatures. Other surface modification techniques less well examined in the literature include surface implantation. This has been used to modify the passive oxide layers of stainless steels as examined by Lavigne et al. [148] and Feng et al. [149] to improve conductivity and/or corrosion resistance.

Table 2.7 Surface modification techniques for metal based bipolar plate materials

Type	Method	Substrate	Reference & Year
Gas based diffusion	Thermal nitridation at 1100 °C for 2 h	Ni–50Cr alloy & 349™ SS	Wang et al. [141] 2004
	Thermal nitridation at 1100 °C for 2 or 24 h	AISI446	Wang et al. [142] 2004
	Thermal nitridation	V-modified Fe–27Cr alloy	Yang et al. [143] 2007
	Thermal nitridation	Ni–Cr alloys G-30® and G-35™, AL29-4C®	Brady et al. [150] 2007
	Thermal nitridation	Fe–20Cr–4V alloy and type 2205 0.1mm foils	Brady et al. [144] & Toops et al. [145] 2010
	Thermal nitridation	0.2 mm Electroplated Cr SS316L	Han et al. [140] 2009
Liquid based diffusion	Electrochemical nitridation of NH_3 and a nitride layer	SS 446	Wang & Turner [147] 2011
Implantation	Ce insertion	SS 316L	Lavigne et al. [148] 2010
	Ag ion implantation	SS 316L	Feng et al. [149] 2011

2.6.2 *Metallic Thin Film Coatings*

There are a range of metal based thin film coatings that have been explored in the literature including noble metals, nitrides, carbides and oxides. PVD is the dominant method of deposition with coating thickness varying from nanometers to several microns as shown in

Table 2.8.

Gold, perhaps, is the most obvious coating candidate because of its very high chemical stability and low electrical resistance. However, it has historically been considered too expensive to be a viable option for coatings. Nevertheless, recently Kumar et al. [151] have suggested that Daido Steels very thin Au Nanoclad® coating of 10 nm of Au would enable the coating to be commercially viable, (estimating that only 5 g of gold would be required for 80 kW stack) in addition to providing sufficient corrosion resistance and electrical conductivity. The authors also suggested that any defects in the coating could be accommodated by the passivation of the underlying 316L under cathodic conditions; however, it is not clear if this protection would continue under extended anodic conditions. It would also be interesting to examine the quality of adhesion compared to PVD Au as the coating is mechanically clad to the substrate.

Figure 2.15 Daido Steel's Au Nanoclad® coating on a Ford bipolar plate

Whilst many metal nitrides have been widely researched, very few studies examine more than one coating simultaneously as can be seen from

Table 2.8. This can lead to some difficulty in comparing the performance of different coatings. Furthermore, the different deposition methods, coating thicknesses, substrates and experimental test procedures reported in individual papers make it impossible to directly compare the performance of the coatings.

Of the studies that did examine more than one coating, Wang et al. [152] investigated the contact resistance and electrochemical properties of electron beam physical vapour deposited (EBPVD) coatings on 316L. Contact resistance increased in order TiAlN < CrN < TiN < SS316L while corrosion resistance in simulated anodic and cathodic environments were TiN > CrN > SS316L > TiAlN, and SS316L > CrN > TiN > TiAlN respectively.

Possible reasons for the variation between studies of the same coating are the changeable conditions of PVD deposition. A review by Iordanova et al. [153] highlighted that the crystallographic orientation of the coating is sensitive to a large number of factors including, film thickness, substrate biasing, substrate temperature, sputtering gas mixtures and nitrogen partial pressure, energy of the bombarding particles and ion/atom flux ratio. Many authors have shown that these factors have a dramatic effect on the properties of the coating including corrosion resistance and ICR. Huang et al. [154] showed that the lowest resistivity of a TiN coating was associated with stoichometric (1:1) TiN which had a high packing factor (less lattice defects). In other work Huang et al. [136] found that multilayer coatings possessed fewer pinholes than a single layer coatings due to the interlayer interrupting any through-thickness defects which therefore improved corrosion resistance. The packing factor was also found to be more important than the film thickness to the corrosion resistance of < 500 nm coatings. High power pulsed magnetron sputtering (HPPMS) or HiPIMS has been identified as a method of increasing the target current and plasma density to improve coating density and morphology [155]. This method may also infer an improvement in conductivity and corrosion resistance although this has yet to be shown in the bipolar plate literature.

A final group of materials which may be included in this metal nitride section are MAX materials. These are ternary compounds with an approximate formula of M = Ti, Sc, V, Cr, Zr or Ta. A = Si, Al, Ge or Sn. X = C and/or N. Both Sandvik (US7786393, 2010) and Impact Coatings (US7786393, 2010) hold patents for the use of these coatings for electrical contact elements, for which bipolar plates would fit. There does not seem to be any data in the open research literature on the performance of these coatings; however, a recent presentation [156] suggested that the coating has excellent ICR and corrosion properties and has been used in a 2,000 hr stack test.

Although metal oxides may have improved corrosion resistance they are generally not so electronically conductive. This results in relatively few oxides being deemed suitable for bipolar plates. However, Treadstone Technologies Inc. has suggested that non conductive metal oxides could be used in conjunction with a more conductive metal. Their patented method (US 2009/0176120) involves coating the surface with a non-conductive and corrosion resistant material such as TiO_x (by electron beam evaporation for example) followed by plasma spraying the surface with conductive gold nano dots which cover a small surface area of ~2%. Despite the very low surface coverage the contact resistance is still sufficiently low to meet the ICR target.

Figure 2.16 Treadstone Technologies Inc. coating on a Ford bipolar plate

A more recent patent (US 2011/0076587) includes the use of non precious metal powders such as Ti or Cr which could be thermally sprayed in a nitrogen atmosphere to create a conductive nitride before they adhere to the corrosion resistant substrate. Although this may reduce cost, the stability of these materials is obviously likely to be less than gold.

Table 2.8 Coating Materials and Methods for Metal Based Coatings (inc. [122],[139])

Group	Method	Coating	Substrate	Reference & Year
Noble Metals	Pulse Current Electrodeposition	1) Cu 2) Ni 3) Au	Al	Woodman et al. [12] 1999
	Electrodeposition	Au	Al, SS 316L	Hentall et al. [111] 1999
	Electroplating	Au	SS 316L	Wind et al. [157] 2002
	Electroplating or PVD	2 nm, 10 nm, 1 µm Au, Zr, ZrN, ZrNb, ZrNAu,	SS 304, 310, 316	Yoon et al. [158] 2008
	Mechanical cladding	10 nm Au Nanoclad® Daido Steel (Japan)	100 µm SS 316L	Kumar et al. [151] 2010
Metal Nitrides	PVD and chemical anodization/oxidation overcoating	(1) Ti over TiAlN; (2a) Cr (Ti, Ni, Fe, Co) followed by H_2SO_4 /chromic acid OR; (2b) Graphite	Al, Ti, Ni, SS	Zafar et al. [159] 2001
	PVD or CVD, Electroless Deposition for Ni-P alloy	(1) Cr/Ni/Mo rich SS or Ni-P alloy; (2) TiN	Al, Ti, SS	Li et al. [160]
	Radio Frequency Sputtering	TiAlN, TiN	Al, Ti	Matsumoto et al. [161] 2001
	PVD	NS	SS	Silva et al. [162]
	PVD	CrN	SS 316, SS 304	Pozio et al. [163] 2008
	PVD	TiN	SS 410	Wang & Northwood [164] 2007
	Electrodeposition	TiN	SS 316	Li et al. [165] 2004
	PBAIP	CrN	SS 316L	Wu et al. [166] 2009
	Inductively coupled plasma (ICP) assisted, reactive DC magnetron sputtering	(Ti,Cr)N	SS 316L	Choi et al. [167] 2009
	Ion Beam Sputtering	ZrN	SS 304	Larijani et al. [168] 2009
	Electron Beam PVD	TiN, TiAlN, CrN	SS 316L	Wang et al. [152] 2010
	Cathodic Arc Evaporation PVD	ZrN, ZrN/CrN	Al-5083	Barranco et al. [169] 2010
	PVD	0.1 µm, 0.5 µm, 1 µm TiN, CrN, ZrN	51 µm SS 316L	Dur et al. [170] 2011
	ICP assisted, reactive direct current magnetron sputtering	TaN_x with varying N_2 flow rate	SS 316L	Choe et al. [171] 2011
	Plasma surface diffusion	9 µm Nb-N	SS 304	Wang et al. [172] 2012
	Plasma surface diffusion	~4 µm Mo_2N	SS 304	Wang et al. [173] 2012
	PBAIP	Cr/CrN Multilayer	SS 316L	Zhang et al. [174] 2012
Carbides	Electro-Spark Deposition	Cr Carbide	SS	Natesan et al. [175] 1987
	Glow discharge decomposition and PVD	(1) n-Type SiC; (2) Au	SS	Matsumoto et al. [161] 2001
	-	Carbide with Ni/Cr binder	Al	Hung et al. [176] 2009
Metal Oxides	Electron Beam Evaporation	Indium doped tin oxide $(Sn(In)O_2$	Ti	Matsumoto et al. [161] 2001
	Vapor Deposition and Sputtering	(1) Pb (2) PbO/PbO_2	Ti	Matsumoto et al. [161] 2001
	Electron Beam Evaporation and plasma spray	Non-conductive oxide with Au nanodots	-	Treadstone Technologies (US 2009/0176120)

*(PVD- Physical Vapor Deposition, SS- Stainless Steel, PBAIP- Pulsed bias arc ion plating, NS- not specified)

2.6.3 Carbon Based Thin Film Coatings

Pure carbon has many allotropes as a consequence of its atomic structure. Of its six electons, there are four in the outer shell, two each in the s and p orbitals. These electrons can bind in three different ways to form sp^1, sp^2, or sp^3 bonds. Amorphous carbons (a-C) are predominately sp^2 bonded, whereas diamond-like carbons (DLC) are mainly sp^3 bonded. Carbon/polymer coatings and conductive polymer coatings are also included in this section as they are essentially carbon based materials. A summary of carbon based materials is shown in Table 2.9.

Diamond like carbon (DLC) coatings have been examined by a few authors [33, 114]; however, they typically have unacceptably high electrical resistance due to their low sp^2 content. Studies have been carried out to investigate how it might be reduced [177].

Amorphous carbon coatings have widely been shown to significantly reduce the ICR and increase the corrosion resistance particularly by Feng and coworkers [178-180]. However, the long term durability of this coating is yet to be tested in the literature, with possible increased degradation at high potentials being a particular concern.

Coating metals with carbon-polymer composites has not been extensively researched, but Kitta et al. [181] have also showed some promising results with significant improvements in through-plane conductivity and corrosion resistance. Importantly, the surface of the stainless steel substrate was modified prior to coating by shot blasting to decrease ICR. A potential drawback of these type of coatings would be the brittle nature of composite coatings which may be unsuitable for stamping.

Conductive polymer coatings such as polyaniline and polypyrrole have been electrodeposited or painted on stainless steels and aluminium substrates [182, 183]. These coatings have shown improvements in corrosion resistance; however, crucially the polymers are not sufficiently conductive to meet the ICR targets. The authors do suggest that ICR would be improved under acidic fuel cell conditions, but the extent of which was not clarified.

Table 2.9 Coating Materials and Methods for Carbon Based Coatings (inc. [122],[139])

Coating Type	Method	Surface Coating	Substrate	Reference & Date
Diamond-like Carbon (DLC)	-	DLC	-	Borup & Vanderborgh [33] 1995
	PVD	DLC- YZU001	Al-5052	Lee et al. [114] 2003
	PVD	DLC film with embedded carbon & Cu nanoparticles	SS	Sasaki et al. [177] 2011
Carbon	Painting or Pressing	(1) Graphite particles in an emulsion, suspension or paint (2) Exfoliated graphite	Al, Ti, Ni	Zafar et al. [159] 2001
	Radio Frequency Plasma Enhanced CVD	Amorphous Carbon	Ti	Show [184] 2007
	Plasma Assisted CVD	Carbon	SS 304	Fukutsuka et al. [185] 2007
	PVD & CVD	PVD Nickel transition layer under CVD carbon film	SS 304	Chung et al. [186] 2008
	CVD	Carbon	SS 304	Chung et al. [187] 2009
	PVD (CFUBMSIP)	(1) Cr transition layer (2) Amorphous Carbon	SS 316L	Feng et al. [178] 2009
	PVD (CFUBMSIP)	Amorphous Carbon	SS 316L	Feng et al. [179] 2010
	PVD (CFUBMSIP)	Amorphous Carbon	SS 304	Yi et al. [188] 2010
	PVD	Amorphous Carbon	2 mm SS 316L	Larijani et al. [189] 2011
	PVD (CFUBMSIP)	1 μm Cr transition layer & 2 μm Amorphous Carbon	SS 304	Jin et al. [180] 2011
Carbon/Polymer Composite	Shot blasting, doctor blade and hot pressing	Graphite, Epoxy Resin and Phenol Hardener	0.2 mm SS 304	Kitta et al. [181] 2007
	Electropolymerization and pyrolyzing	C-SiO_2-N and PANI-C-SiO_2	SS 304	Wang et al. [190] 2011
Conductive Polymer	-	Organic self-assembled Monopolymers or conductive polymer	-	Borup & Vanderborgh [33] 1995
	-	Carbon fibres within a polymer matrix	SS	Fronk et al. [191] 1999
	Electrodeposition	Multilayer coating (Ni, Au) and Polyaniline (PANI)	Al	Kimble et al. [192] 1999
	Spraying	(1) Conductive polymer; (2) Graphite; (3) Conductive polymer	SS	Cunningham et al. [193] 2002
	Electrodeposition	PANI and Polypyrrole (PPY)	SS 304	Joseph et al. [182] 2005
	Electrodeposition	PANI and PPY	SS 304	Gonzalez-Rodriguez et al. [194] 2007
	Cyclic Voltammetry and Painting	PANI and PPY	Al 6061	Joseph et al. [183] 2008

*(PVD – Physical Vapor Deposition, SS – Stainless Steel, CFUBMSIP – Closed Field Unbalanced Magnetron Sputtering Ion Plating)

Table 2.10 shows patents relevant to PVD carbon based coatings for bipolar plates. The results are dominated by General Motors. Whilst much of GM's work has focussed on carbon based coatings, it could be argued from their recent patents that the carbon coatings may not maintain their hydrophilicity (US2011/0070528) and/or that they may not be sufficiently electrochemically stable over extended periods of operation (US 2010/0304267).

Table 2.10 PVD carbon based coatings for bipolar plates from the patent literature

Patent	PVD Coating	Inventor
GM Global Technology Operations, Inc.		
Low Contact Resistance PEM Fuel Cell (2004) US 6,811,918	Deposition of 'hyperconductive' surface layer onto composites	R.H. Blunk et al.
Ultra-low loadings of Au for stainless steel bipolar plates (Dec, 2009) US 7,625,654	Ru, Rh, Pd, Ag, Ir, Pt, Os and preferably Au	G.V. Dadheech et al.
Amorphous Carbon Coatings for Fuel Cell Bipolar Plates (Feb, 2010) US 8497050	Amorphous carbon with activated hydrophilic surface	G.V. Dadheech et al.
Graphene Coated SS Bipolar Plates (Feb, 2010)	Graphene containing layer with activated hydrophilic surface	G.V. Dadheech et al.
Coated Steel Bipolar plates (Aug, 2010)	Graphitic layers characterized by sp^2 carbon-carbon bonding, Mo doped InO, Cr+N or $MoSi_2$	M. Budinski et al.
Surface Treated Carbon Coatings for Flow Field Plates (Aug, 2010) US2010/0323276	Carbon coatings made either more hydrophilic using oxygen/nitrogen gases or more hydrophobic by using fluorinated gases	G.V. Dadheech & M.H. Abd Elhamid
Method to Enhance the Durability of Conductive Carbon Coating of PEM Fuel Bipolar Plates (Dec, 2010) US 2010/0304267	Carbon-containing layer is doped with a metal such as Pt, Ir, Ru, Au, Pd or combinations thereof. These carbon-containing layers show improved corrosion resistance than when doped with other metals such as Ti or Cr	Y.M. Mikhail et al.
Carbon Based Bipolar Plate Coatings for Effective Water Management (Mar, 2011) US2011/0070528	The carbon coating is overlaid with a silicon oxide layer which is then activated to increase hydrophilicity and results in a minimal increase in contact resistance	G.V. Dadheech & M.J. Lukitsch
Conductive and Hydrophilic Bipolar Plate Coatings and Method of Making the Same (Mar, 2011) US2011/0070529	The carbon coating is overlaid with a titanium oxide layer which is then activated to increase hydrophilicity and results in a minimal increase in contact resistance	G.V. Dadheech & M.J. Lukitsch
Corrosion Resistant Metal Composite for Electrochemical Devices and Methods of Producing the same (Jul, 2011) US7,972,449	Deposition of Ni-Cr-Mo alloy on a stainless steel substrate resulting in lower contact resistance and improved corrosion resistance	M.H. Abd Elhamid et al.
ABB Research Ltd. & Impact Coatings AB		
Contact element and a contact arrangement 2009/1278905	Nanocomposite film having a matrix of amorphous carbon	E. Lewin et al.

2.7 Thesis Aims

This literature review has highlighted the importance of bipolar plates in PEM fuel cells and has explored many of the major issues regarding their design, materials, manufacture and characterisation. In particular, matters of corrosion resistance and interfacial contact resistance (ICR) for metallic plates have been identified. From the literature, coatings have been shown to be an effective way of addressing these issues. Therefore, this work was focused on the development and characterisation of metallic and carbon based coatings for metal bipolar plates. As coating performance is often affected by the underlying substrate, various alterations to the substrate were investigated to examine the effects on the surface topography of a range of manufacturing techniques such as photochemical etching and stamping. Closed Field Unbalanced Magnetron Sputter Ion Plating (CFUBMSIP) was then used to deposit a range of coatings including TiN, CrN, ZrN, Graphit-iC™, Au and carbon multilayer coatings of varying thickness. The interfacial contact resistance of the coatings was measured both prior to and after corrosion tests. The importance of ICR on in-situ performance will also be clarified using a single cell test. Post corrosion surface characterisation via XPS identified chemical changes in the coating composition related them to observed changes in ICR. Due to the complexity of the corrosion issues and the lack of long term in-situ testing capability, corrosion experiements were simplified to a similar method to that used in the literature (with caveats defined) to give an indication of the most promising candidate coatings for further research.

CHAPTER 3 EXPERIMENTAL METHODOLGY

Includes extracts published in H. Sun, K. Cooke, G. Eitzinger, P. Hamilton & B. Pollet. *Development of PVD coatings for PEMFC metallic bipolar plates.* Thin Solid Films, 2012, 528, 199-204. Reprinted by permission.

3 EXPERIMENTAL METHODOLOGY

This chapter describes the type of substrate materials and PVD coatings used in this work. The experimental methods that were used to characterise these materials are then outlined.

3.1 Substrate Material

The AISI 316L stainless steel was purchased from ADVENT Research Materials Ltd., UK, (Catalogue No. FE694618). A typical analysis (ppm) of this material is: C < 300, Si < 1%, Mn < 2%, Ni 10–14%, Cr 16–18%, Mo 2–3%, S < 300, P < 450, Fe balance. The heat treatment condition for the foil was temper annealed. This type of stainless steel was selected as the substrate material for this work as it is widely available and has been reported as the bipolar plate material of choice in the literature (see section 2.6). The effects on the interfacial contact resistance (ICR) of two types of substrate modification were examined. First, physical surface roughening using three different grades of SiC paper (P400, P800, P1200) and 6 μm diamond paste was tested to discover at what level of surface roughness the ICR would dramatically increase, as described in the literature [118-120]. This was carried out to determine whether the AISI 316L 0.1 mm foil substrate would be influenced by this effect. Secondly, it was desirable to investigate the effects of photochemical etching which was expected to alter the chemical composition of the substrate surface. The effect of this alteration on the properties of the subsequently deposited PVD coating was of interest. The two modes of chemical etching used were a rapid ‘flash’ etch and a more substantial 0.2 mm etch. The exact process conditions used in the etching cannot be disclosed as they were the proprietary property of Precision Micro Ltd.

3.2 Physical Vapour Deposition (PVD)

Physical vapour deposition (PVD) is a generic term used to describe a variety of methods where a coating material is evaporated under partial vacuum and then condensed onto, for example, a metal, semiconductor or dielectric target surface to form a thin film coating. In this work Teer Coatings Ltd used a proprietary Closed Field Unbalanced Magnetron Sputter Ion Plating (CFUBMSIP) [195] arrangement as shown in Figure 3.1. This coating technique has also been used in the literature for the production of bipolar plate coatings [178-180, 188, 196].

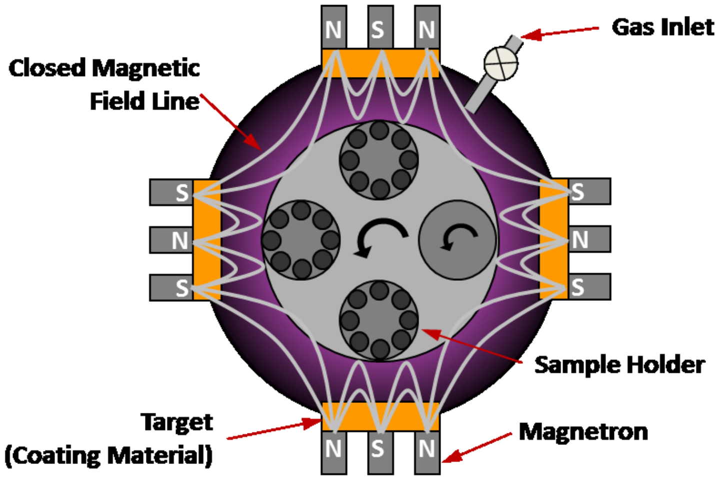

Figure 3.1 Diagram of a Closed Field Unbalanced Magnetron Sputter Ion Plating (CFUBMSIP) System. Image courtesy of Teer Coatings Ltd. [195]

All the coatings for this work were deposited by Teer Coatings Ltd using a Teer UDP 650 system. This system enables coating deposition to be carried out using a high density of low energy bombarding ions, which can result in very dense, non-columnar coating structures with low internal stresses (with the appropriate parameters). Prior to coating, the samples were ultrasonically cleaned in acetone for 15 – 20 minutes and then removed from the solvent and warm air dried or wiped dry with lint-free tissue. They were placed into the coating chamber which was then pumped down to a pressure of typically 2.7 –4.7 Pa (2.0 - 3.5 x 10^{-5} torr). At the start of the coating process, argon gas was admitted, via a mass flow controller, typically operating in the range 15 - 25 sccm, allowing the chamber to reach a pressure between 0.107 – 0.27 Pa (8.0 x10^{-4} – 2.0 x10^{-3} torr) depending on the coating required. The typical substrate temperatures reached during the deposition processes were in the range of 250 – 300 °C and no auxiliary heating process was required. Typically, ion cleaning of the substrate was carried out by applying a pulsed DC bias voltage of -350 V to -400 V to the sample with low magnetron target currents of 0.2 – 0.4 A. The deposition processes generally involved reducing the sample voltage to 50 – 60 V and increasing the magnetron target currents to approximately 4 – 7 A. Exact conditions were deliberately varied for each sample. For the nitride based coatings an optical emission monitor (OEM) system was used to control the metal nitride stoichiometric ratio. This measures the intensity of a metallic emission line in the plasma above the target surface during sputtering, and feeds back to a piezoelectric valve which controls the nitrogen input. The flow valve is rapidly opened and shut repeatedly to keep the chosen emission line at the same intensity, which regulates the amount of N_2 in the chamber and keeps the coating's stoichiometry constant.

The coating materials examined in this work were TiN, CrN, ZrN, Graphit-iC™, TiN+C, CrN+C and Au. The patented Graphit-iC™ coating [197] consisted of a Cr transition layer followed by a Cr/amorphous carbon second layer. This amorphous carbon has a high sp^2 bonded carbon content which is electrically conducting.

The thickness of the coatings was measured using a ball crater technique [198] as shown in Figure 3.2. A small crater in the coating was formed using a ball of known diameter and a little diamond paste. The resulting crater provides a tapered cross-section of the film when viewed under an optical microscope from which the film thickness can be calculated. The error associated with this measurement is typically ± 100 nm.

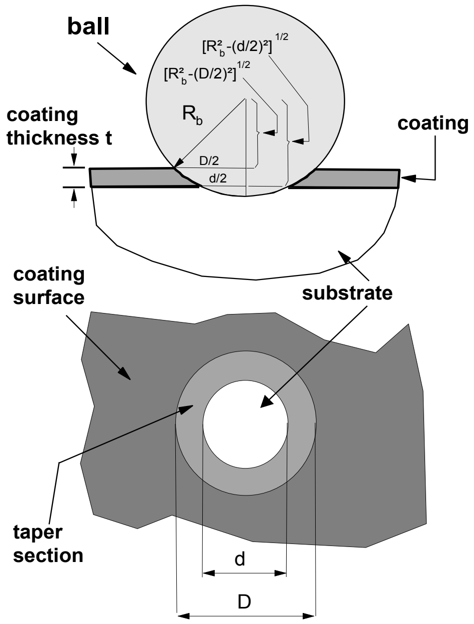

Figure 3.2 Schematic diagram of the crater and the geometries used for coating thickness determination Image courtesy of Teer Coatings Ltd.

There are a significant number of factors that need to be considered in order to calculate the cost of a PVD coating. However, many of these are commercially sensitive and so it was not possible to obtain precise values for this work. Costs that are common to all coatings include equipment depreciation, labour, utilities (power, water, compressed air) and the type of process used (batch, semi-continuous or continuous). The coating itself will also affect the cost according to the sputter target cost, reactive gases used, coating thickness and deposition rate. Relative target material costs are shown Figure 3.3. It was observed that on a materials basis alone, gold coatings would need to be around three orders of magnitude thinner than alternative coatings, in the realm of nanometers, to be commercially viable.

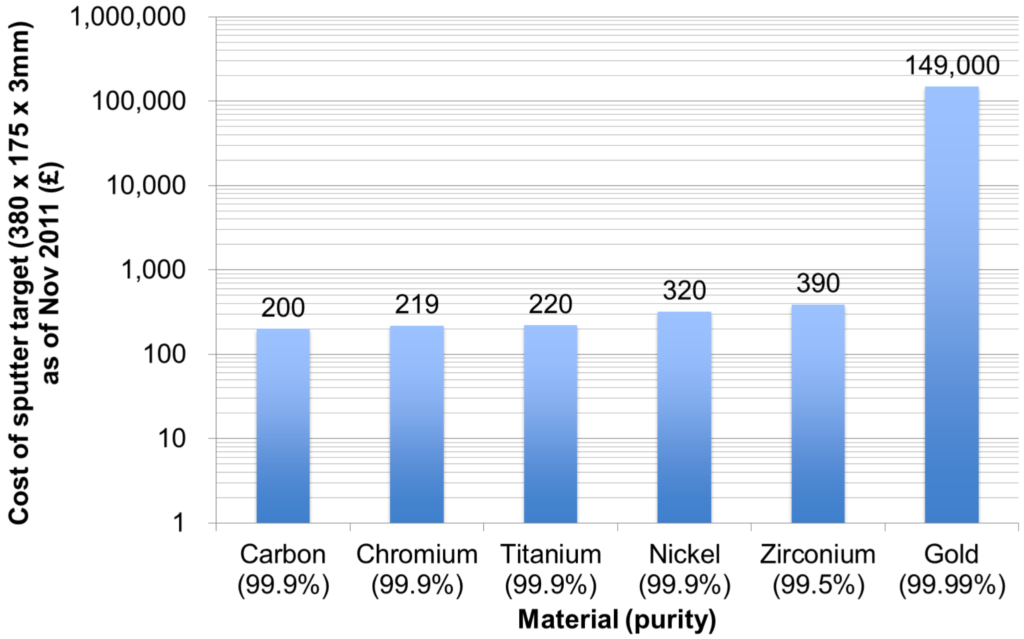

Figure 3.3 Graph shows material costs for 380 x 175 x 3 mm sputter targets used for coating [199].

3.3 Ex-situ Characterisation

The physical, microstructural, mechanical, electronic and chemical properties of the bipolar plate coating materials were characterised using the following methods.

3.3.1 Surface Metrology

An optical interferometry technique; which has not been widely used in this particular field thus far, was used to measure the surface topography of coated and uncoated samples. This measures the interference of light beams to determine differences in surface height over a large surface area. Interferometric analyses of surface topography were performed under ambient conditions using a MicroXAM interferometer (Omniscan, UK) using a white light source. Samples were imaged using a 50x objective lens with a 2x field-of-view multiplier. The data was displayed in visual and graphical arrangements with average 3D surface roughness (Sa) values (ISO/DIS 25178-2 & ASME B46.1) using SPIP v4.4.3.0 software. A slope correction function was performed with a polynomial plane fit before the calculation of the Sa to remove any effect of the sample being unevenly placed.

3.3.2 Atomic Force Microscopy

Atomic Force Microscopy (AFM) has been used in the literature to analyse the surface morphology of bipolar plate coatings [179, 200, 201]. In this work a NanoWizard® II from JPK Instruments was used in intermittent contact mode at 18 °C and 35% relative humidity. This system used rectangular Si cantilevers with pyramidal tips of 10 nm nominal radius (PPP-NCL, Nanosensors, Switzerland) to scan across the surface of the sample. The deflection of this cantilever can be measured using a laser to detect nanoscale changes in surface height. This equipment was used to examine the surface morphology of some of the PVD coatings.

3.3.3 Water Contact Angle

The sessile water contact angles of the sample surfaces were measured, as often carried out in the literature [122, 180, 187], to determine the degree to which a material was hydrophilic or hydrophobic, as it plays a large role in the removal of water from the flow field. A droplet was created using a very fine needle and syringe fitted with a screw-thread micrometer. The droplet angle was measured at room temperature using a high magnification camera and custom-built contact angle measurement software (courtesy of Teer Coatings Ltd). At least three droplets were created on each of the materials and the average water contact angle was taken. The software was unable to accurately measure contact angles of < 30°.

3.3.4 Raman Spectroscopy

This technique measures the Raman scattering, of monochromatic light from a laser. The resulting change in energy of the laser photons provides information about the molecular vibrations and can be correlated to the chemical bonds within molecules. This technique has previously been used in the literature to characterise carbon coatings [179, 189]. In this work Raman spectroscopy was used to examine the effect of oxygen plasma treatment on the type of carbon bonding present in the carbon coating. Raman spectra of samples were obtained using a WiTec Alpha 300R (LOT Oriel, UK) confocal Raman microscope operating a 0.3 W single frequency 785 nm diode laser (Toptica Photonics, Germany) and an Acton SP2300 triple grating monochromator/spectrograph (Princeton Instruments, USA) over the wavenumber range 0 – 3,000 cm^{-1} at a mean resolution of 3 cm^{-1}. Mean spectra were composed of 20 accumulations, acquiring individual spectra using an integration time of 0.5 s.

3.3.5 X-ray Photoelectron Spectroscopy

X-ray Photoelectron Spectroscopy (XPS), also known as Electron Spectroscopy for Chemical Analysis (ESCA), has been used to measure the elemental composition of bipolar plate coatings in the literature [152, 202, 203]. The process involves exposing the surface to X-rays and measuring the kinetic energy and number of electrons that escape from the surface. In this work a VG ESCALAB 250 at Leeds EPSRC Nanoscience and Nanotechnology Research Equipment Facility (LENNF) was used which utilized a monochromated Al K alpha X-ray source. The spot size was ~500 µm with a power of 150 W. Detailed scans were performed at a pass energy of 20 eV and surveys at 150 eV. Peak decomposition and analysis was carried out using CasaXPS software. In this work XPS was used to examine the elemental composition of the coatings, with a particular interest in any surface oxides which are known to increase the interfacial contact resistance.

3.3.6 Interfacial Contact Resistance

The interfacial contact resistance (ICR) values were determined using the experimental setup shown in Figure 3.4., which is similar to that originally used by Davies et al.[116]. In this arrangement, the sample was placed between two gas diffusion layers (GDLs), which were sandwiched between two cylindrical 1 cm^2 gold coated copper electrodes. The GDLs and the coated samples were then compressed and the total resistance was measured at a particular pressure (140 N/cm^2 was selected, being typical of the mechanical loading conditions in a fuel cell stack). The resistance of the GDL alone was also measured in advance, and the value was subtracted from the total resistance and divided by two to give the ICR of one surface. The ICR after potentiostatic testing was also measured to observe any changes after exposure to the corrosion conditions. This testing method assumes that the bulk conductivity of the carbon GDL is negligible. Thus, the ICR results given here are the corrected value between the sample and GDLs based on the assumptions described above.

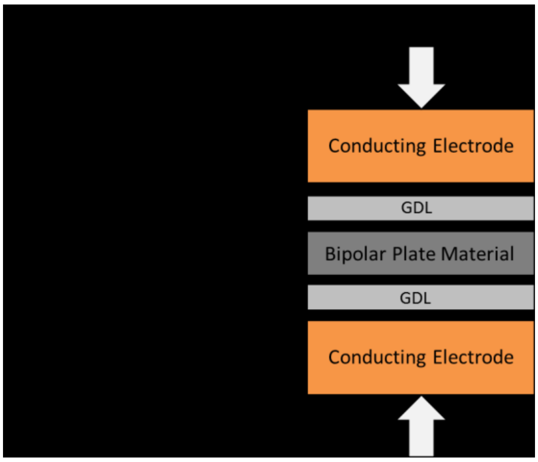

Figure 3.4 Arrangement for measuring the interfacial contact resistance (ICR)

The equipment used during this study included an Instron® MicroTester (Model No. 5848) compression machine with a 2 kN load cell and a Thurlby Thandar BS407 micro ohm meter which utilised a four wire measurement method. Toray H120 GDLs were used and were conditioned before testing by compressing three times to 140 N/cm^2. Figure 3.5 shows the drop in resistance and displacement of a single GDL over time whilst under controlled load of 140 N. A noticeable change in plate displacement was observed over the first 60 s followed by a lower rate of displacement as the GDL continued to be compressed further up to the maximum time of 600 s. This rate of displacement change was comparable to the rate of change in the through plane resistance. This suggests that the as the GDL material relaxes under compression, more contact points are made between fibres, which in turn lowers the through plane resistance. Due to this relaxation of the GDL after setting the load, all samples' resistance values were recorded after 180 s.

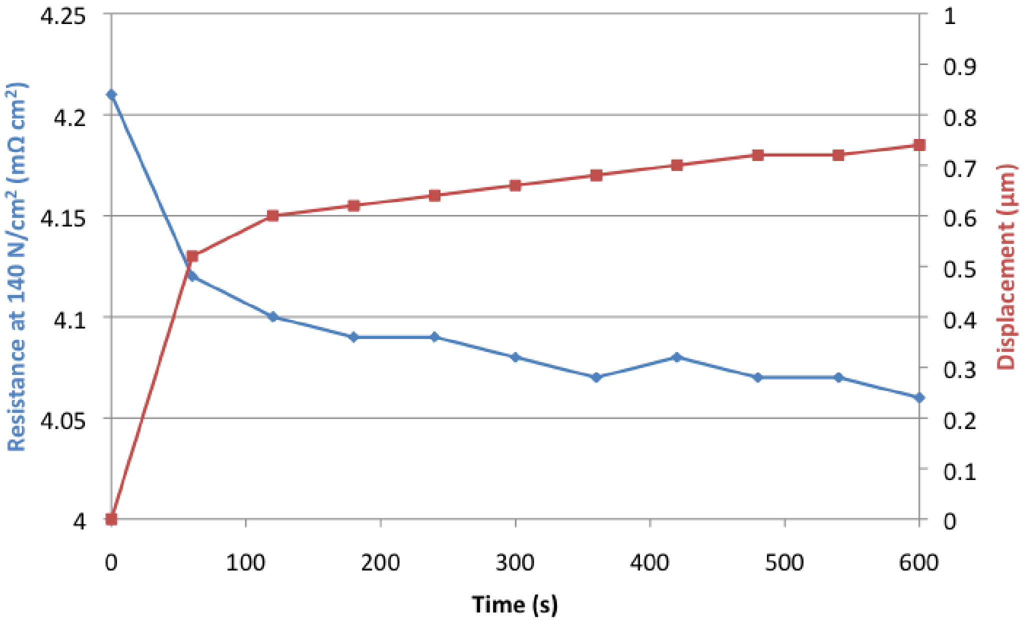

Figure 3.5 Change in resistance and plate displacement over time with a controlled 140 N/cm^2 load for a single Toray H120 GDL

3.3.7 Electrochemical Characterisation

Corrosion resistance is an important factor in gauging the likely practical performance of bipolar plate materials [123]. Potentiodynamic experiments were carried out using an Autolab PGSTAT302N potentiostat connected to a computer. The electrochemical cell was a Bio-logic 250 ml jacketed flat corrosion cell, with a 1 cm^2 sample surface area, and was linked to a thermostatically controlled bath. The cell was placed in a Faraday cage to minimise any electrical interference from surrounding equipment. A C10-P5 Thermo Scientific circulating water bath was used to maintain the temperature of the cell at 70 °C. A three electrode setup was used as shown in Figure 3.6 where the working electrode was the as-received AISI 316L 0.1 mm foil which had been coated by the PVD equipment described above, and was cleaned with acetone and dried prior to immersion. A Hg/Hg_2SO_4/K_2SO_{4sat} (MSE) was used (0.68 V/RHE) as the reference electrode rather than a Saturated Calomel

Electrode (SCE, 0.241 V/RHE) to avoid any possible chloride contamination [124]. A platinum mesh which had a considerably greater geometric surface area than that of the working electrode was used as the counter electrode. The electrolyte used was 250 ml of 0.5M H_2SO_4 as used elsewhere in the literature [117, 164].

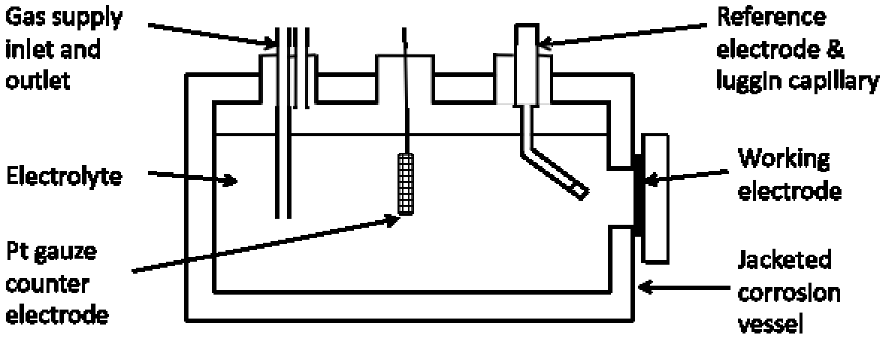

Figure 3.6 A schematic of the three electrode set up

The procedure involved bubbling the electrolyte with either air or hydrogen for 20 mins after which the delivery tube was withdrawn from the solution but left within the electrochemical cell to maintain the chosen atmosphere. The open circuit potential (OCP) was then recorded for 40 mins. Following this, a potentiodynamic scan was then initiated recorded from 250 mV below the OCP value at a scan rate of 1 mVs^{-1} until the measured current density reached ~ 10^{-2} A/cm^2 or 2 V/RHE. Potentiostatic measurements were also carried out at 1 V/RHE to simulate an extended time under fuel cell standby conditions. This potential was selected as it is more severe than the fuel cell operating potential of 0.8 V/RHE and it is plausible that the fuel cell may be under these conditions for extended periods of time.

3.4 Flow Field Design & Manufacture

The multiple serpentine flow field with the following parameters was designed using *AutoCAD* software as shown in Figure 3.7. The as-received plate materials were cut into 70 x 70 mm squares by the micro machinining department to correspond to the Paxitech test station cell dimensions. The plate thickness varied depending on the material and was kept the same as it was received (typically 2 - 3.5 mm). The flow fields were milled using a Matsuura LX-1 CNC milling machine. The multi serpentine design used a 0.6 mm diameter square end mills (CR/MS 2MSD00 50/60 from Mitsubishi Carbide). For composite and graphite plates the spindle speed was 50,000 rpm with a 0.1 mm depth of cut per pass and a feed rate of 700 mm per minute. For stainless steel plates, the spindle speed was 13,000 rpm with a 0.5 mm depth of cut per pass and a feed rate of 45 mm per minute.

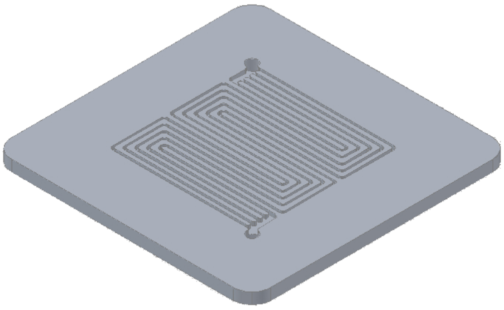

Description	Multiple Serpentine
Number of channels	5
Channel depth (mm)	1
Channel width (mm)	0.6
Land width (mm)	1
No. of 180° turns/channel	4
~Channel length (cm)	20

Figure 3.7 Isometric CAD View and Parameters of a Multiple Serpentine Flow Field Design

3.5 In-situ Characterisation

Single cell testing of bipolar plate materials using a fuel cell test station was carried out on a PaxiTech/Bio-logic FCT-50 test station as shown in Figure 3.8 to enable in-situ comparisons.

Commercially available graphite (Toyo Tanso) and composite (Bac2 EP1109) bipolar plate materials were used to provide a general benchmark against TiN and Graphit-iC™ coated 316L.

Figure 3.8 PaxiTech/Bio-logic FCT-50 Fuel Cell Test Station [204]

The test station was capable of controlling and measuring flow rates, relative humidity, temperature and the pressure of the reactant gases. It was also capable of measuring the voltage and current produced and electrical impedance, which enables the calculation of ohmic losses as discussed in Section 1. The anode and cathode flow field plates both used exactly the same flow field design, and were orientated in a counter flow arrangement. The voltage and PT100 temperature probes were modified or exchanged to fit into the side of the plates. The voltage sensors (2 mm diameter) were connected to copper wires (1 mm diameter) and a 1 mm PT100 (Platinum Resistance Thermometer) wire probe was used. The membrane electrode assembly (MEA) consisted of a Nafion 212 proton exchange membrane with two 34BC SGL Gas Diffusion Electrodes (GDE) with 0.4 mg/cm^2 Pt loading either side. This was fabricated in-house using some additional Nafion solution to assist binding the MEA together whilst in a hotpress. The active area was 16 cm^2 and PTFE gaskets were used to seal the cell. Cell compression has a significant impact on cell through-plane resistance, porosity of the GDL, water management and overall performance. In this work compression of cell was carried out by tightening the eight bolts to 5 Nm bolt torque. It is difficult to directly relate this to compressive pressure (e.g. MPa) as it is dependent on factors such as the number of bolts, torque per screw, surface area, frictional forces and material stiffness. Consequently the internal compression was also measured post testing using Pressurex™ paper.

The MEA was initially activated by maintaining the cell voltage at 0.6 V for several hours until the current stabilized. During the testing the cell temperature was maintained at 70 °C with the fuel lines kept slightly hotter to avoid any potential condensation of water prior to the gases entering the cell. The relative humidity of both anode and cathode gas streams was maintained at 45 % with inlet flow rates of hydrogen and oxygen of 120 ml/min and 300 ml/min respectively. Hydrogen and air back pressures were kept at 2 Bar. The purity of the hydrogen used was 99.999 %. A schematic of the single cell test station with parameters is shown in Figure 3.9. 20 quick initial polarisation curves (also known as IV curves) were performed between OCV and 0.25 V at 50 mV/s to make sure the MEA performance was stable followed by a recorded slower scan at 1 mV/s.

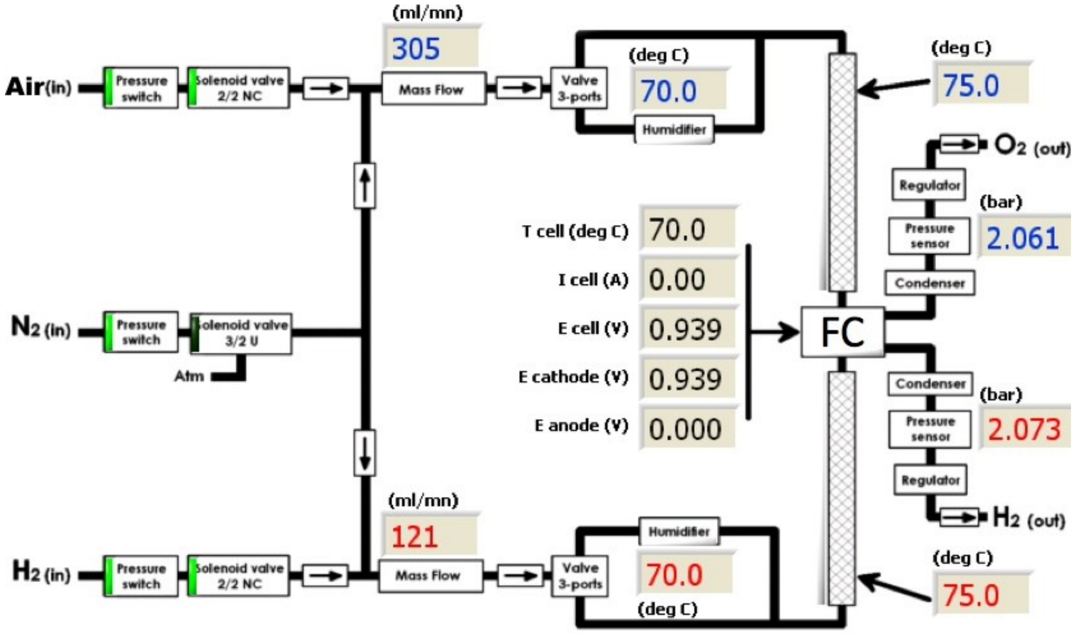

Figure 3.9 Schematic of PaxiTech/Bio-logic FCT-50 Fuel Cell Test Station from Fuel Cell Software

CHAPTER 4
INTERFACIAL CONTACT RESISTANCE

Includes extracts previously published in H. Sun, K. Cooke, G. Eitzinger, P. Hamilton & B. Pollet. *Development of PVD coatings for PEMFC metallic bipolar plates.* Thin Solid Films, 2012, 528, 199-204. Reprinted by permission.

4 INTERFACIAL CONTACT RESISTANCE

Using the methodology previously described in Section 3.3.6, this chapter examines factors affecting the interfacial contact resistance (ICR) of PVD coatings. These factors included the effect of substrate modification, coating type, thickness, stoichiometry, post coating treatments, multilayer coatings and corrosion. The significance of ICR on the in-situ performance of a single cell was also briefly examined.

4.1 Substrate modification

The substrate properties often play a significant role in the effectiveness of any PVD coating. Therefore it was desirable to investigate the effects of altering the surface roughness and chemical composition of the surface on the ICR.

4.1.1 Surface Roughness

As highlighted in Section 2.5.2, it has been well documented in the literature that surface roughness can have substantial effect on the ICR particularly with very smooth surfaces. To modify the surface roughness, the surface of two sets of 0.5 mm AISI 316L was polished with various grades of SiC paper and diamond paste. Figure 4.1 shows a similar trend to that seen in the literature, where a very smooth 316L surface (polished 6 μm diamond paste) has a detrimental effect on ICR. To investigate if this behaviour would be replicated with the addition of a PVD coating, a second set of the various grades of surface roughened substrate was coated with Graphit-iC™. The results show in contrast that the surface roughness of the substrate has no significant effect on the ICR of Graphit-iC™ coated samples. From this data, it would seem that a very conductive surface coating negates any effect on the ICR, as measured by compression between the selected GDL material, from changes in physical surface roughness.

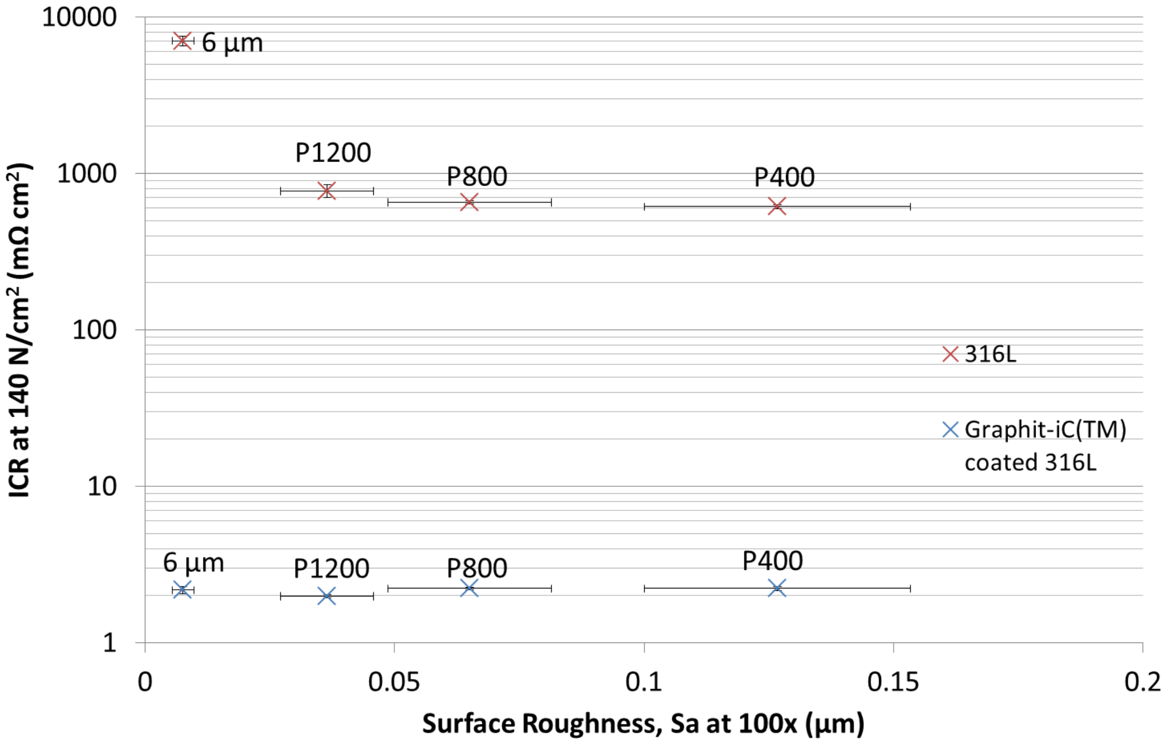

Figure 4.1 Influence of the surface roughness of 316L and Graphit-iC™ coated 316L on the ICR. X axis error bars show the standard deviation of 10 measurements after polishing with various grades of SiC paper or diamond paste. Y axis error bars show the standard deviation after three measurements.

Following this, the average Sa surface roughness of as-received 100 µm thick foil was measured as this is assumed to be a typical substrate material and condition for bipolar plates. With an average roughness of 0.036 µm from nine samples, it seems unlikely that the ICR will be dramatically altered by the surface roughness of the as-received foil even without conductive coatings. Figure 4.2 shows a representative image of the surface which reveals that the height distribution was essentially symmetrical with no visible grain boundaries as seen on thicker plates (see Figure 4.3). Striations on the surface were also visible which were attributed to the rolling manufacturing process.

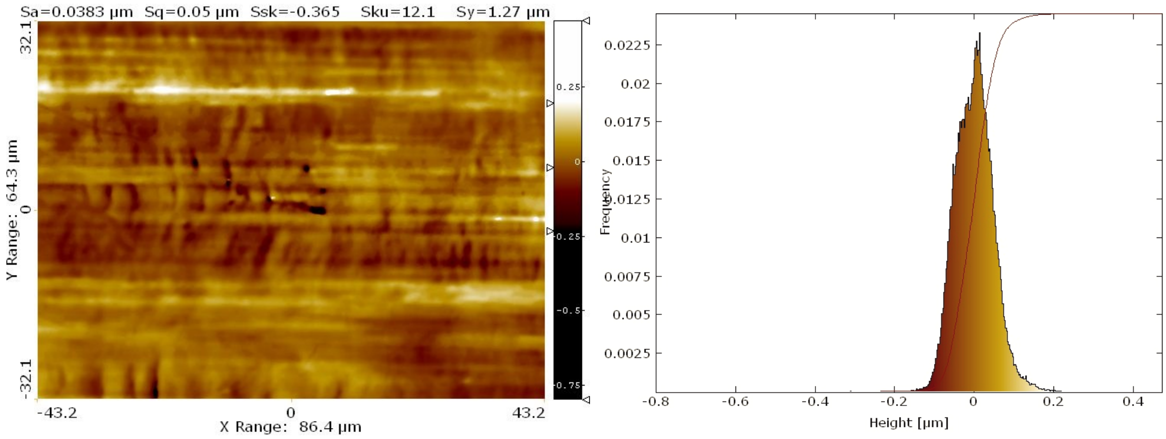

Figure 4.2 Interferometry image (left) and histogram (right) of 100 µm thick 316L foil surface

4.1.2 Photochemical Etching

Photochemical etching is one manufacturing process used to produce bipolar plates. Therefore a control ('masked') 1 mm annealed 2B AISI 316L plate and two grades of etched ('flash' etched and a 200 µm etch) courtesy of Precision Micro Ltd. were used to investigate the influence of this photochemical etching on the ICR of the uncoated and post treatment PVD coated substrate. Figure 4.3 shows that the histogram profile of the masked (as-received) substrate surface was narrow, suggesting a very flat surface. There was also a notable tail to the profile caused by the crevices (<1 µm deep) potentially at the grain boundaries. The Sa average surface roughness of 6 images was 0.21 µm. The difference between this masked plate and the 100 µm foil shown in Figure 4.2 was attributed to different manufacturing conditions. The histogram profile for the flash etched surface was broader than the masked surface which was symptomatic of a wider variety of surface heights (in the range of ~2 µm). Circular pitting was observed which was attibuted to the corrosive mechanism of photochemical etching. The Sa average surface roughness of 5 images was slightly rougher at 0.26 µm. The histogram profile for the 200 µm etched surface condition was broader still due to the continued corrosion of the surface during etching and a wider variety in surface heights ranging over 2.8 µm. The Sa average surface roughness of 6 images was 0.37 µm. These substrate conditions were then coated with 1 µm TiN and the surface roughness measured. The resulting roughness values are shown in Figure 4.4 and compared against the uncoated substrate conditions. As can be seen, the roughness of PVD coated substrate conditions was consistently higher, which was attributed to geometric shading where the surface peaks are more accesible than the troughs to the coating flux and thereby increase the difference in surface height.

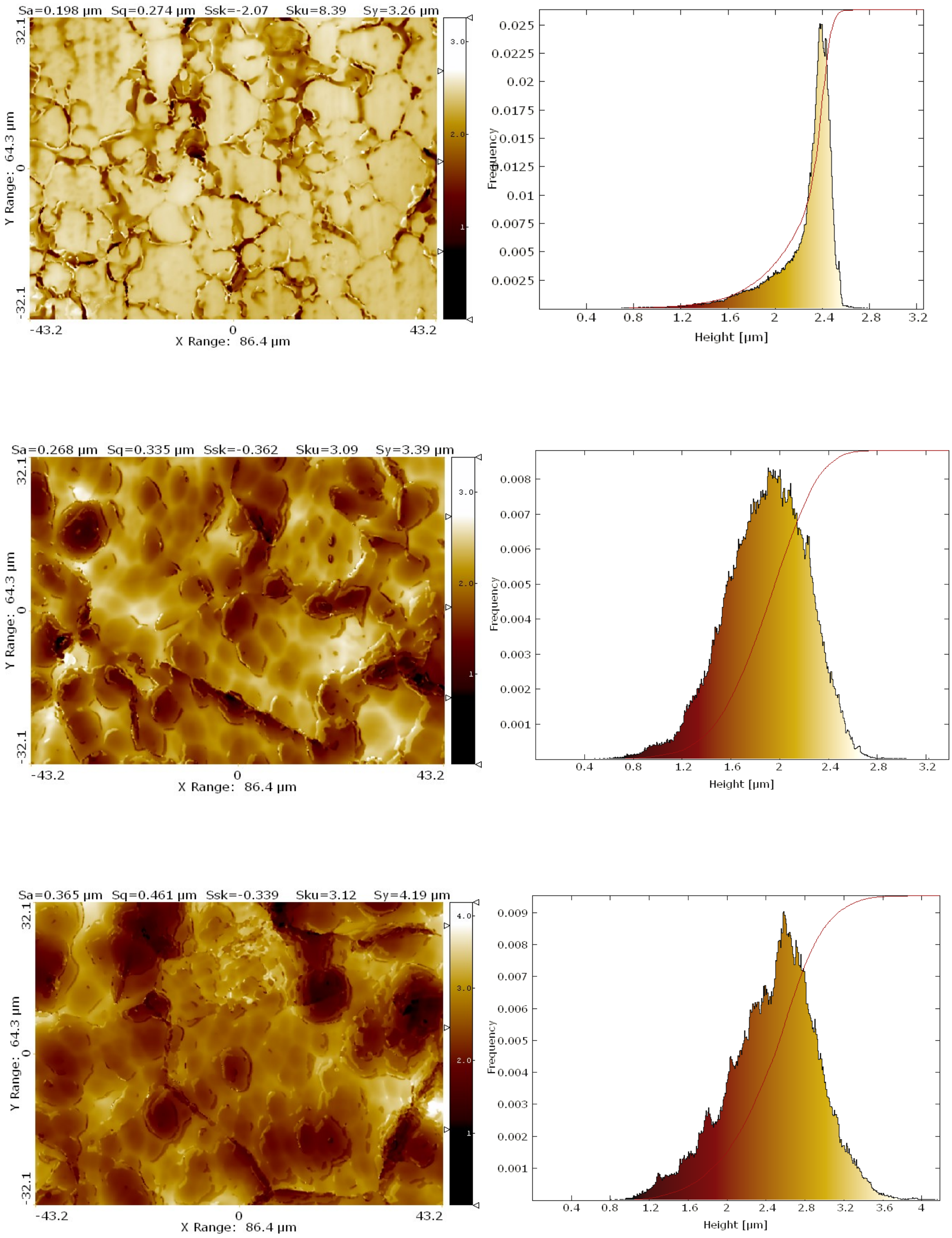

Figure 4.3 Representive 2D interferometry images and histograms of Masked (top), Flash Etched (middle) and 200 µm Etched SS316L (bottom) at 100x magnification

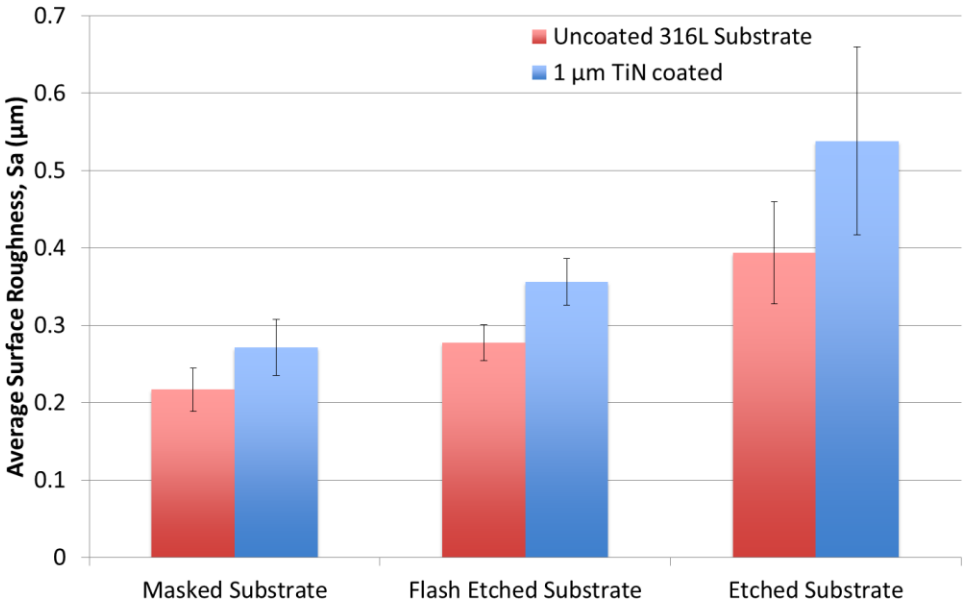

Figure 4.4 Graph of average surface roughness (Sa) at 100x magnification of masked, flash etched and 200 µm etched 316L substrates with and without a 1 µm coating of TiN. Error bars show the standard deviation of 10 images for each condition

Figure 4.5 shows that both flash etching and 200 µm deep etching of the substrate resulted in a significant decrease in the ICR compared to the masked (control) condition. The improvement was furthermore directly related to the depth/time of etch, 200 µm resulting a greater improvement than the flash etched condition. The reason for this improvement is likely to be a chemical modification of the insulating passive oxide layer; however, this needs to be confirmed with an elemental characterisation technique such as XPS which is outside the scope of this work. A Graphit-iC™ coating was also deposited on to the masked, flash etched and 200 µm etched 1 mm substrate to investigate the effects of this substrate modification on the ICR of PVD coatings. Despite chemical etching initially reducing the resistance of bare substrate, presumably by modifying the passive oxide film; Figure 4.5 shows that etching the substrate before PVD coating gives no improvement in ICR over the non-etched control (masked) coated sample. This suggests that any chemical modification of the surface caused by chemical etching is made redundant by the PVD coating process. This may be due to ion cleaning by the argon sputtering process used to clean the substrate before coating, which will remove any passivating oxide layer on the photochemically etched substrate.

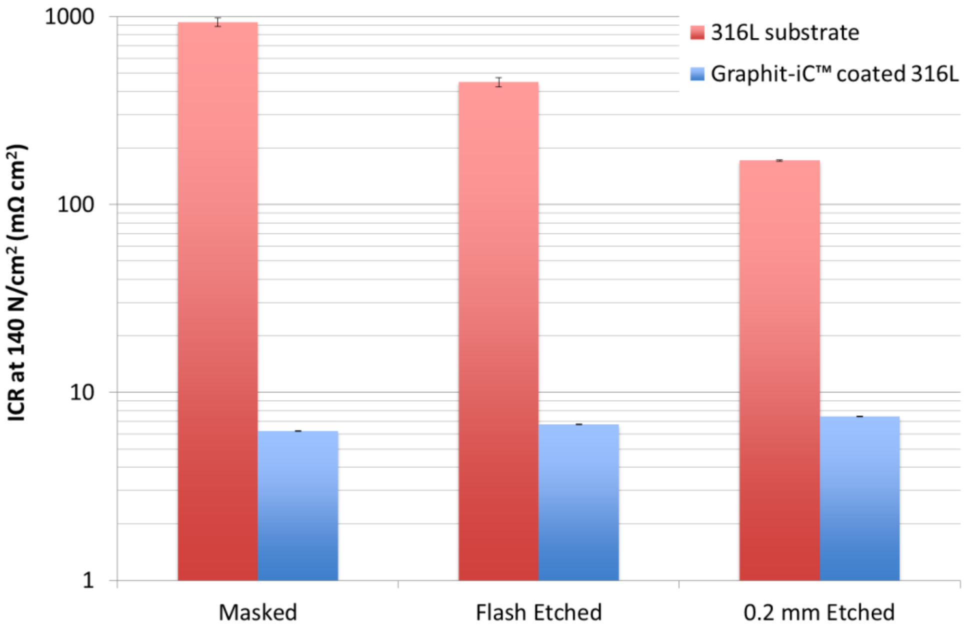

Figure 4.5 ICR of masked, flash etched and 200 µm etched 316L with and without a Graphit-iC™ coating at a compression of 140 N/cm^2

One disadvantage of this type of surface roughness measurement is its lack of ability to distinguish between different features contributing to surface roughness, such as crevices, pits and burs, which may have different contributions to the ICR. However, it is also unclear whether such a technique capable of discriminating between them is currently available.

4.2 PVD coatings

Figure 4.6 shows that the ICR of 1 µm PVD coatings were found to decrease in the following order; ZrN > TiN > CrN > Carbon based coatings > Au. The results for these seemed to be qualitatively consistent with the literature, although no study compared this particular of range coatings and the exact values cannot be directly compared as they are dependent on a number of factors such as level of compression, GDL, coating deposition parameters etc. Adding a thin layer (0.1 - 0.2 µm) of amorphous carbon to the surface of TiN and CrN coatings resulted in a striking reduction in the ICR. These multilayer coatings were comparable to the carbon based Graphit-iC™ coating. This suggested that the vast majority of the overall resistance of the metal nitride coatings could be attributed to the GDL/coating interface, rather than the coating/substrate interface. Consequently SEM and XPS were carried out to confirm if this was the case.

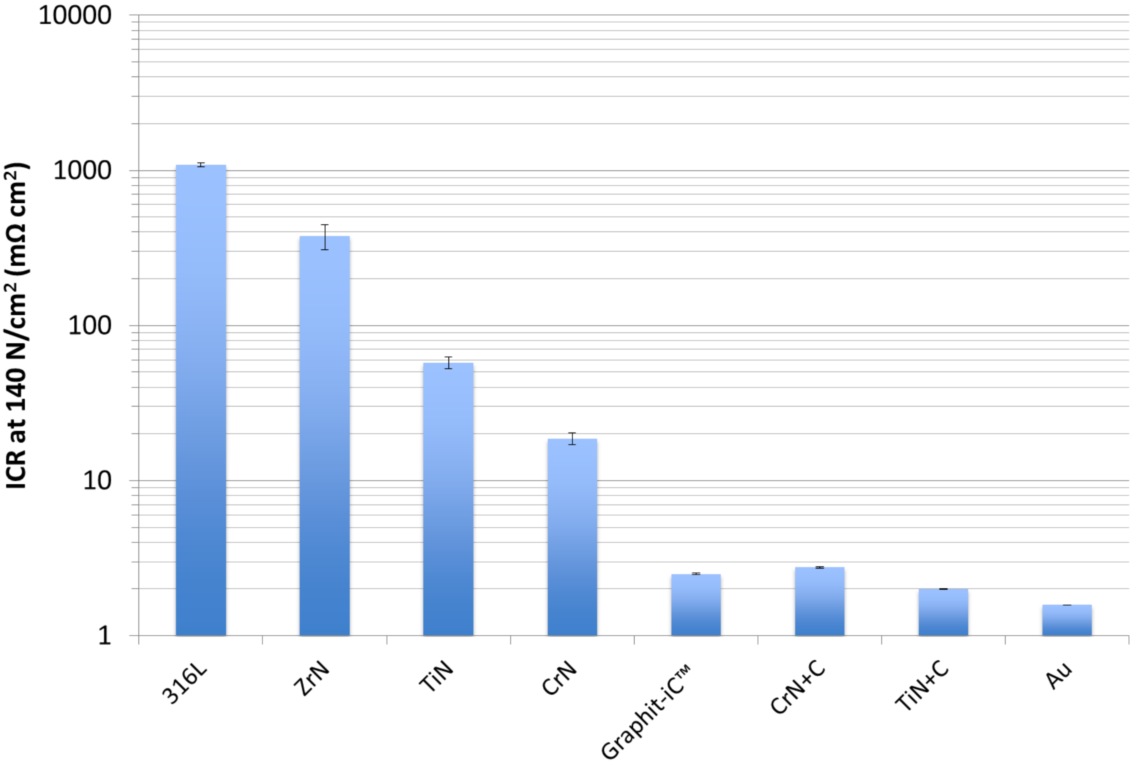

Figure 4.6 ICR of 316L, ZrN, TiN, CrN, Graphit-iC™, CrN+C, TiN+C and Au PVD coatings

4.2.1 Scanning Electron Microscopy

Scanning Electron Microscopy (SEM) was used to examine the structure of the multilayer coatings. Figure 4.7 shows the cross-section of a typical TiN+C coating on AISI 316L using a SEM and EDX line scan. It can be clearly seen that there is a well-defined interface between TiN coating and AISI 316L foil in addition to the carbon topcoat being well bonded to the TiN coating with both coatings having a dense structure. Compared with the amorphous carbon topcoat, the TiN has a columnar structure which is just visible. The dark line between the substrate and the coating was caused during sample preparation by the etchant used to create a clean cross section. The EDX line scan (shown adajent) confirmed the elemental composition of the coating.

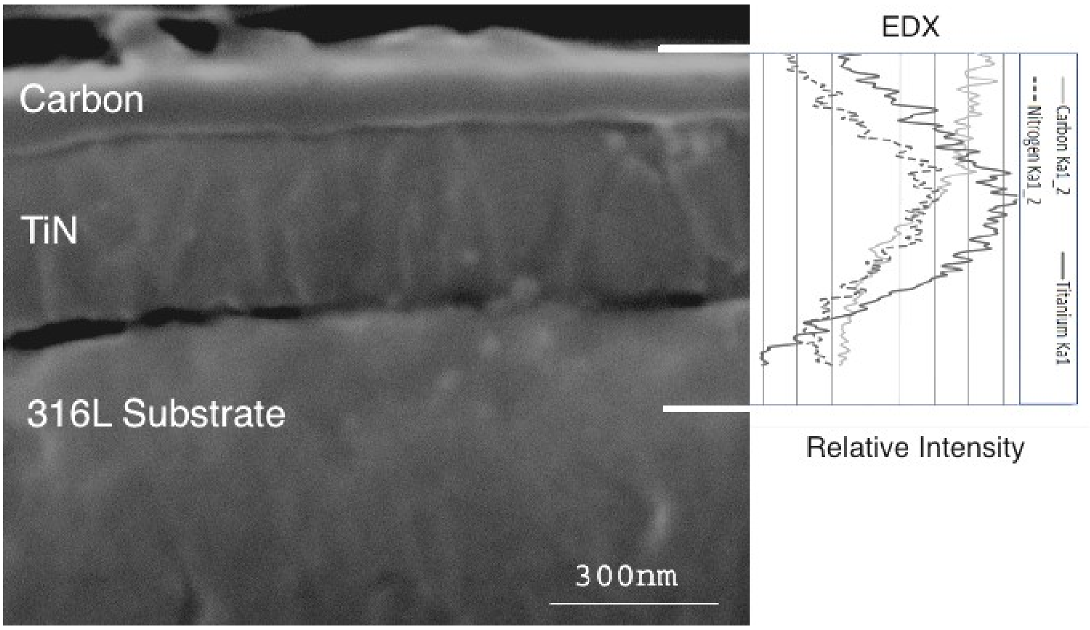

Figure 4.7 SEM image of 0.1 μm Ti / 0.4 μm TiN / 0.1 μm carbon multi layer coating cross section with EDX line scan

AFM examination after deposition of the coatings on the AISI 316L foil showed a smooth surface, which is beneficial for minimizing the surface area available for corrosion in the aggressive fuel cell environment. As shown in Figure 4.8, the average surface roughness (Ra) and RMS roughness (Rq) of a TiN coating (left) was 14.31 nm and 18.64 nm respectively using a 20 x 20 µm scan area. The addition of a PVD carbon top layer to the TiN (right) did not drastically modify the roughness and morphology with the average surface roughness (Ra) and RMS roughness (Rq) being 12.33 nm and 15.68 nm for the TiN+C coating. However, these findings are likely to be heavily influenced by roughness of the underlying substrate. Further work on very smooth silicon wafers may be required to determine if this is actually the case.

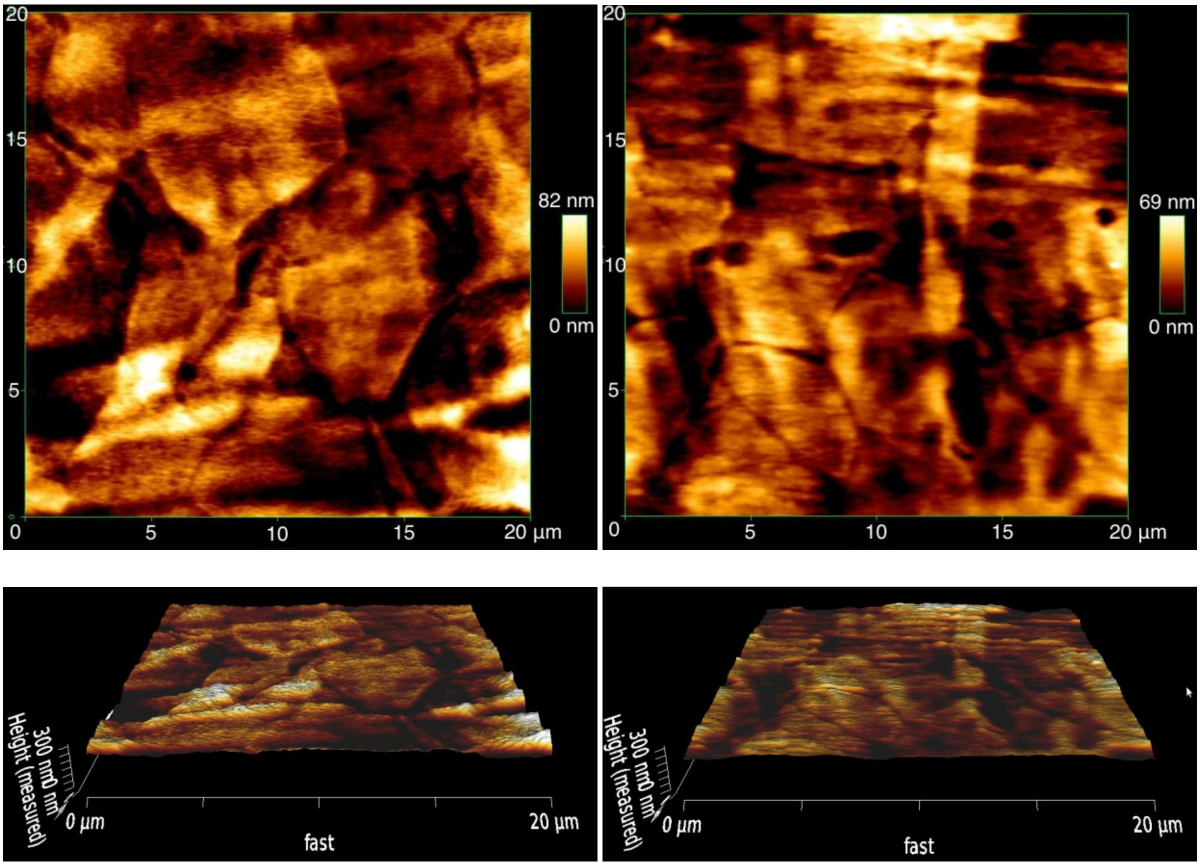

Figure 4.8 2D and 3D AFM images of TiN (left) and TiN+C (right) coatings on 316L foil substrate

A similar dense and well adhered coating structure was observed for the CrN+C coating shown in Figure 4.9. The surprisingly low nitrogen content of the CrN was attributed to the poor sensitivity of the EDX technique to lighter elements.

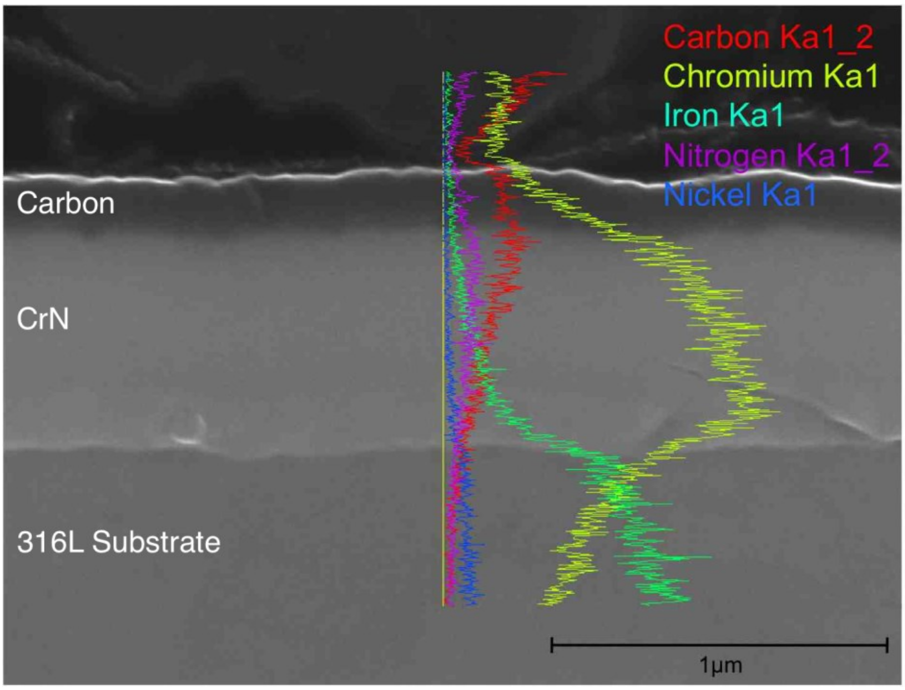

Figure 4.9 SEM image of CrN+C coating cross section on a 316L substrate with EDX elemental analysis.

4.2.2 X-ray Photoelectron Spectroscopy

Elemental quantification from X-ray Photoelectron Spectroscopy (XPS) surveys was used to help identify the reason for the variations in ICR across the PVD coatings. Figure 4.10 shows that the surface oxygen content of the nitride coatings was found to decrease in the order ZrN > TiN > CrN which was also consistent with the drop in ICR shown in Figure 4.6. Whilst further peak fitting can be done in future work to identify the particular oxides responsible and discard any contribution from the ineviteable surface carbon and oxygen contamination from the transport of such samples in normal atmospheres before XPS examination, it is perhaps helpful to view the 'contaminated' data as this is also the state of material during the ICR tests.

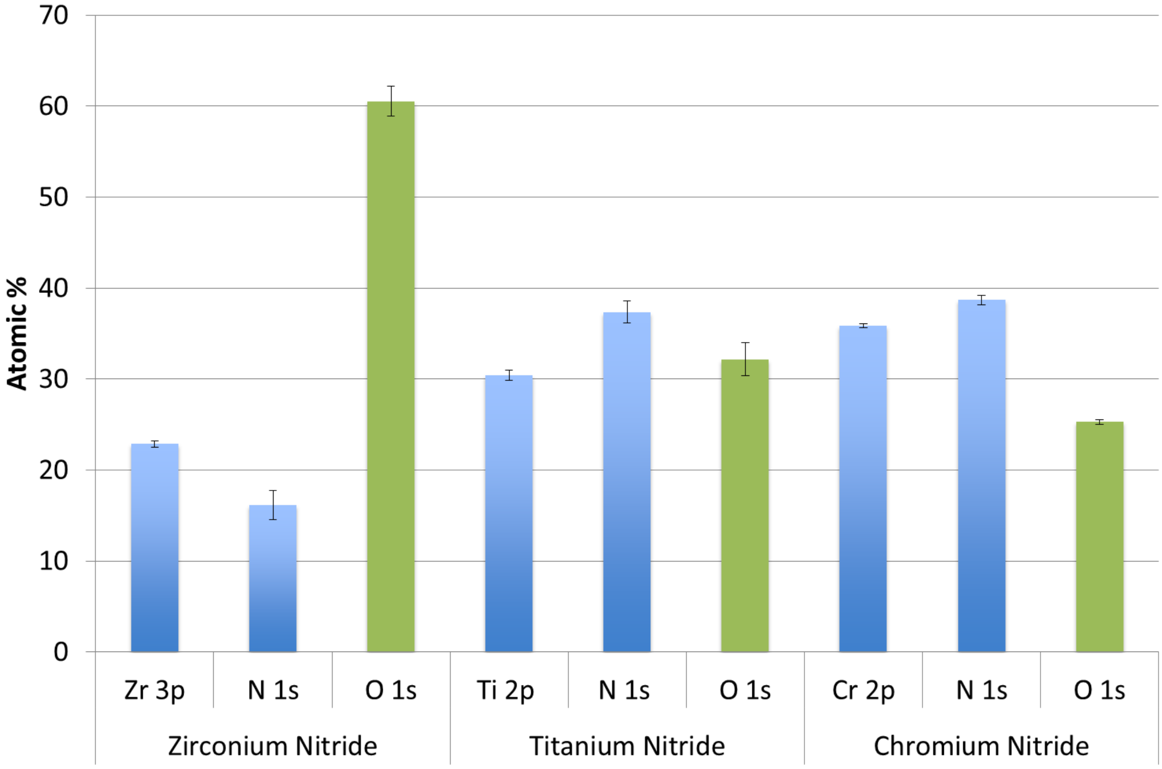

Figure 4.10 Elemental quantification from XPS survey of as-received ZrN, TiN and CrN coatings. Error bars show the standard deviation of three measurements (spot size of 400 µm each)

Figure 4.11 shows the elemental quantification from the XPS surveys of the carbon based and 10 nm Au coatings. All of the carbon based coatings (Graphit-iC™, CrN+C and TiN+C) showed very high levels of carbon (>80%) with very little surface oxygen (<15%). Trace amounts (<2%) of Cr or Ti were observed for CrN+C and TiN+C suggesting possible defect sites in the 0.1 – 0.2 µm thick carbon topcoat. In contrast, the Graphit-iC™ coating was doped by design with Cr and so low levels of Cr were expected. Unexpectedly, and in contrast to the nitride coatings, there was also a consistent low level of Ar in the carbon based coatings which attributed to trapped Ar in the coating originating from the PVD process. However, it is not clear why the Ar is only trapped in the carbon coatings and this result does not appear to have been reported elsewhere in the literature. The 10 nm Au coating showed no presence of Fe, Cr or Ti peaks, suggesting excellent surface coverage.

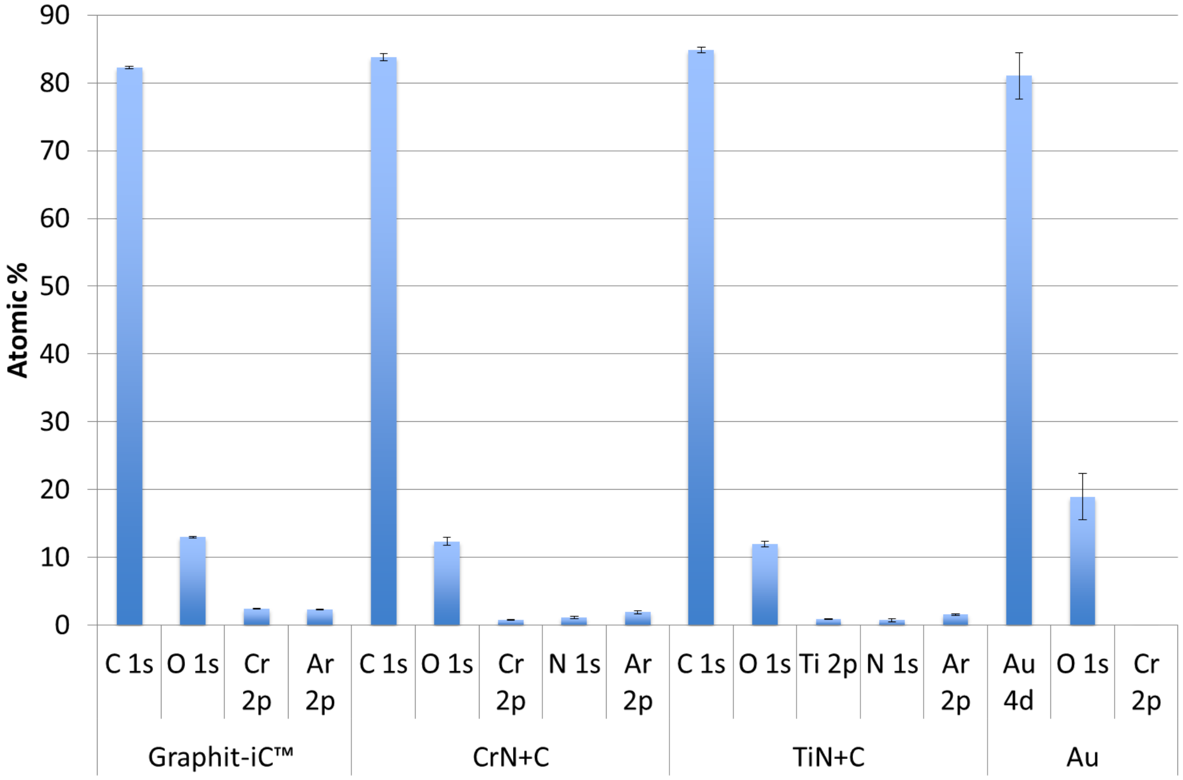

Figure 4.11 Elemental quantification from XPS survey of as-received Graphit-iC™, CrN+C, TiN+C and Au coatings. Error bars show the standard deviation of three measurements (spot size of 400 µm each)

4.2.3 Coating Thickness

Varying the coating thicknesses between 0.1 and 1.1 µm had no significant effect on the ICR of Graphit-iC™ coated 316L foil as shown in Figure 4.12. This shows that even a very thin coating of 0.1 µm can give the same benefit, in terms of ICR, compared to thicker (and more expensive) coatings.

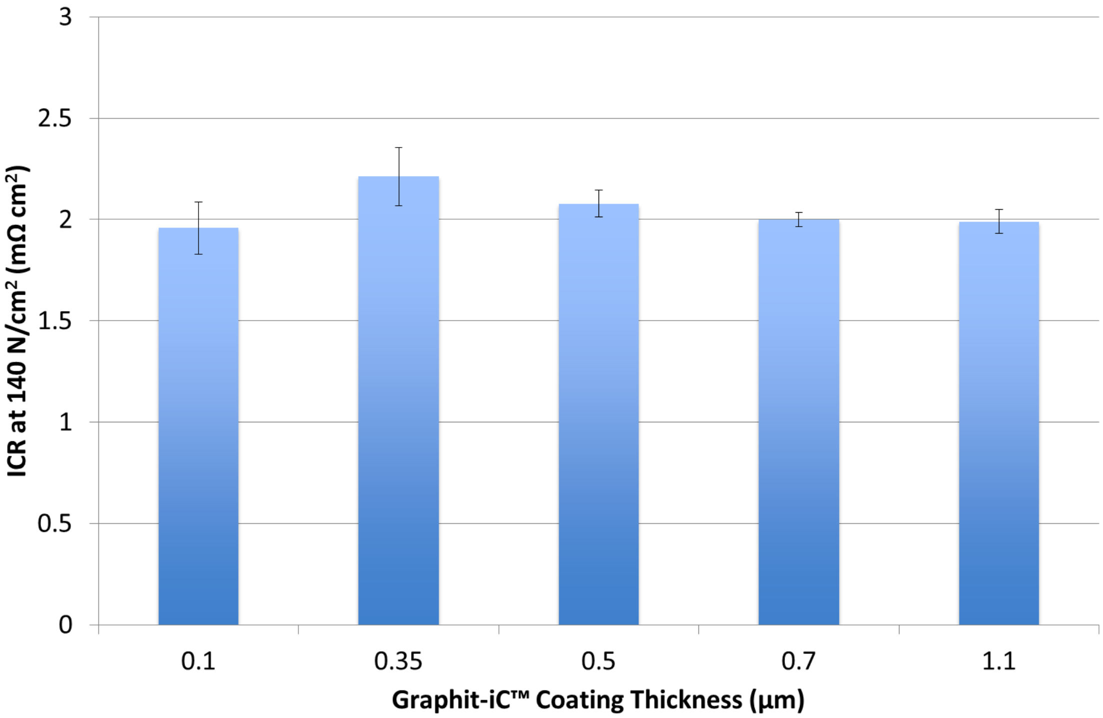

Figure 4.12 ICR of Graphit-iC™ coated 316L foil of varying thickness from 0.1 – 1.1 µm

4.2.4 Stoichiometry

It was observed that there was some variation in ICR for different TiN coatings. Therefore, various stoichiometries of TiN (55, 65, 75, 85% OEM) were deposited (on a slightly thicker 0.5 mm 316L substrate) to examine if unintentional changes in stoichiometry were a possible reason for this. CrN was also examined to see if a similar behaviour was observed. The optical emission monitor (OEM) method for controlling stoichiometry is described in Section 3.2. Figure 4.13 shows that the lowest ICR coatings were produced for TiN and CrN at 65 and 50% OEM respectively (CrN could potentially be lower). This would suggest that stochiometric nitrides were formed near these % OEM as the literature suggest the lowest resistivity is associated with stoichometric (1:1) as these coating contain fewer defects [154].

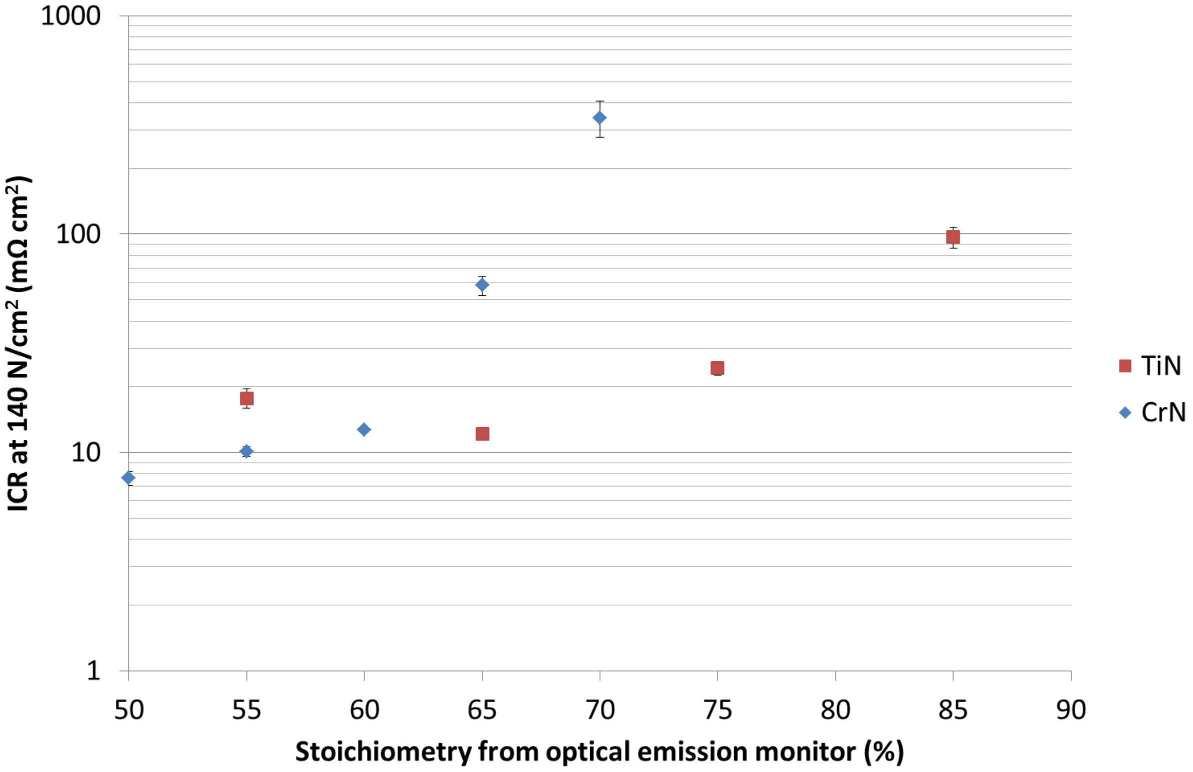

Figure 4.13 ICR of varying TiN and CrN stoichiometries obtained by altering the OEM % during coating

Whilst the ICR data showed the lowest resistance at 65% OEM for TiN (suggesting stoichiometric TiN), EDX data shown in Figure 4.14 suggested that stoichiometric TiN was not achieved under any of the % OEM conditions. The reason for this discrepancy was attributed to EDX analysis not being suitably sensitive to lighter elements such as nitrogen, resulting in a perceived lower nitrogen content. More accurate elemental analysis, such as Wavelength Dispersive X-ray Spectroscopy (WDX), should be carried out to identify the actual stoichiometry. This contribution to ICR from stoichiometry must also be explored in relation to surface oxides, as examined in section 4.2.2.

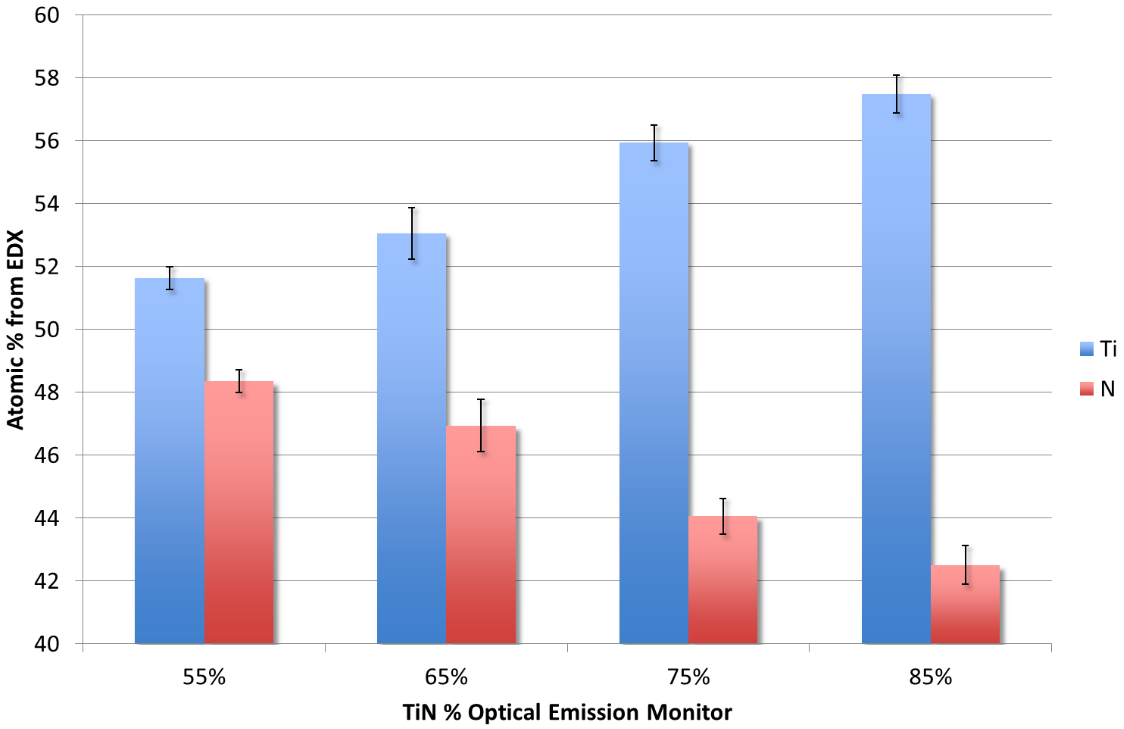

Figure 4.14 Average atomic % of Ti and N recorded from EDX of TiN stoichiometries of 55, 65, 75 and 85% OEM. Error bars show standard deviation of three measurements

4.2.5 Oxygen Plasma Treatment

Oxygen plasma treatment of carbon based coating has been proposed as a method to increase the hydrophilicity to enhance fuel cell performance, as shown in Table 2.10, and certainly after treatment the coating was indeed found to become extremely hydrophilic to the extent that it was not possible to measure the contact angle with the selected apparatus. However, given the detrimental effect of surface oxides on the ICR of metal nitride coatings found previously in Figure 4.10, it was desirable to investigate the effects of this treatment. It was found that after the carbon coating was exposed to oxygen plasma for 600 s, the ICR was increased significantly from 4.8 to 314 mΩ cm^2. To examine any chemical and physical changes caused by the oxygen plasma treatment, Raman spectroscopy, XPS and AFM were used.

The Raman spectra shown in Figure 4.15 showed two possible carbon peaks which according to Feng et al. [178], who also examined amorphous carbon, can be deconvoluted into two Gaussian curves, namely the D and G bands. These correspond to the Disordered band (from the defects in the graphite crystal at ~1390 cm^{-1}) and the Graphite band (from the graphite lattice at ~1568 cm^{-1}). In this case, for both samples, the intensity of the D-band was higher than that of the G band, which indicates that the quantity of the disordered carbon was larger than the amount of graphitic crystallites. This result was similar to the work of Feng et al. with the exception that this carbon coating contained comparatively more disordered carbon. The D-band is a feature common to all sp^2 hybridized disordered carbon materials [205]. However, more importantly, there was no significant difference between carbon coating and the carbon coating that had subsequently been treated with oxygen plasma for 600s. This suggested that if the process had modified the carbon coating, it had only affected the very surface of the coating and this method was not a suitable method of characterisation.

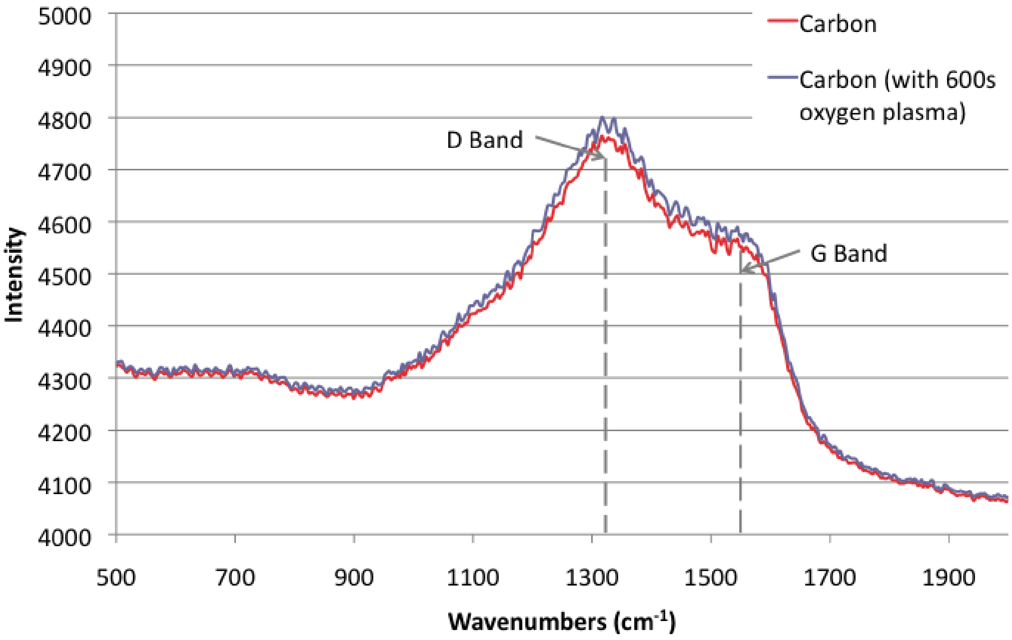

Figure 4.15 Raman spectra of carbon coating with and without O_2 plasma treatment

Subsequently an alternative XPS technique was used to examine the coatings. The results in Figure 4.16 and Figure 4.17 showed that the surface of the carbon coating which had been exposed to oxygen plasma had indeed been altered. Table 4.1 shows that over half the detected carbon was bonded to oxygen (C-O) after treatment. This finding seems to confirm that it is the oxygen content in the carbon coating that is responsible for the increase in ICR. It would be beneficial to examine the surface composition of a carbon based coating after in-situ tests to investigate if the same increase is observed.

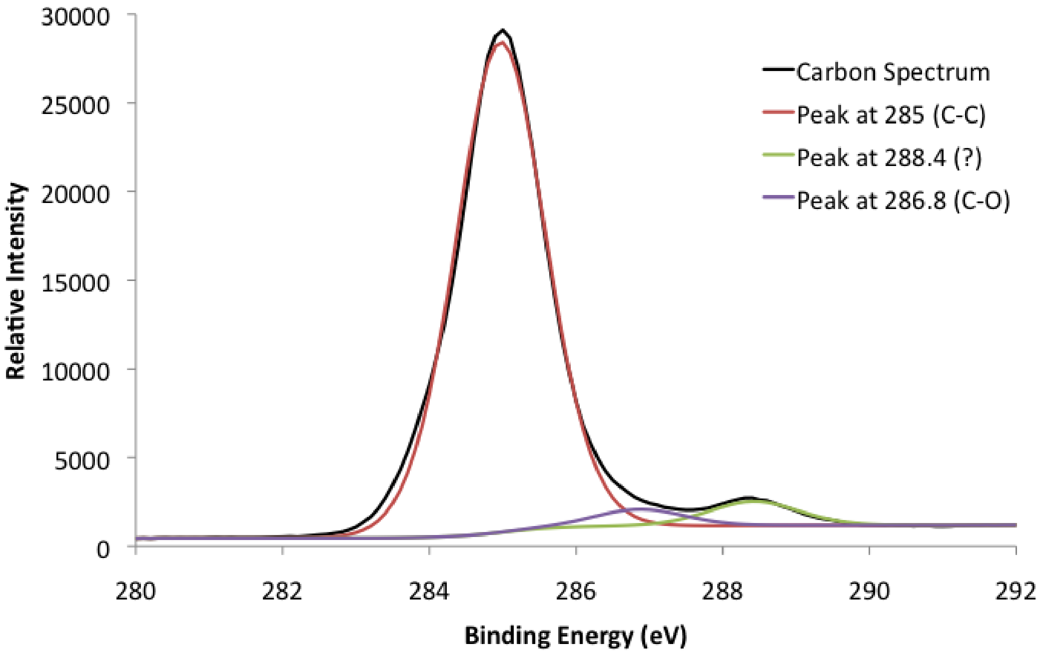

Figure 4.16 High resolution XPS C 1s spectra of carbon coating

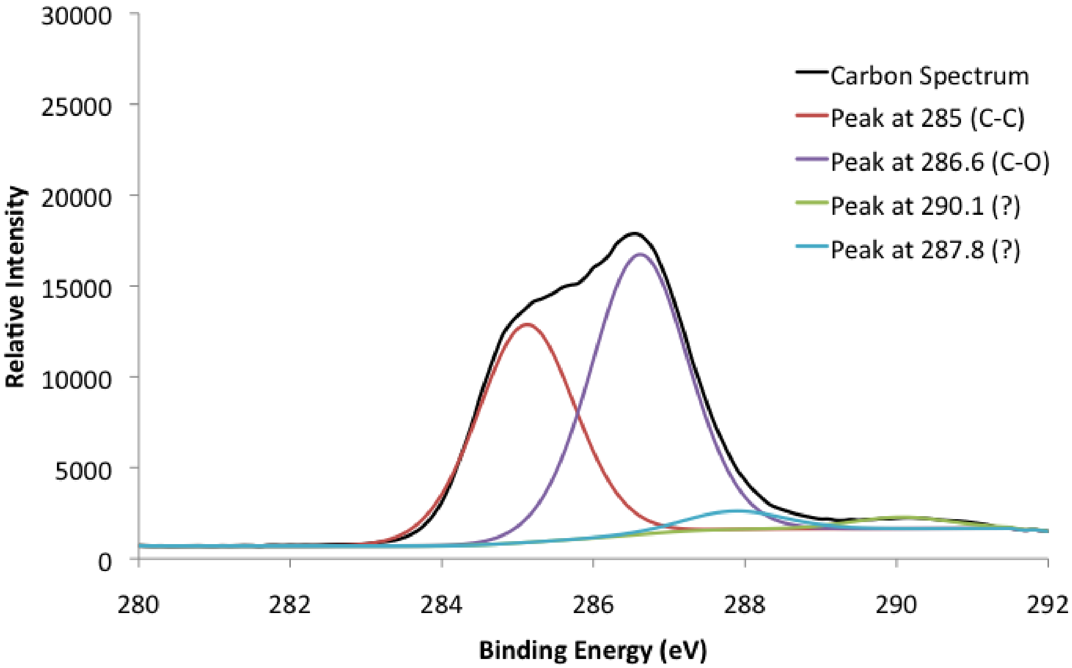

Figure 4.17 High resolution XPS C 1s spectra of O_2 plasma treated carbon

Table 4.1 Relative % of carbon species from carbon coating with and without oxygen plasma treatment

Peak	Relative %	Suggested Species [206]
Carbon (as-received)		
285	92.3	C-C
286.8	3.15	C-O
288.4	4.53	C=O
Carbon (after O_2 plasma treatment)		
285 (C-C)	41.32	C-C
286.6 (C-O)	53.04	C-O
287.8 (?)	3.48	?
290.1 (?)	2.16	Hydrocarbon contamination?

Atomic Force Microscopy (AFM) was finally used to examine the surface morphology of the carbon coating and investigate the effects of oxygen plasma treatment as the resolution of the interferometer was insufficient to detect any change on the surface of the coating.

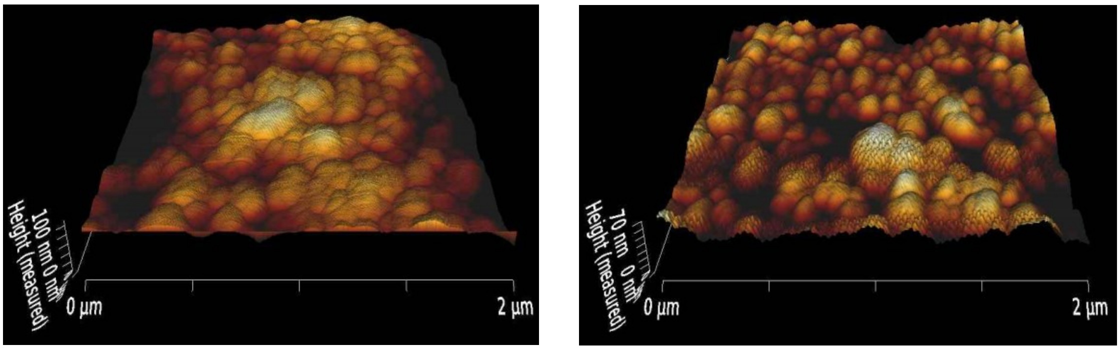

Figure 4.18 AFM images of as deposited 1 µm PVD carbon coating (left) and after 600 s of O_2 plasma treatment (right)

The AFM image of the carbon coating with no oxygen plasma treatment clearly showed the ‘cauliflower-like’ nature of the surface carbon film. After treatment however, the carbon coating showed a more bulbous structure with a rougher surface (Ra of 3.93 nm). This showed that the oxygen plasma treatment has both a chemical and physical effect on the carbon surface. However, the relative contributions from these two effects on the hydrophilicity and ICR should be explored in further work. Another area for investigation would be reducing the length of exposure time to study if it were possible to reduce the detrimental effects to ICR while keeping a measure of hydrophilicity.

4.3 Effect on in-situ performance

As noted in the first chapter, the ohmic losses associated with the ICR were reported to be a relatively small fraction of the overall fuel cell losses. Therefore the significance of ICR on actual fuel cell performance and a comparison with commercial Bac2 EP1109 composite and Toyo Tanso graphite plates, described in Section 2.4.1, was investigated by applying PVD coatings to bipolar plates that were then tested in a single cell. The plates were designed and manufactured as described in Section 3.4.

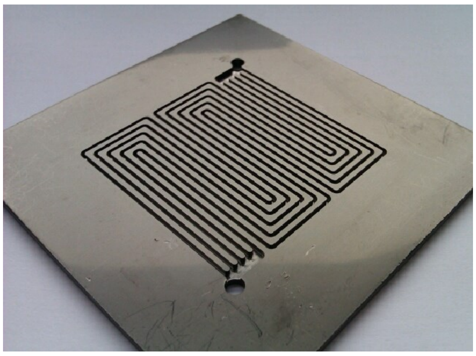

Figure 4.19 Photograph of CNC machined multiple serpentine flow field plate with Graphit-iC™ coating

Three general observations could be drawn from the I-V curves shown in Figure 4.20. First, at very low current densities (<0.1 A/cm^2) there was no distinguishable difference between the bipolar plate materials. This was expected, as the same MEA was used for each test and the voltage losses in this range were primarily caused by the catalyst overpotential. Secondly, at current densities of 0.1 – 1 A/cm^2 there were small differences in the slopes of the I-V curves for all bipolar plate materials. The resistance of the coatings and materials increased in the order of Graphit-iC™, Toyo Tanso < Bac2 EP1109 < TiN and was attributed to the through plane resistivity and contact resistance of the material. This was also qualitatively consistent with the ex-situ ICR results in Figure 4.6. Thirdly, at higher current densities of 1–1.5 A/cm^2, there was a marked change in behaviour which was attributed to mass transport issues and water flooding where the water contact angle of the material seemed to play a significant role. Materials that were more hydrophilic in the ex-situ tests such as the Graphit-iC™ coating (average contact angle of 39°), showed greater losses at high current densities compared with more hydrophobic coatings such as TiN (average contact angle of 96°) using this particular flow field. With regards to peak power, bipolar plate materials were found to alter peak performance by up to ~15% which was attributed to both the ICR and the water contact angle of the bipolar plate material. A study of the influence of coating water contact angle on in-situ performance taking into account the flow field, GDL and long term stability should be carried out in the future. Manufacturing the plates via a more realistic route would also be of some benefit to improve the validity of the in-situ tests.

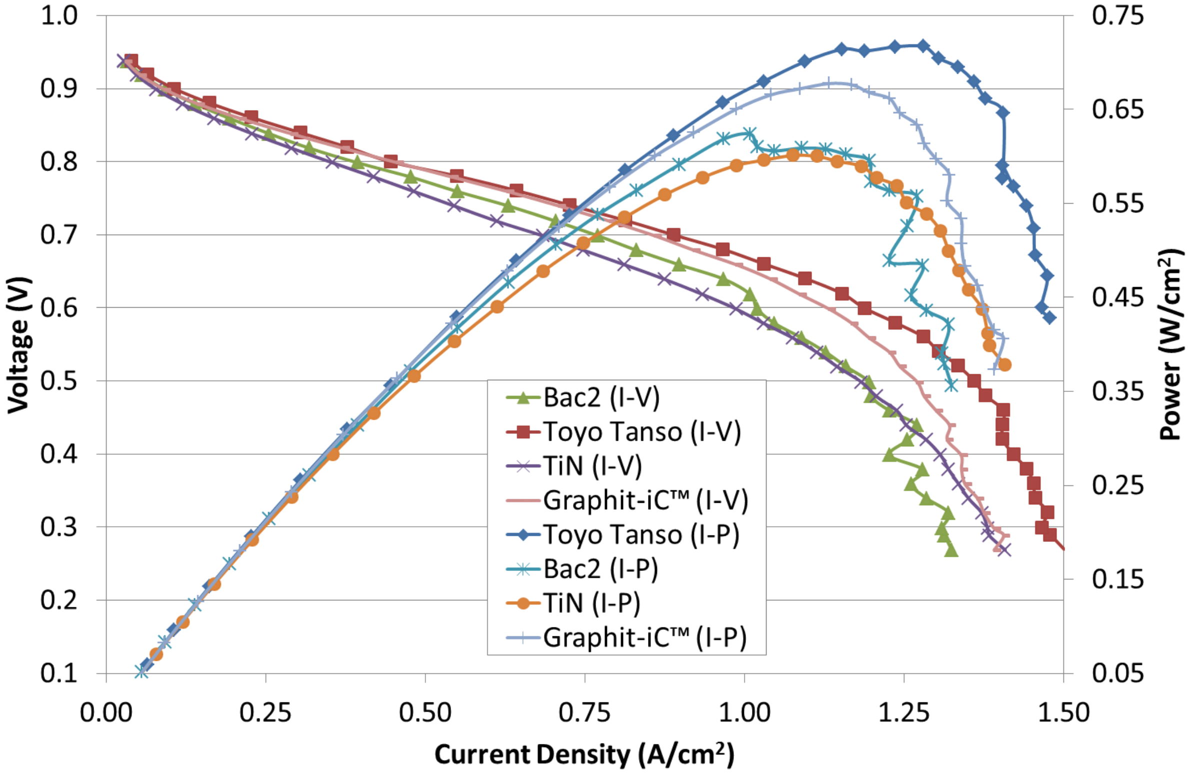

Figure 4.20 I-V curves for different bipolar plate materials. A Nafion 212 membrane and an ETEK GDE. Pt loading was 0.4 mg/cm^2. 70°C cell temperature. Relative humidity of anode and cathode gas streams was 30%. Flow rate of hydrogen and oxygen was 120 ml/min and 300 ml/min respectively

To link this in-situ data with the previous ex-situ ICR measurements it would be necessary to confirm the magnitude and uniformity of the pressure on the plate. In order to give a rough measurement of the actual *in-situ* compression between the GDL and bipolar plate, Pressurex™ paper (0.5-2.5 MPa) was used. Despite tightening the bolts in a star type sequence, Figure 4.21 shows non uniform compression of the MEA with the majority of the pressure located around the gasket area with the membrane between the two gaskets being clearly visible. Obviously, the selection of the MEA/gasket combination for optimal active area pressure is an area for future work. An air bladder may also be a more accurate method of measuring compression compared to bolt torque. Once a uniform pressure can be established, a more precise relationship between *ex-situ* ICR and *in-situ* performance should be able to be calculated (provided the GDL type is the same). However, the influence of operating conditions must also be considered as Oyarce et al. [207] have found that temperature, relative humidity of gases and current density may also alter the ICR.

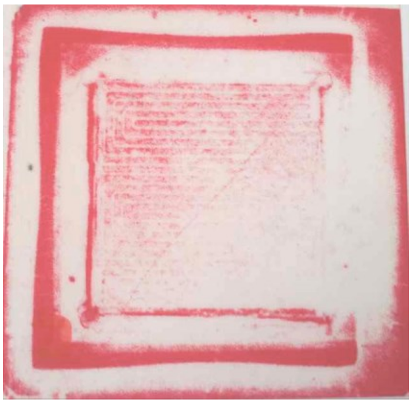

Figure 4.21 Photo of Pressurex™ paper after being compresed in the fuel cell between the GDL and bipolar plate using a bolt torque of 5 Ncm

4.4 Post corrosion testing

As will be explained further in Section 6.2, potentiostatic corrosion measurements were also carried out at 1 V/RHE for 24 h to simulate an extended time under fuel cell standby conditions. This potential was selected as it is more severe than the typical fuel cell operating potential of 0.6 V/RHE and it is plausible that the fuel cell maybe under these conditions for extended periods of time. After corrosion testing, the ICR was found to decrease in the same order as the as-received materials 316L > ZrN > TiN > CrN > Carbon based coatings > Au, although the ICR values for all materials were increased as shown in Figure 4.22. The relative increase in ICR was ranked in the order CrN < 316L < Carbon coatings < Au < ZrN < TiN.

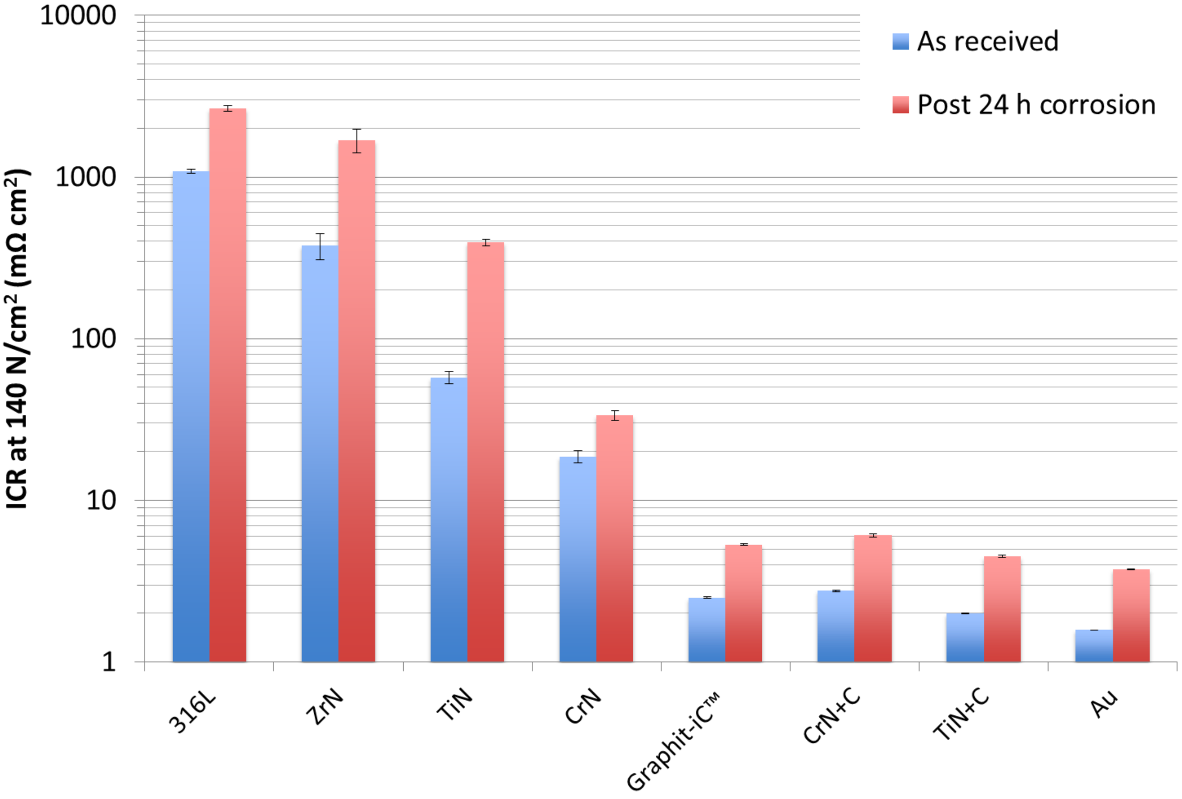

Figure 4.22 ICR of as-received and corroded PVD coatings (see Chapter 6 for conditions)

4.4.1 XPS of PVD coatings post corrosion testing

As shown in Figure 4.23, the nitride coatings all showed increased levels of oxygen at the surface post corrosion testing. Of these coatings, TiN had the greatest increase in surface oxygen which was consistent with the greatest increase in ICR seen previously.

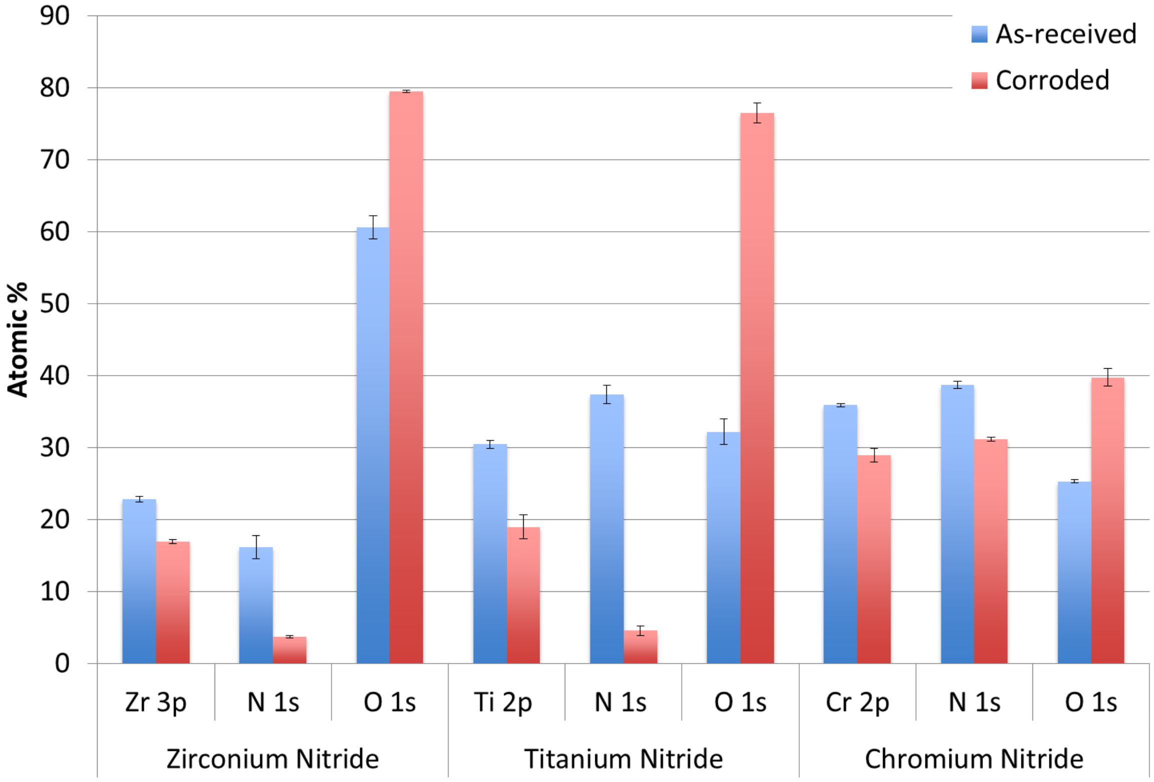

Figure 4.23 Elemental quantification from XPS survey of as-received ZrN, TiN and CrN coatings. Error bars show the standard deviation of three measurements (spot size of 400 µm each)

Compared to the nitride coatings, the carbon based coatings in Figure 4.24 showed much lower levels of surface oxygen, even after corrosion testing which was in keeping with their lower ICR values. In contrast to all other coatings, the Au coating showed a significantly larger standard deviation from three measurements. This was attributed to its very low thickness (20 nm) which may have resulted in an increased surface heterogeneity. Somewhat unexpectedly there was also a decrease in surface oxygen, which would suggest the need for more intrasample tests.

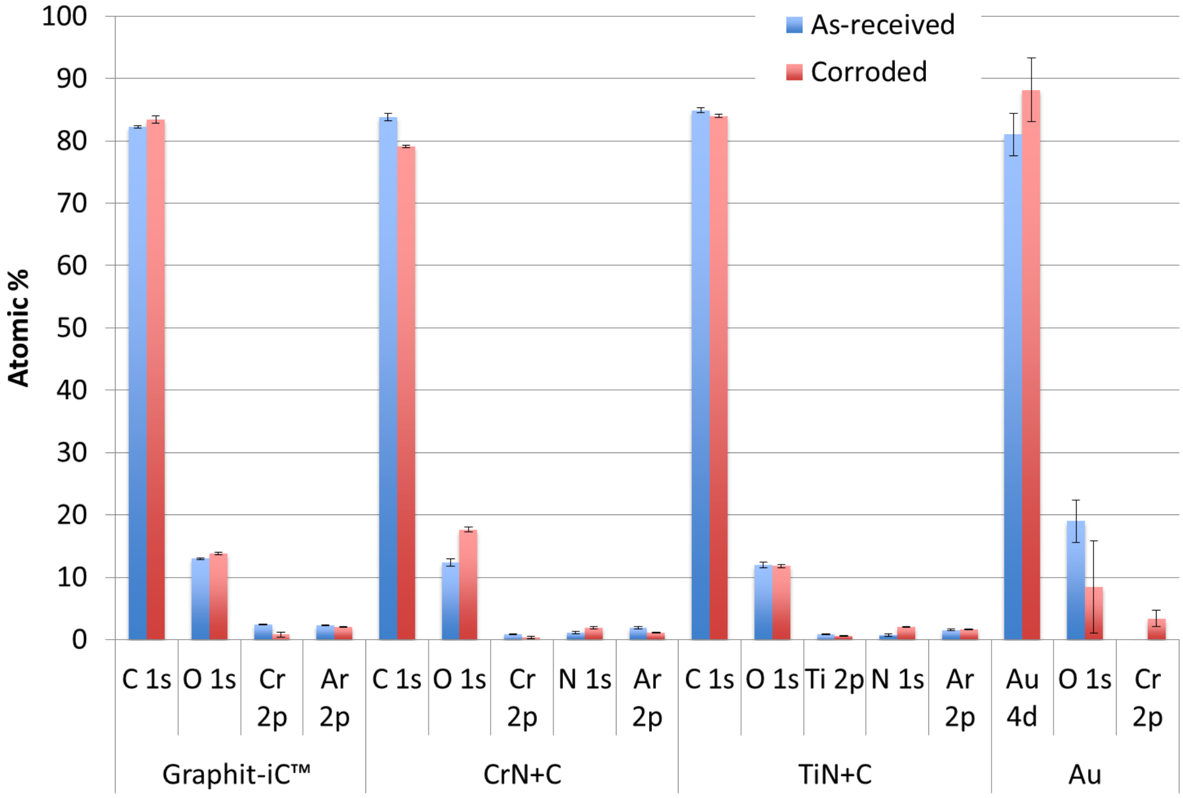

Figure 4.24 Elemental quantification from XPS survey of as-received and corroded Graphit-iC™, CrN+C, TiN+C and Au coatings. Error bars show the standard deviation of three measurements (spot size of 400 µm each)

In terms of futher work, whilst the identification of the particular metal oxide states would be of some benefit, it would be much more preferable to carry out more extensive XPS on actual bipolar plates after in-situ testing to ensure that the ex-situ test conditions are valid.

4.5 Summary

This chapter has examined many of the factors affecting the interfacial contact resistance (ICR) of PVD coatings. As observed in the literature, the substrate surface roughness was found to influence the ICR, particularly when the surface was very smooth. However, it was also found that the addition of a conductive Graphit-iC™ coating to the said surfaces negated any previously observed effect. Chemical etching was also found to have an effect on the measured ICR of the substrate, with greater etching times being associated with a lower ICR. This was presumably due to the modification of the passive oxide film although further surface analysis was not carried out in this work. Similarly to the influence of surface roughness on ICR, the addition of a conductive Graphit-iC™ coating to the etched surfaces negated any previously observed effect. It was presumed that any chemical modification of the surface caused by chemical etching was made redundant by the oxide removing ion cleaning process prior to coating deposition.

PVD coating type was found to have a significant effect, with the ICR of 1 μm PVD coatings decreasing over orders of magnitude in the following order; ZrN > TiN > CrN > Carbon based coatings > Au. The variation of coating thicknesses from 0.1 – 1.1 μm resulted in no significant effect on the ICR for the Graphit-iC™ coating. The addition of a thin layer (0.1 – 0.2 μm) of amorphous carbon to the surface of TiN and CrN coatings resulted in a striking reduction in the ICR to a comparable level to that of Graphit-iC™. This suggested that the primary resistance of the metal nitride coatings was located at the GDL/coating interface, rather than the coating/substrate interface. Further examination of the nitride coatings by XPS confirmed the existence of metal oxide, the percentage of which could be linked directly to the ICR. The addition of oxygen to a carbon coating via oxygen plasma treatment was also found to have a detrimental effect on the ICR of carbon coatings with changes to the surface morphology and chemistry. After cathodic potentiostatic tests for 24 h at 1 V/RHE the ICR was found to increase across all of the coating types, the extent of which was correlated with the increase in surface oxygen as determined by XPS. The short term in-situ test results were qualitatively in accordance with the ex-situ ICR results, with a lower ICR resulting in increased fuel cell performance.

CHAPTER 5

STAMPED PVD COATINGS

5 STAMPED PVD COATINGS

As mentioned in Section 2.5.4, three methods of producing metallic bipolar plates are stamping, hydroforming and etching. Stamping is one of the most favoured methods for producing metal bipolar plates for the automotive industry due to its very short process time and large unit volume capability. For automotive applications, typically two foils are formed and welded together. This process also produces an internal cavity that can then be used as a conduit for water cooling. Stamping of bipolar plates can either be done in a single stage or by a progressive process with consecutive dies to elongate the material prior to producing the final form. This chapter examines the feasibility of using pre-coated material for subsequent stamping. Consequently, in collaboration with Brandauer Ltd., the surface of pre-coated stamped foils was examined to investigate the effect of stamping. AISI 316L 0.1 mm foil with TiN, Graphit-iC™ and TiN+C multilayer coatings ranging from 0.1 to ~1.5 µm in thickness were stamped according to the same confidential stamping procedure. No physical cleaning of the surface was carried after stamping to avoid exacerbating any damage to the coating after stamping. SEM was used to observe the rib areas of the samples as this was anticipated to be the area of greatest strain. Several ribs were studied, as shown in Figure 5.1, to see if there were any localised changes across the sample, rib 1 being the outermost.

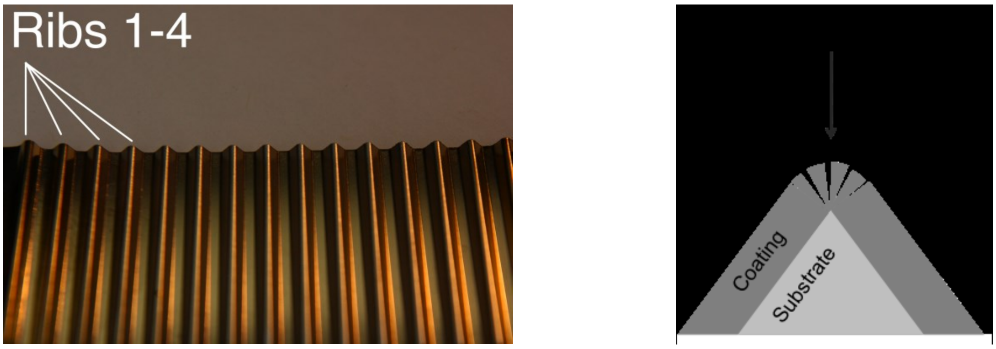

Figure 5.1 TiN coated AISI 316L foil after stamping (left) and area for SEM observation diagram (right)

5.1 As-received AISI 316L

As can be seen from Figure 5.2, vertical striations orthogonal to the horizontal strain from the stamping were observed for the as-received substrate due to the stretching of the material. Some horizontal striations were also observed which were attributed to existing features left over from the rolling process used to form the 0.1 mm foil. There was no apparent change in the surface morphology across the rib numbers.

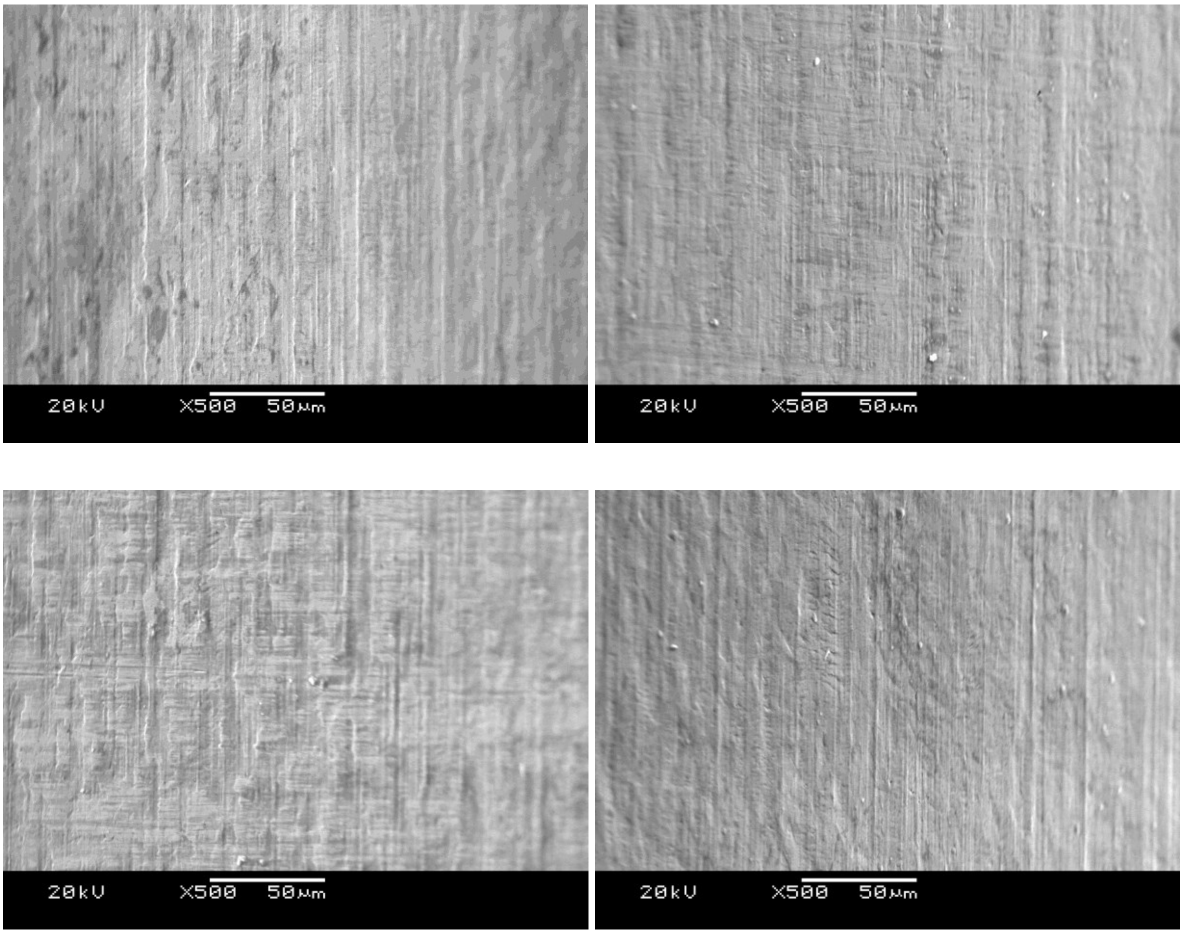

Figure 5.2 SEM images of as-received stamped 316L foil - rib 1 (top left), rib 2 (top right), rib 3 (bottom left) and rib 4 (bottom right)

5.2 PVD Coatings

5.2.1 Titanium Nitride

Figure 5.3 shows that the rib number of the stamped 1.5 μm TiN coated foil had a large impact on the coating integrity with the outer ribs of the sample (1 and 2) showing a great deal less cracking than those closer to the middle of the foil (3 and 4). There was no further deterioration of the ribs after this point. It was proposed that the outer edges of the foil are drawn inwards during the stamping action resulting a locally reduced strain at the outside edge ribs in comparison to ribs formed closer to the middle of the sample.

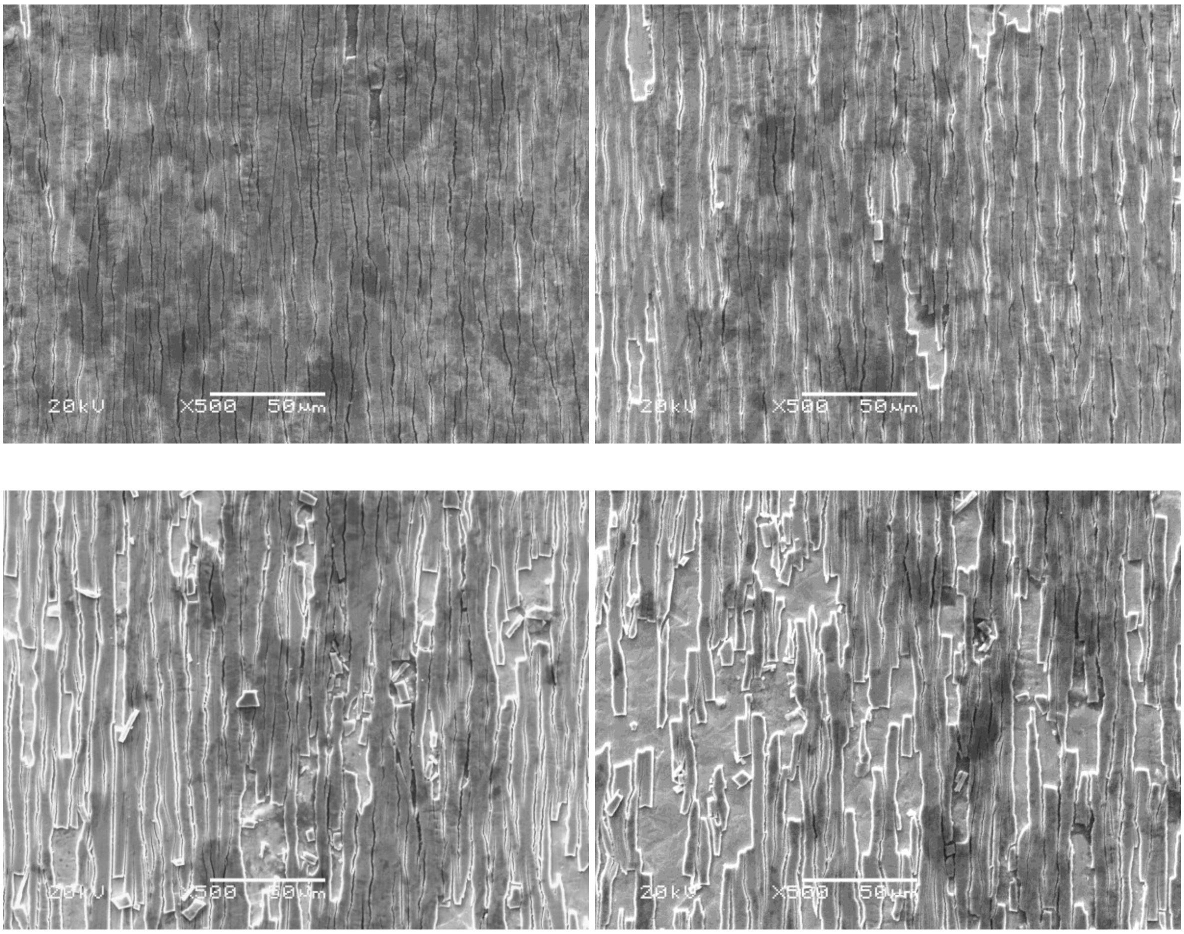

Figure 5.3 SEM images of stamped 1.5 μm TiN coated 316L foil - rib 1 (top left), rib 2 (top right), rib 3 (bottom left) and rib 4 (bottom right)

Figure 5.4 showed that the 0.1 μm TiN coating had less cracking than the thicker 1.5 μm TiN coating (Figure 5.3), although rib number was still found to have a noticable effect. The dark spots on the surface of the sample were attributed to residual lubricant (Aquadraw 4000) from the stamping process.

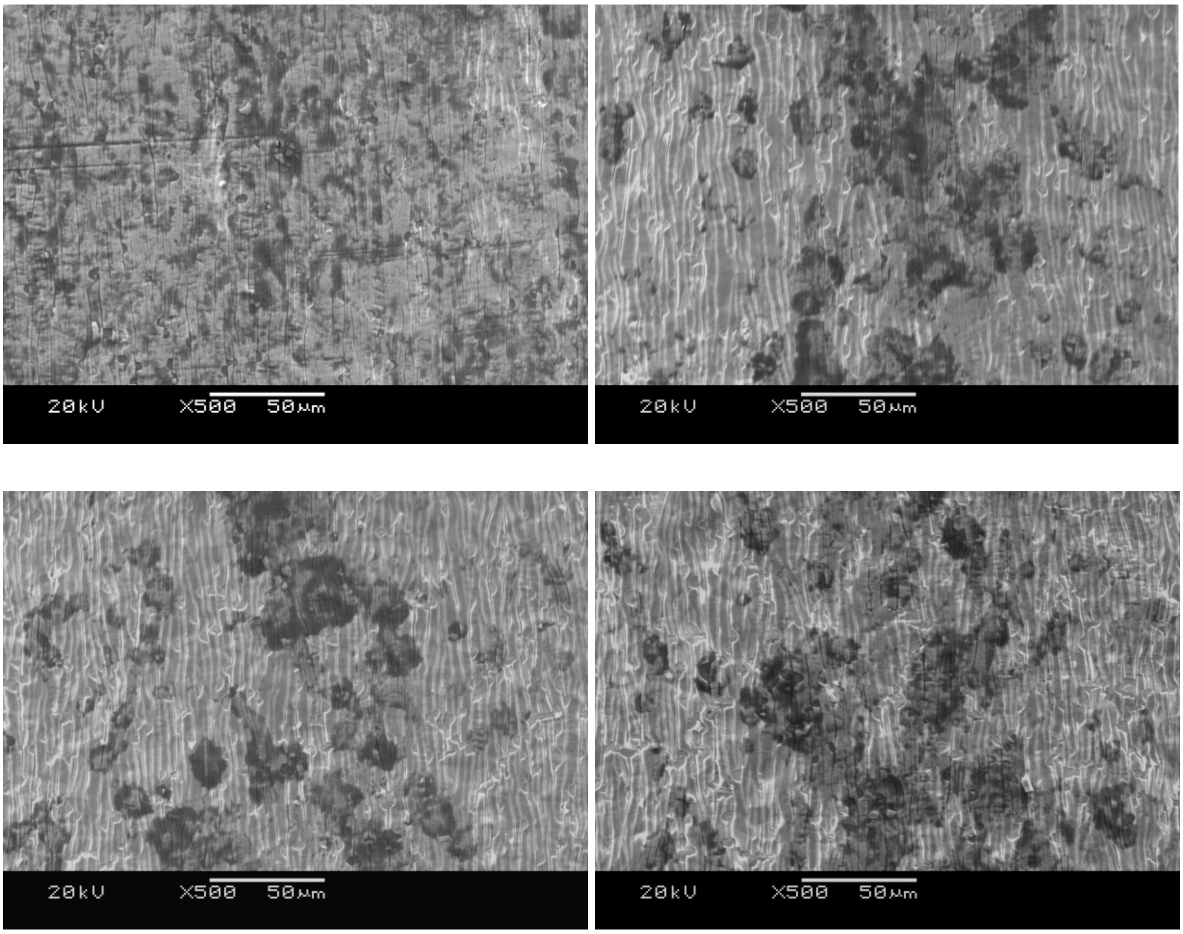

Figure 5.4 SEM images of stamped 0.1 μm TiN coated 316L foil - rib 1 (top left), rib 2 (top right), rib 3 (bottom left) and rib 4 (bottom right)

5.2.2 Graphit-iC™

There was significantly less cracking and flaking of the 1.1 µm Graphit-iC™ coating shown in Figure 5.5 compared to the 1.5 µm TiN coating shown in Figure 5.6. This was attributed to the lower hardness (14-17 GPa) and friction coefficient (<0.1) of the carbon based coating compared to TiN (20-22 GPa and 0.6-0.7 respectively). This coating is also commonly used as a dry lubricant coating. A similar stamping effect was seen (although to a lesser degree) where the outer ribs of the stamped foil (1 and 2) showed less cracking than the inner ribs (3 and 4). The dark spots on the surface of the sample were attributed to residual lubricant from the stamping process. This may also have exacerbated surface charging effects resulting in the observation of bright lines eitherside of some cracks.

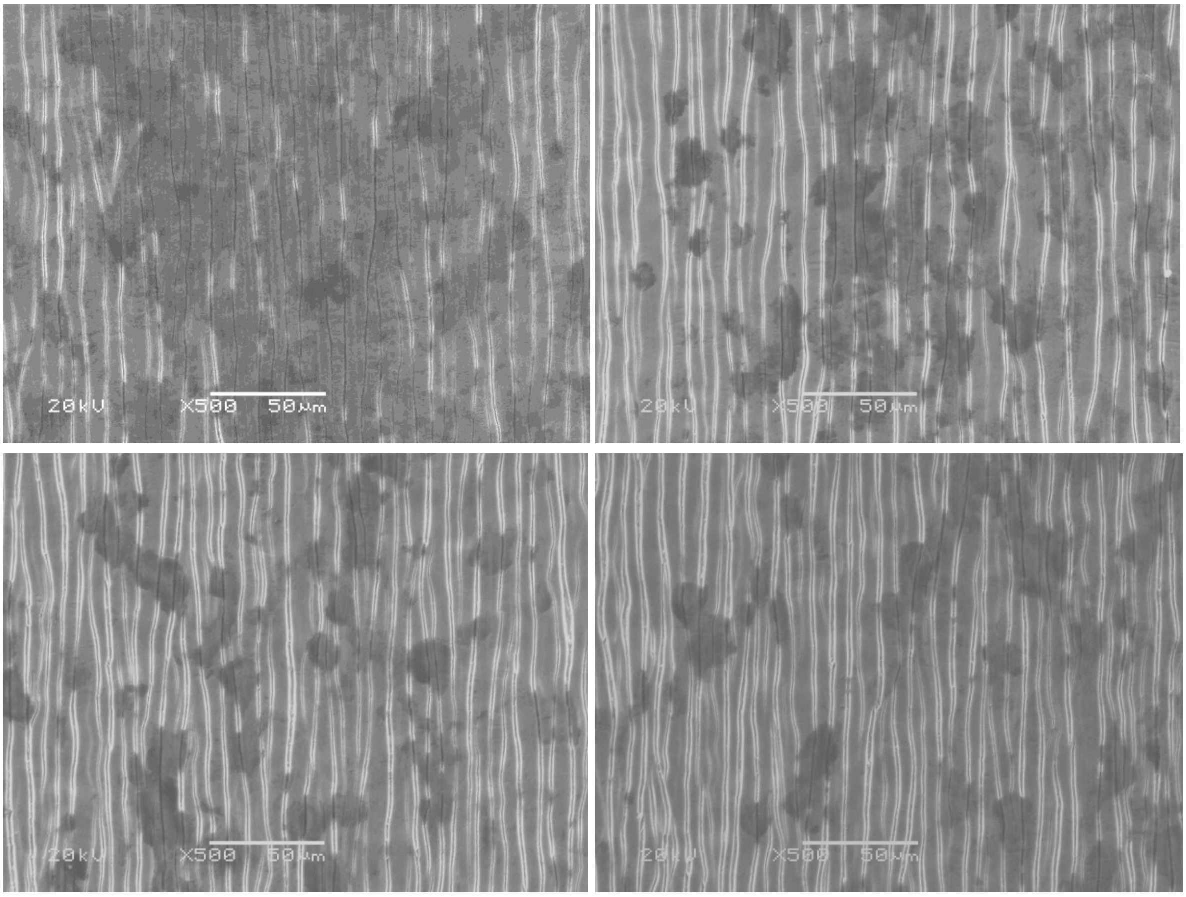

Figure 5.5 SEM images of stamped 1.1 µm Graphit-iC™ coated 316L foil - rib 1 (top left), rib 2 (top right), rib 3 (bottom left) and rib 4 (bottom right)

Similarly to TiN, the 0.1 μm Graphit-iC™ coating appeared to show less cracking than the thicker 1.1 μm coating; however, there also appeared to be less sensitivity to rib number. Horizontal striations shown in Figure 5.6 from the rolled 316L foil were also more visible than those samples with thicker coatings, but this was attributed to local variations in substrate condition. It was difficult to establish whether the perceived smaller cracks on the thinner coatings were indeed smaller at the substrate interface or if actually the crack width at the surface of the coating was just proportional to coating thickness.

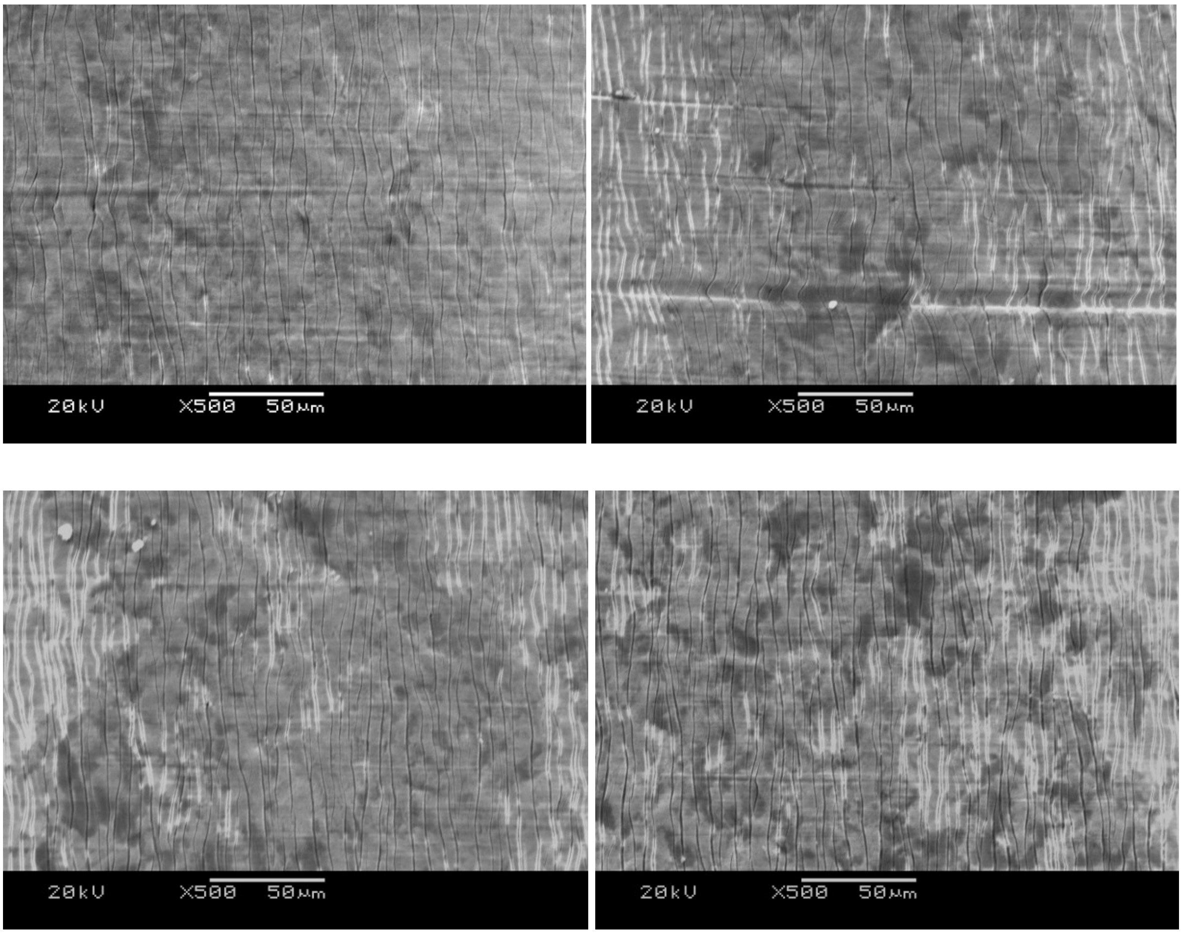

Figure 5.6 SEM images of stamped 0.1 μm Graphit-iC™ coated 316L foil - rib 1 (top left), rib 2 (top right), rib 3 (bottom left) and rib 4 (bottom right)

5.2.3 Multilayer Coatings

Figure 5.7 shows that the addition of a thin 0.2 μm carbon topcoat to a 0.3 μm TiN coating resulted in the coating appearing to behave similarly to a single layer Graphit-iC™ coating. Exactly how the TiN underlayer was modified after stamping was not clear using this method, although the coating in general showed no signs of flaking or poor adhesion. This shows that in addition to improving the ICR of metal nitride coatings, the carbon topcoat also gives significant benefits to the mechanical properties required for stamping pre coated material. Similarly to the other tested coatings, regardless of coating type or thickness, rib position (suspected elongation) was again a large factor in the degree of cracking observed.

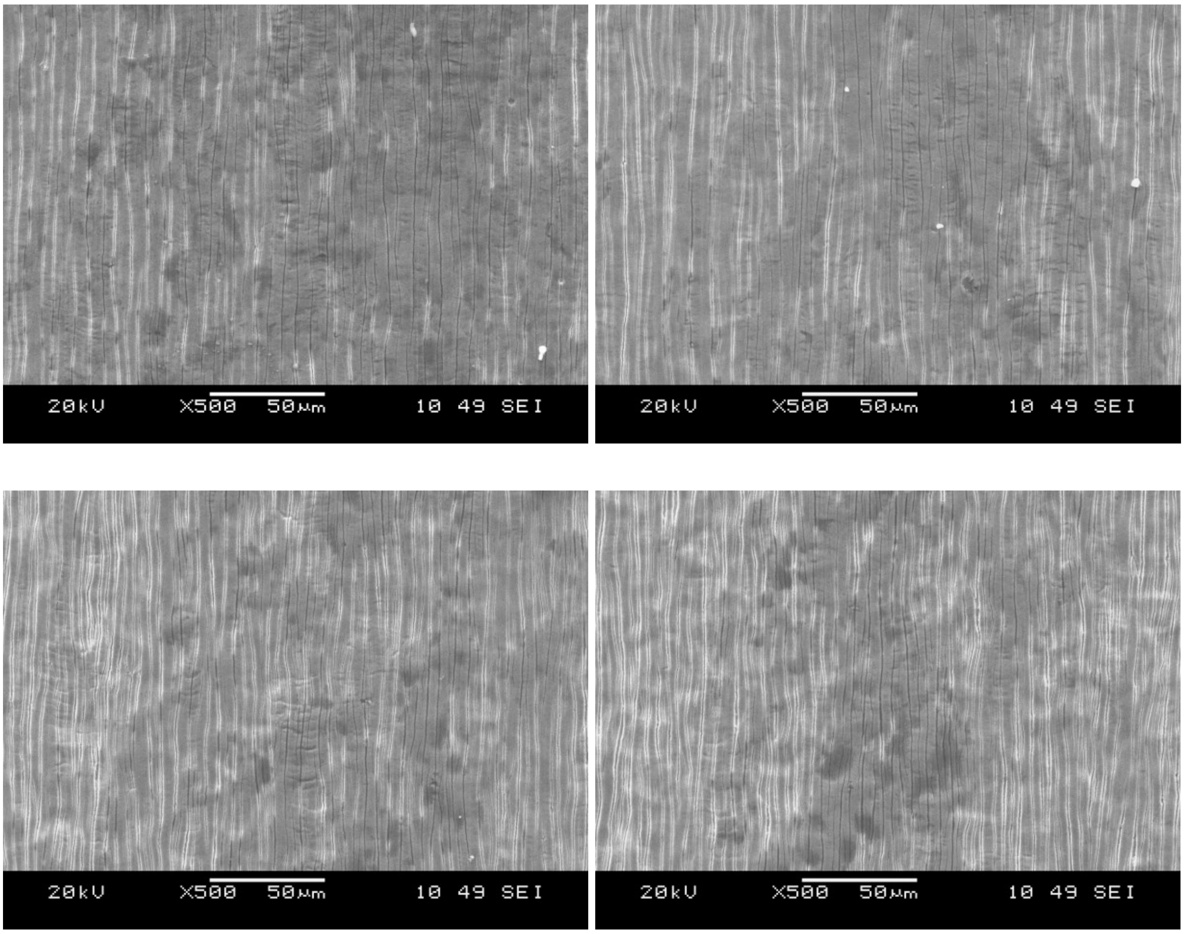

Figure 5.7 SEM images of stamped TiN+C coated 316L foil - rib 1 (top left), rib 2 (top right), rib 3 (bottom left) and rib 4 (bottom right)

5.3 Feasibility of PVD coatings for serial production

The exact manufacturing process route for the serial production of coated bipolar plates is currently unclear. Two manufacturing possibilities involve using pre-coated metal strip or post coating of the complete bipolar plate assembly as shown below in Figure 5.8.

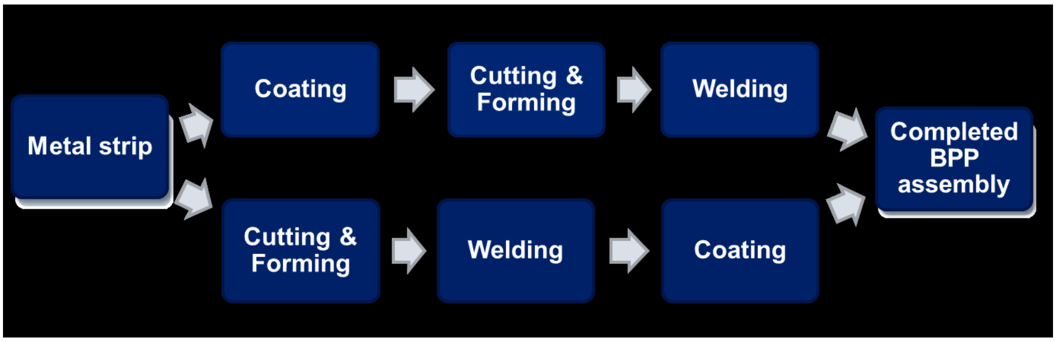

Figure 5.8 Example of possible pre-coating (top) and post-coating (bottom) process routes

Pre-coated material is preferred by tier one suppliers and automotive OEMs due to anticipated cost reductions from reduced handling complexity. It is already used extensively in other industries e.g. the metallisation of polymer film for packaging. Existing suppliers specifically providing pre-coated PVD strip for bipolar plates include Sandvik and Impact Coatings. However there are some potential technical concerns with this route. As shown in the previous section, the pre-coated material is highly likely to be damaged by the stamping process. Other down stream processes which may also cause concern for pre-coated material are the exposure of the substrate from cutting out plate perimeter and inlet/outlet holes and welding processes which may be problematic if needed in the active area. In light of the potential process compatibility issues, it is unclear if the coating after processing will provide sufficient corrosion protection. Metal ions released from the stainless steel substrate (particularly Fe) will reduce the protonic conductivity of the membrane and may accelerate the chemical degradation of the membrane via Fenton type reactions, which, in tern may accelerate the corrosion of the bipolar plate.

Coatings deposited after the manufacture of BPP assemblies are less likely to suffer from the same process compatibility issues as the coating is carried out after these process steps. Although likely to be a more expensive process, serial PVD post coating of large discrete parts is already commonly carried out in industry manufacturing architectural and automotive glass, electronics (flat panel displays, semi conductors, data storage) and large reflective surfaces. Using this process route, multiple bipolar plate assemblies could conceivably be placed into large frames for subsequent PVD coating.

5.4 Summary

Although the exact process for manufacturing automotive bipolar plates is yet to be fixed, there is an existing DoE requirement for 40% elongation of the bipolar plate. This clearly shows that the physical and tribological properties of the coating are an important factor. In this chapter the suitability of the coating for post stamping was found to be influenced by several factors. In terms of coating type, the Graphit-iC™ coating, which is widely known to be softer and with a lower coefficient of friction, was found to be more suitable than the TiN coating. Rib position was also found to be a major factor in the degree of cracking experienced. This was attributed to a locally reduced strain at the outside edge ribs, due to the edges of the foil being drawn inwards during the stamping action. This could be a significant issue for automotive plates as they are significantly larger than the samples tested in this work and hence there could be an even larger strain gradient. Coating thickness was found to play a lesser role seeming to have a larger effect with the harder TiN coating compared with the Graphit-iC™. The addition of a thin carbon topcoat to the TiN coating noticeably improved the stamping behaviour compared to TiN only coatings, however it was not clear whether the cracks were present in both coating layers or just the carbon topcoat.

Further Work

From this prelimenary work there are several interesting avenues for futher exploration including;

- A closer examination of the crack sites to confirm the effect of thickness on crack width and a systematic study of the effects of elongation.
- The identification of a suitable quantitative measure such as toughness to compare resistance to cracking.
- Corrosion testing of the coated stamped plates to discover the impact of cracking with regard to the protective ability of the PVD coatings. This could also be followed by a comparison with formed post coated material.
- A comparison with other manufacturing methods. In particular, hydroforming may minimise localised regions of elevated stress across the foil due to more uniform forces from the hydrostatic pressure used to form the flow field.

CHAPTER 6
CORROSION

Includes extracts published in H. Sun, K. Cooke, G. Eitzinger, P. Hamilton & B. Pollet. *Development of PVD coatings for PEMFC metallic bipolar plates.* Thin Solid Films, 2012, 528, 199-204. Reprinted by permission.

6 CORROSION RESISTANCE

Although the corrosion of the bipolar plate in a fuel cell is a highly complex process with many variables, as previously described in Section 2.5.3, in this chapter the measurement of corrosion was simplified to an accelerated corrosion method commonly used in the literature, placing the sample in an electrolyte solution of 0.5 M H_2SO_4 at 70 °C [117, 128]. Both potentiodynamic and potentiostatic measurements were carried out to investigate the behaviour of as-received 316L, ZrN, TiN, CrN, Graphit-iC™, CrN+C, TiN+C and Au coatings. The results were compared with studies in the literature, which gave the best fit, in terms of coating material, substrate and experimental conditions. The anodic current densities from the polarisation curves of coated materials were also measured used to compare coating performance at the potentials expected during fuel cell operation, stand-by and start up/shut down.

6.1 Potentiodynamic Measurements

6.1.1 *AISI 316L Stainless Steel*

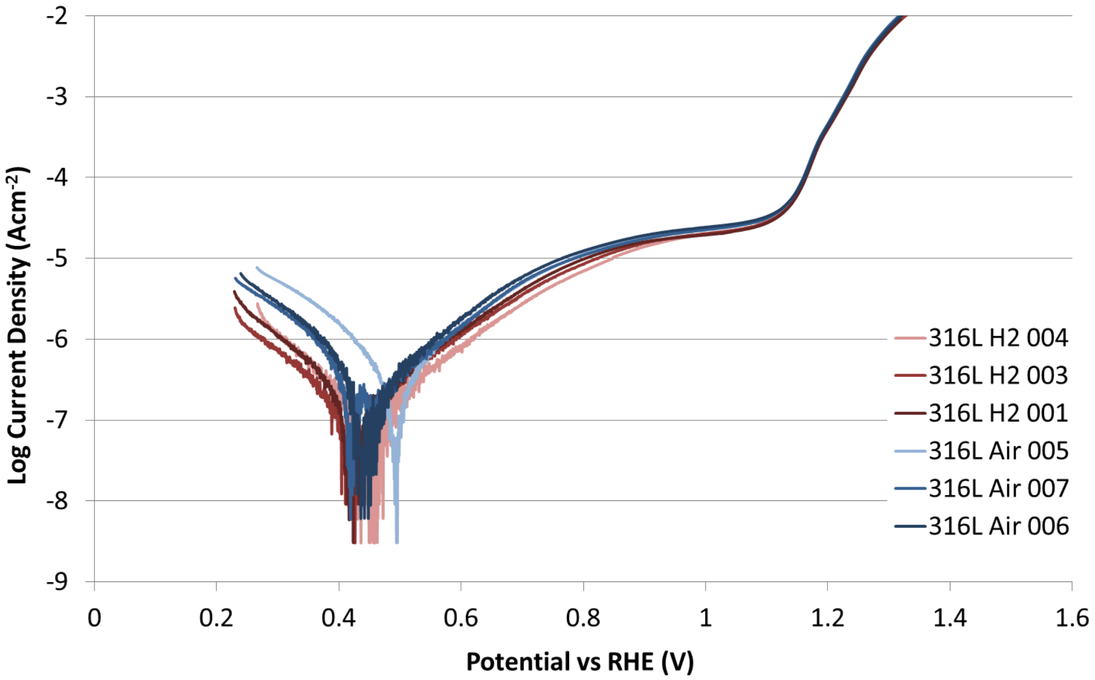

Figure 6.1 Potentiodynamic measurements of as-received 316L 100 µm foil at 1 mV/s in 70 °C 0.5 M H_2SO_4 bubbled with air or hydrogen

As-received AISI 316L 100 µm foil was used without polishing in order to match the likely condition of the material when used as a bipolar plate. Possibly as a result of this, there were some sample to sample variations in the polarisation curves shown in Figure 6.1, which were attributed to local changes in surface chemistry and roughness. Several aspects of the polarisation curves were found to be unusual when compared to the established literature regarding stainless steel corrosion. Specifically, the E_{corr} at ~0.45 V/RHE was significantly higher than similar studies, as shown in Table 6.1. These studies also showed the presence of a typical active peak followed by a passivation region, which was also not observed in this work. Only in one other fuel cell related study by Lavigne et al. [209], was a similar behaviour observed for 100 µm 316L foil where the E_{corr} was also significantly higher (0.4 V/RHE) and the polarisation curve failed to show an active peak and passivation region. However, in this study no comment on the lack of these features was given. Given the good fit between the studies in the literature regardless of material form (plate or foil) and preparation (as receieved or polished); the results from the literature, and not those obtained in this work, were used for comparisons in later sections. There were some similarilties between these results and the literature; the current density, which at 0.8 V/RHE was around 10 µAcm^{-2} [208] and the shift in E_{corr}, becoming more positive in the aerated environment than the hydrogen bubbled environment. This was attributed to the higher half-cell potential of $O_2 + 4\ H^+ + 4\ e^- \leftrightarrow 2\ H_2O$ compared to that of $2\ H^+ + 2\ e^- \leftrightarrow H_2$ [179].

Table 6.1 Potentiodynamic polarisation parameters of 316L from the literature

Substrate	Experimental Conditions	E_{corr} (standardised to V/RHE)	I_{corr} (µAcm^{-2})	Reference
4, mm thick 316L (Trinity Brand Industries Inc.)	0.5 M H_2SO_4 solution with 2 ppm HF at 80 °C	– 0.045 (Air) – 0.066 (H_2)	-	Feng et al. [179]
Polished 316L	0.5 M H_2SO_4 solution at 70 °C	0.043 (O_2) – 0.014 (H_2)	2.43 (O_2) 9.15 (H_2)	Wang & Northwood [128]
0.5 mm thick 316 (Goodfellow, UK)	1 M H_2SO_4 and 2 ppm F^- ions at 70 °C	– 0.09 (Air) – 0.1 (H_2)	-	Gabreab et al. [208]
316 (as-received condition without any grinding or polishing)	0.005 M H_2SO_4 (pH 2) solution at 80 °C	– 0.106 (Air)	4.5 (Air)	Yoon et al. [158]

At higher potentials, in the region of 1.1 V/RHE, there was a rapid increase in current density (as also observed in the literature) which was attributed to the formation of soluble chromate ions at the surface via a reaction such as $2\ Cr + 7\ H_2O \rightarrow Cr_2O_7^{2-} + 14\ H^+ + 12\ e^-$. It was unlikely that this increase was due pitting corrosion as there was little evidence of this when examined by SEM as shown in Figure 6.2. Instead, the surface of the AISI 316L steel was found to become slightly cloudier after the testing and there was evidence of a small amount of dissolution from the grain boundaries. This has been suggested to occur due to the oxides at the grain boundary being less ordered and more easily dissolved than the regions within the grains [208].

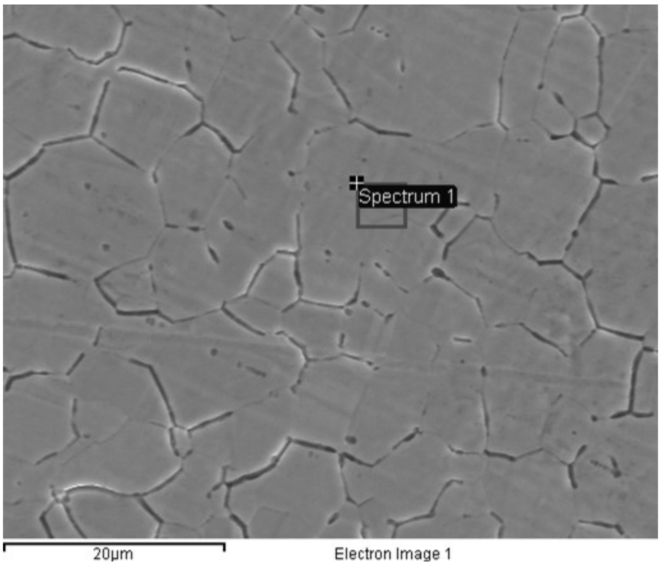

Figure 6.2 SEM image of AISI 316L stainless steel after potentiodynamic test showing no pitting corrosion

6.1.2 Titanium Nitride

There was very little difference in the polarisation behaviour of the 0.4 and 1 µm thick TiN coatings as shown in Figure 6.3 and Figure 6.4. This was attributed to two factors; first, the thickness of both coatings being greater than the surface roughness of the substrate (as previously measured in Section 4.1.1), and secondly, the coating thickness apparently having no discernable effect on the coating defect density.

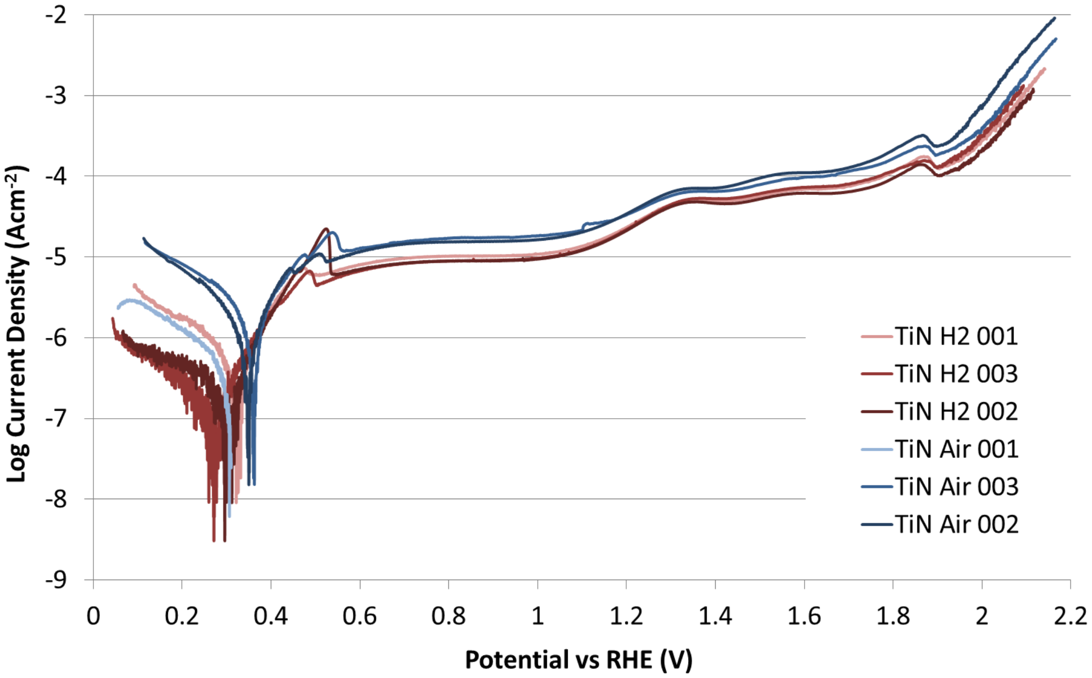

Figure 6.3 Potentiodynamic measurements of 0.4 µm TiN coated 100 µm 316L foil at 1 mV/s in 70 °C 0.5 M H_2SO_4 bubbled with air or hydrogen

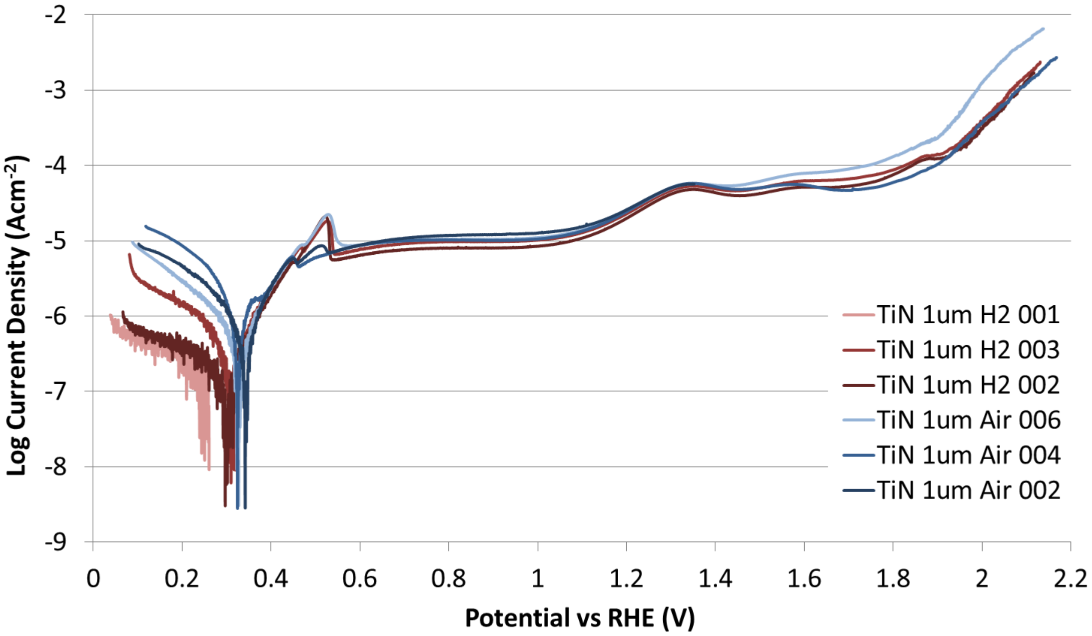

Figure 6.4 Potentiodynamic measurements of 1 µm TiN coated 100 µm 316L foil at 1 mV/s in 70 °C 0.5 M H_2SO_4 bubbled with air or hydrogen

The E_{corr} of both TiN coating thicknesses was more noble (~ 0.35 V/RHE under aerated conditions) than the AISI 316L results found in the literature (0 to -0.1 V/RHE). It was also more noble than the results found in the literature (Table 6.2), which was attributed to different deposition methods and experimental conditions having a large effect on the coating performance. The critical passivation potential (E_{pp}) was in the region of 0.5 V/RHE and the critical passivation current (I_{crit}) was only marginally higher than the initial passive current (I_p) of ~10 μAcm^{-2}, suggesting the coating was easily passivated. However, the current density at an operational potential on the fuel cell cathode side (0.8 V/RHE) was above the US DoE target of 1 μAcm^{-2}. As the E_{corr} was significantly more positive than the potential range expected at a fuel cell anode (<0.1 V/RHE), very little corrosion is likely to occur as the sample should be cathodically protected (this was also the same for most other coatings). The change in colour from golden to blue/brown (shown in Figure 6.5) after the corrosion tests suggested the formation of a TiO_x layer during the potentiodynamic measurement (which was also confirmed by XPS data shown earlier in Figure 4.23). It is this TiO_x layer that was proposed to protect the AISI 316L substrate at higher potentials beyond 1.2 V/RHE. This may be of some benefit at the fuel cell cathode if the load cycle involves many startup/shut downs with their associated high potentials.

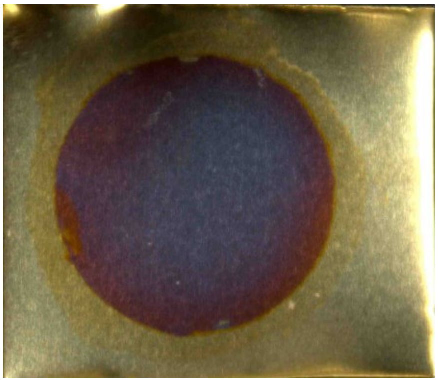

Figure 6.5 Photo of 1 µm TiN coated 100 µm 316L foil after potentiostatic test

Table 6.2 Potentiodynamic polarisation parameters of TiN coated 316L from the literature

Substrate & Coating details	Experimental Conditions	E_{corr} (standardised to V/RHE)	I_{corr} (μAcm^{-2})	Reference
Mirror polished 316L with 2 µm TiN deposited by EBPVD	1 M H_2SO_4 solution at 70 °C	– 0.14 (O_2) – 0.1 (H_2)	31.5 (O_2) 4.07 (H_2)	Wang et al. [152]
Polished 316L with 15 µm TiN coating deposited by evaporative PVD	0.5 M H_2SO_4 solution at 70 °C	-	1.02	Wang & Northwood [117]
Polished 316L with 1 µm PVD TiN. Deposition bias – 50V	1 M H_2SO_4 + 2 ppm HF solution at 70 °C	0.11 (Air)	128.7 (Air)	Nam et al. [200]
Polished 316L with 1 µm PVD TiN. Deposition bias – 100V	1 M H_2SO_4 + 2 ppm HF solution at 70 °C	0.22 (Air)	18.8 (Air)	Nam et al. [200]
Polished 316L with 1 µm PVD TiN. Deposition bias – 150V	1 M H_2SO_4 + 2 ppm HF solution at 70 °C	0.23 (Air)	6.43 (Air)	Nam et al. [200]
3 µm TiN deposited on 316L by multi-arc ion plating	0.05 M H_2SO_4 + 2 ppm F^- solution at 70 °C	~ – 0.1 (Air)	~1	Tian & Sun [201]

6.1.3 Zirconium Nitride

The E_{corr} of the ZrN coating was the least noble of all the examined PVD coating materials at ~ -0.05 V/RHE under aerated conditions. This was similar to the limited results for ZrN found in the literature as shown in Table 6.3. The current density at 0.8 V/RHE was around 10 μAcm^{-2}, which was also above the US DoE target. This was also similar to Yoon et al. [158] who found the current density to be ~4 μAcm^{-2} at 0.841 V/RHE. At high potentials, similarly to the TiN coatings, relatively low current densities and a change in colour after the corrosion tests were both observed. This again suggested the formation of a more stable oxide layer during the potentiodynamic measurement (as also shown by the XPS results in Figure 4.23). Uniquely, the ZrN coating was the only coating examined where the corrosion potential was more noble in the H_2 rather than the aerated environment suggesting further analysis needs to be undertaken.

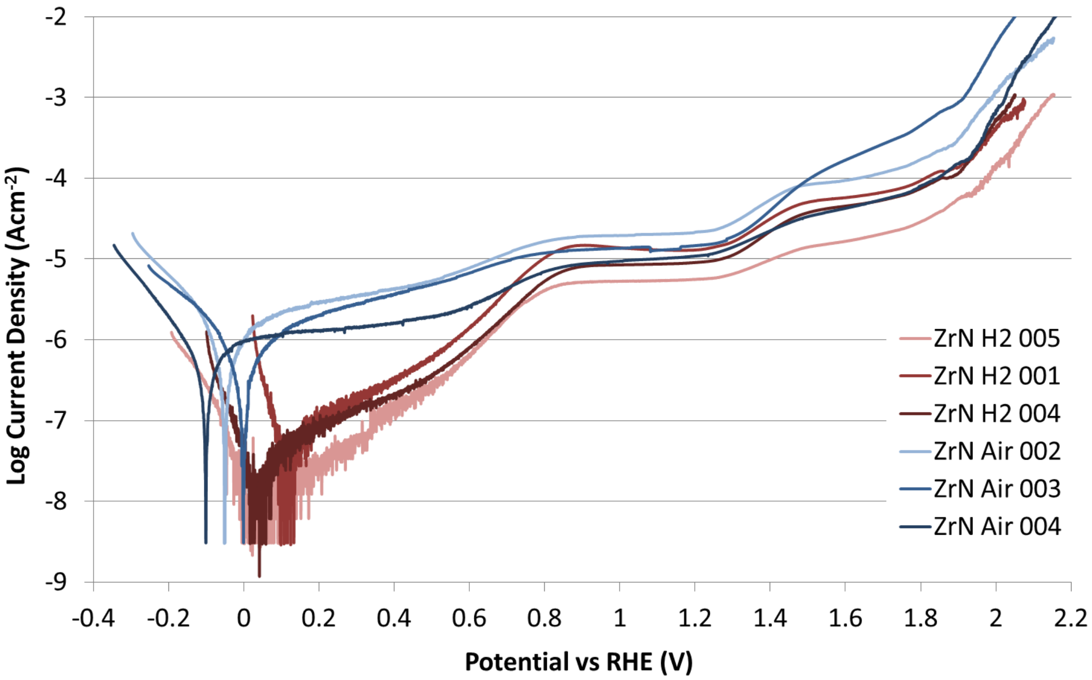

Figure 6.6 Potentiodynamic measurements of 1 µm ZrN coated 100 µm 316L foil at 1 mV/s in 70 °C 0.5 M H_2SO_4 bubbled with air or hydrogen

Table 6.3 Potentiodynamic polarisation parameters of ZrN coated 316L from the literature

Substrate	**Experimental Conditions**	**E_{corr} (standardised to V/RHE)**	**I_{corr} (µAcm^{-2})**	**Reference**
As-received 316L with ZrN deposited by magnetron sputtering or cathodic arc evaporation (Tanury Industries Inc.)	0.005 M H_2SO_4 (pH 2) solution at 80 °C	– 0.01 (Air)	0.07	Yoon et al. [158]
316L with 1.5µm ZrN deposited by cathodic arc evaporation	0.5 M H_2SO_4 solution at 70 °C	– 0.186 (Air)	376	Menghani et al. [210]

6.1.4 Chromium Nitride

The E_{corr} of CrN was was obscured by possible electrical interference in the order of 10 nA/cm^2. The current density at 0.8 V/RHE was below 0.1 μAcm^{-2}, meeting the US DoE target for the potential at the fuel cell cathode. A similar interference was also seen by Zhang et al. [174] who investigated a CrN/Cr multilayer coating on AISI 316L. Due to these very low current densities it was also unclear whether there was an active peak and passive region as with some other metal coatings. Similarly to the AISI 316L, there was also a rapid increase in current density at 1.1 – 1.2 V/RHE which was again attributed to the formation of soluble chromate ions from the CrN coating.

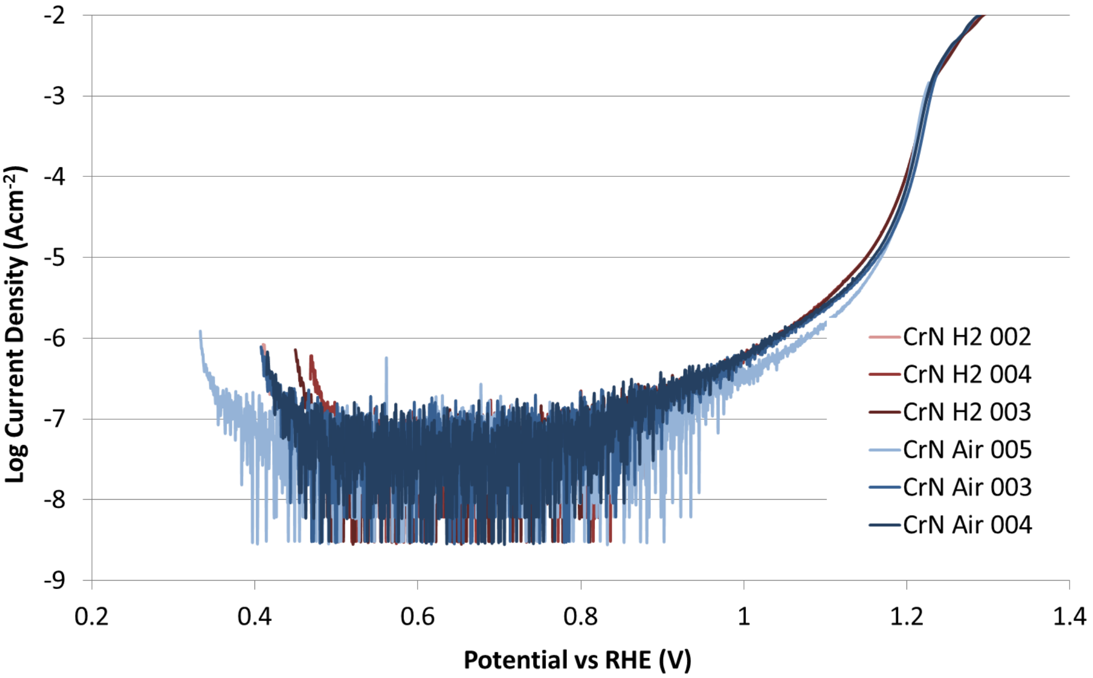

Figure 6.7 Potentiodynamic measurements of 1 μm CrN coated 100 μm 316L foil at 1 mV/s in 70 °C 0.5 M H_2SO_4 bubbled with air or hydrogen

As shown in Table 6.4, there were no studies that used exactly the same CrN deposition method with the same experimental conditions. Despite this, CrN was found to show a significant improvement in the corrosion resistance in all other studies.

Table 6.4 Potentiodynamic polarisation parameters of CrN coated 316L from the literature

Substrate & Coating	**Experimental Conditions**	**E_{corr} (standardised to V/RHE)**	**I_{corr} (μAcm^{-2})**	**Reference**
Mirror polished 316L with 2 μm CrN deposited by EBPVD	1 M H_2SO_4 solution at 70 °C	(O_2) (H_2)	1.31 (O_2) 1.41 (H_2)	Wang et al. [152]
As-received 0.1 mm 316L with 100 nm CrN deposited by PVD	0.07 M of Na_2SO_4 to limit ohmic drop with the addition of a small amount of H_2SO_4 (to reach pH 4) at room temperature	0.35 (Air)	<1 (Air)	Lavigne et al. [209]
CrN/Crmultilayer PBAIP	1 M H_2SO_4 + 5ppm F^- solution at 70 °C	0.24 (Air)	0.1 (Air)	Zhang et al. [174]

6.1.5 Graphit-iC™

Figure 6.8 shows the E_{corr} of the Graphit-iC™ coating was was considerably more noble than AISI 316L at about 0.65 V/RHE in aerated conditions. This was also comparable to the other carbon based coatings in the literature shown in Table 6.5. The current density at 0.8 V/RHE met the US DoE target and was below 1 μAcm^{-2}. However, notably there was no passive region for this coating or any other carbon based material suggesting that they will always be in an active state, albeit with a very low corrosion current. The sudden increase in corrosion current at ~ 1.4 V/RHE was attributed to the formation of soluble chromate ions from areas where carbon had been removed by corrosion, exposing the underlying substrate.

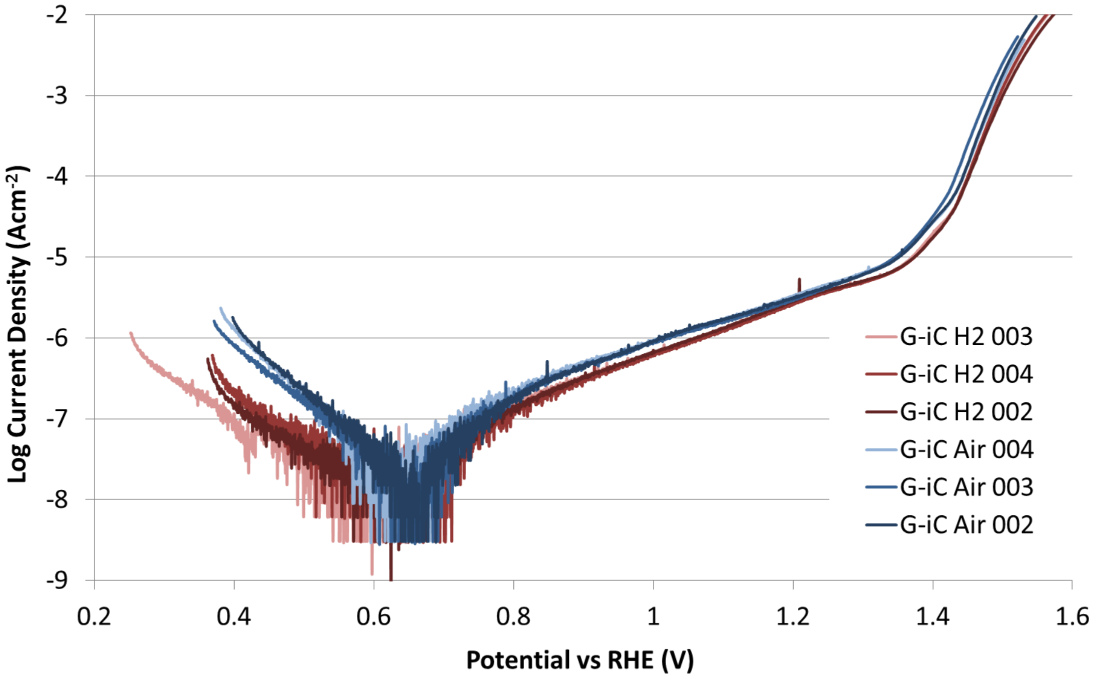

Figure 6.8 Potentiodynamic measurements of 1 µm Graphit-iC™ coated 100 µm 316L foil at 1 mV/s in 70°C 0.5 M H_2SO_4 bubbled with air or hydrogen

SEM examination of the coating after the polarisation test (Figure 6.9), identified large (<300 µm) spots of corrosion, with the majority of the coating being in good condition. It is suggested that the corroded areas observed originated from defect sites in the coating.

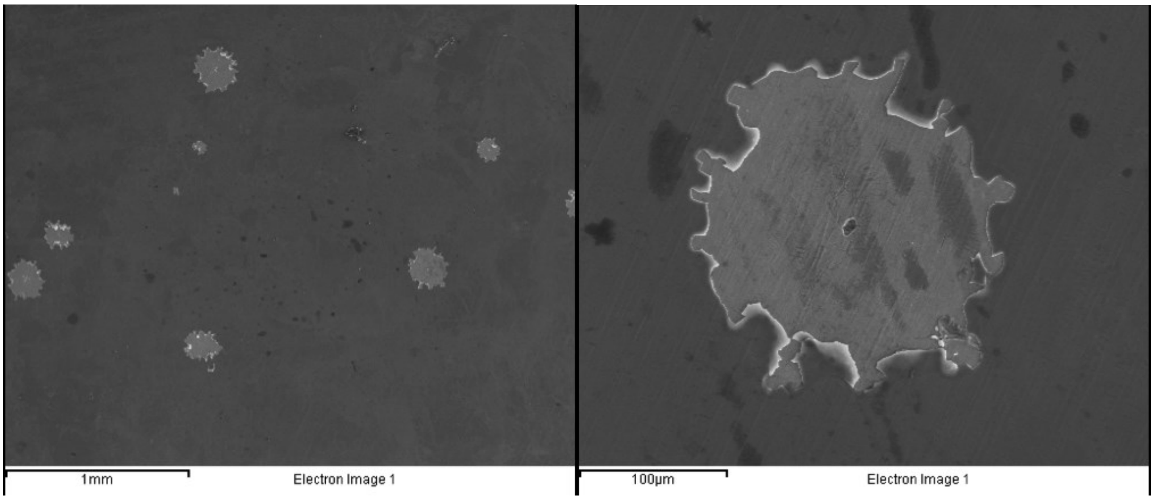

Figure 6.9 SEM images of Graphit-iC™ coating after the potentiodynamic test at low (left) and high (right) magnification

The Graphit-iC™ polarisation results were generally in good agreement with similar carbon coatings found in the literature, as shown in Table 6.5.

Table 6.5 Potentiodynamic polarisation parameters of carbon based coatings on 316L from the literature

Substrate & Coating	**Experimental Conditions**	**E_{corr} (standardised to V/RHE)**	**I_{corr} (μAcm^{-2})**	**Reference**
Polished 316L with 3 μm magnetron sputtered carbon coating	0.5 M H_2SO_4 solution with 2 ppm HF at 80 °C	0.49 (Air) 0.43 (H_2)	-	Feng et al. [179]
Polished 316L with a 200 nm magnetron sputtered carbon coating	1 M H_2SO_4 solution with 5 ppm HF at 70 °C	0.595 (Air)	0.13	Larijani et al. [189]
Polished 316L with 3 μm magnetron sputtered carbon coating (with Cr transition layer)	0.5 M H_2SO_4 solution with 2 ppm HF at 80 °C	0.498 (Air) 0.486 (H_2)	0.06	Feng et al. [178]

6.1.6 CrN+C

At 0.65 V/RHE, the E_{corr} of the CrN+C coating was similar to the other carbon based coatings. The current density at 0.8 V/RHE was around 0.1 μAcm^{-2}. At higher potentials the thin carbon topcoat provided limited protection before the current density started to rapidly increase at ~ 1.2 V/RHE. This was attributed to the exposure of the underlying CrN and the consequent formation of soluble chromate ions as observed for both the AISI 316L and the CrN coating. This increase occurred at a lower potential than the 1 μm Graphit-iC™ coating which was credited to the significantly thinner carbon topcoat in the order of 100 nm. The mode of failure also appeared to differ from the Graphit-iC™ coating, with a greater number of defects as shown in Figure 6.11. Visible pieces of black carbon were also observed in the electrolyte after testing, suggesting widespread delamination of the carbon topcoat. This suggests that the CrN layer may be preferentially attacked at these higher potentials. No studies in the literature with an equivalent multi layered coating were found with which to compare these results.

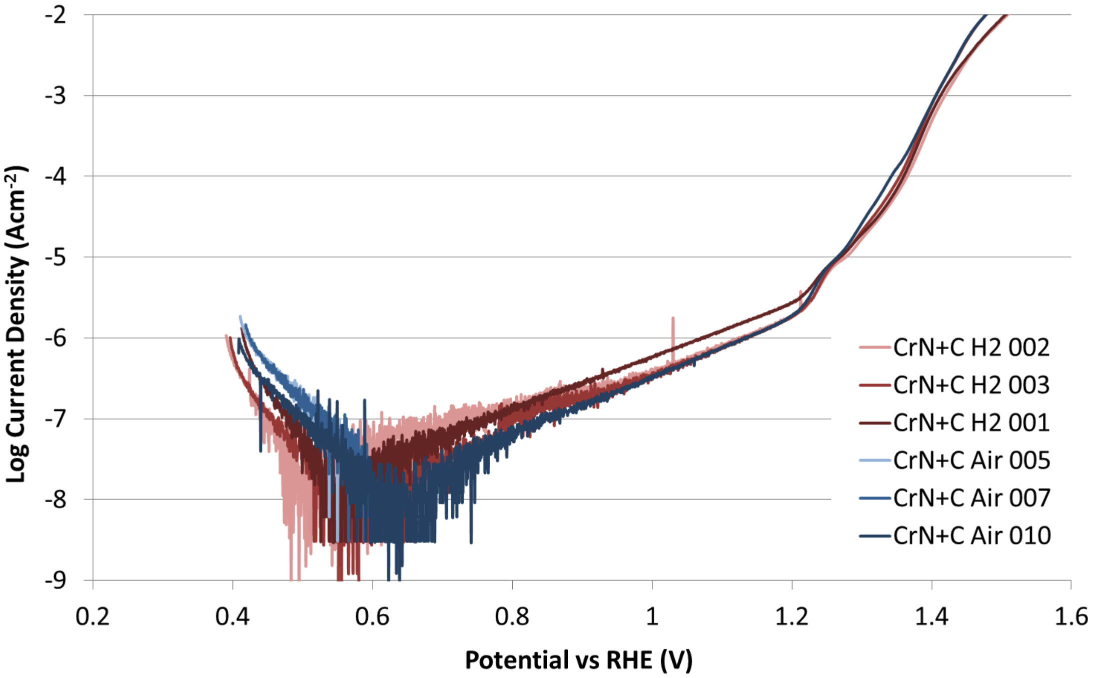

Figure 6.10 Potentiodynamic measurements of 0.4 µm CrN + 0.1 µm Carbon coated 100 µm 316L foil at 1 mV/s in 70°C 0.5 M H_2SO_4 bubbled with air or hydrogen

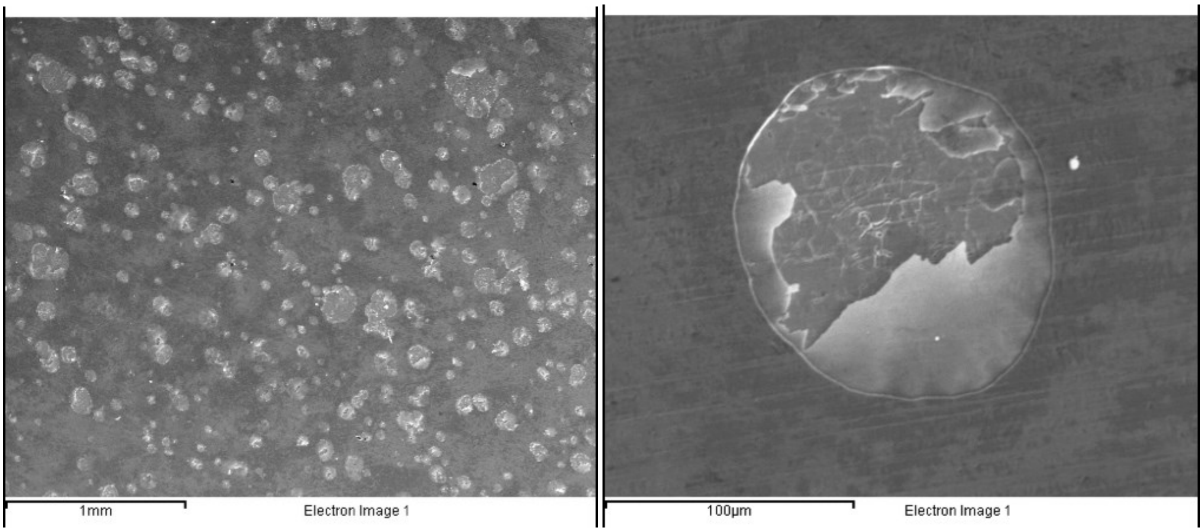

Figure 6.11 SEM images of CrN+C coating after the potentiodynamic test at low (left) and high (right) magnification

6.1.7 TiN+C

As shown in Figure 6.12, the E_{corr} of the TiN+C coated 316L, at about 0.65 V/RHE, was again similar to the other carbon based coatings. This was also a dramatic improvement compared to the TiN only coating under these conditions. The current density at 0.8 V/RHE was well below 1 μAcm^{-2}, thus meeting the US DoE target. At higher potentials the carbon was gradually removed, and was eventually stripped off completely exposing the TiN, and resulting in a drop in current density back to a comparable current density level to the TiN only coating at a comparable potential. No studies in the literature with an equivalent multi layered coating were found with which to compare these results. Figure 6.13 and Figure 6.14 shows that the TiN underlayer was generally in good condition after the measurement was finished, apart from some isolated defect areas where pitting corrosion of the substrate had occurred, which was attributed to the very high potentials reached during the polarisation scan (<2.2 V/RHE). The pits observed in Figure 6.14 showed that the underlying AISI 316L substrate was being corroded at a higher rate than the coating, leading to a clear subsidence of the coating, most likely due to a galvanic process at higher potentials. Compared to the CrN+C coating described previously, the TiN underlayer appeared to give better stability to the carbon topcoat at higher potentials.

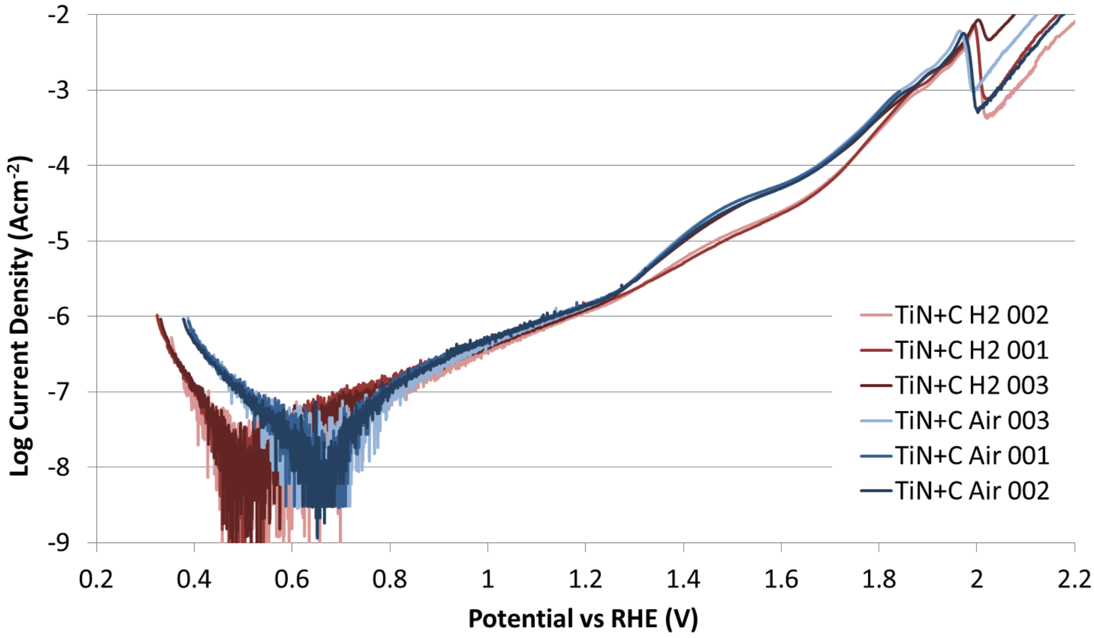

Figure 6.12 Potentiodynamic measurements of 0.4 µm TiN + 0.1 µm Carbon coated 100 µm 316L foil at 1 mV/s in 70°C 0.5 M H_2SO_4 bubbled with air or hydrogen

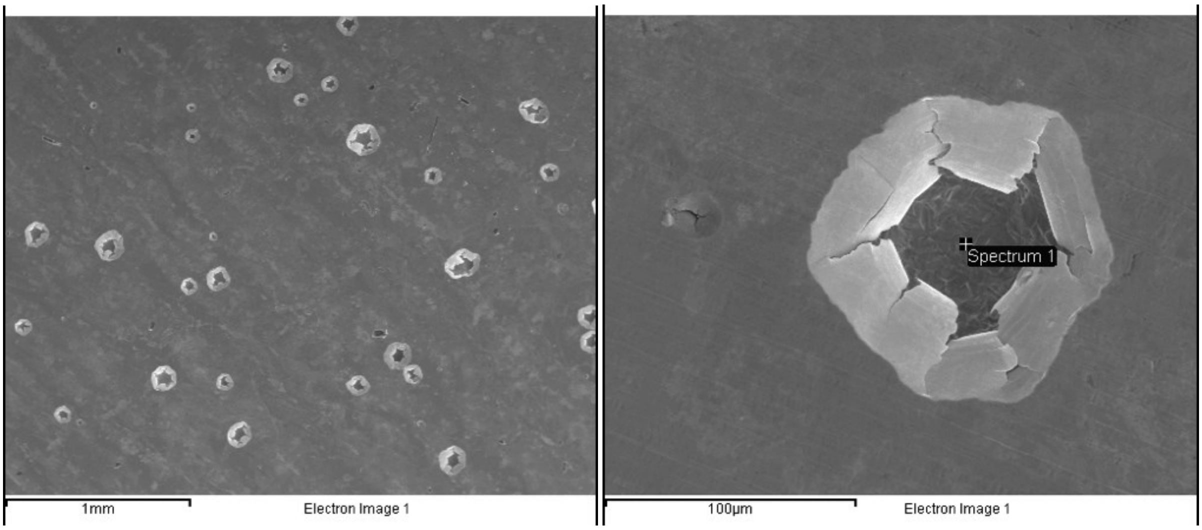

Figure 6.13 SEM images of TiN+C coating after the potentiodynamic test (<2.2 V/RHE) at low (left) and high (right) magnification showing pitting of the substrate underneath the TiN layer.

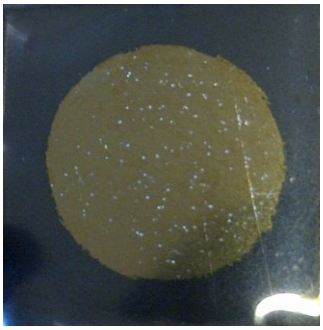

Figure 6.14 Photo of TiN+C coating after the potentiodynamic test showing the loss of the carbon topcoat and some pitting of the underlying substrate

6.1.8 Gold Coating (10 nm)

As shown in Figure 6.15, despite the very low thickness of the gold coating, the E_{corr} showed a large positive shift compared with the AISI 316L substrate. A large passive region between 0.6 and 1.1 V/RHE was observed, with current densities of 0.17 μAcm^{-2} at 0.8 V/RHE which was still below 1 $\mu A/cm^2$ even under the fuel cell cathode stand-by potentials (<1 V/RHE). An increase in current density was observed from 1.1 V/RHE with a small peak at 1.25 V/RHE. Further work with pure Au foil should be carried out identify if this peak is likely to be the oxidation of Au. The only similar study in the literature with which to compare these results, was carried out by Kumar et al. [151]. In this study, the corrosion resistance of a mechanically clad, 10 nm Au Nanoclad® coating from Daido Steel was examined (although under different experimental conditions of 0.5 mM H_2SO_4 (pH 3)). These authors also observed a positive shift in the E_{corr} (0.465 V/RHE under aerated conditions), a passive region between 0.5 and 1.1 V/RHE with current density of <2 μAcm^{-2}, and an increase in current density from 1.1 V/RHE, which was attributed the oxidation of Au to Au^{3+}.

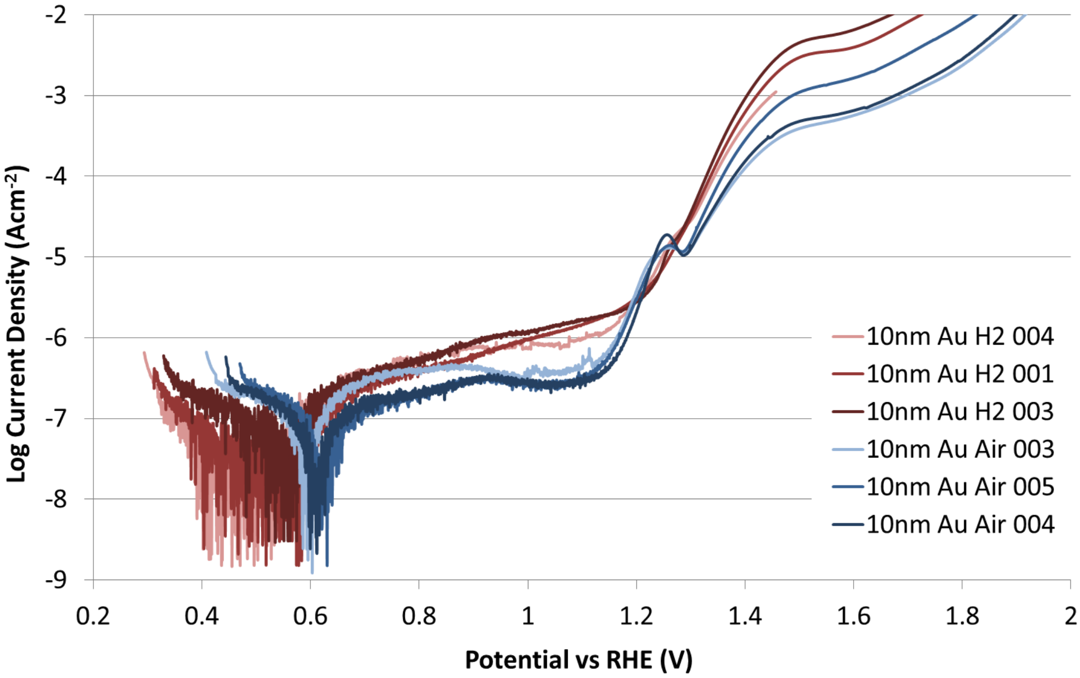

Figure 6.15 Potentiodynamic measurements of 10 nm Au coated 100 µm 316L foil at 1 mV/s in 70 °C 0.5 M H_2SO_4 bubbled with air or hydrogen

6.1.9 Discussion

A comparison of the PVD coatings potentiodynamic measurements in hydrogen and air are shown in Figure 6.16 and Figure 6.17. A comparison of the E_{corr} and current densities at potentials expected during fuel cell operation (0.8 V/RHE), stand-by (1 V/RHE) and start up conditions (1.4 V/RHE) is listed in Figure 6.18 and Figure 6.19. It was apparent that under these corrosion test conditions (0.5 M H_2SO_4 at 70 °C), the E_{corr} of all the amorphous carbon based coatings (TiN+C, CrN+C and Graphit-iC™), CrN, and Au coatings were notably nobler than the AISI 316L substrate. These coatings also met the US DoE target of <1 μAcm^{-2} at the expected operational fuel cell cathode potential of 0.8 V/RHE. Although the E_{corr} of ZrN and TiN were less noble, both of these coatings showed lower current densities at higher potentials of 1.4 V/RHE, which was attributed to a greater stability of the metal oxide layer at these potentials. This was a particular oxide advantage over Cr based materials and coatings (316L, CrN, CrN+C) which all showed significant increases in current density from 1.1 V/RHE onwards, which was attributed to the formation of soluble chromate ions. The TiN+C coating showed the best combination of an improved corrosion potential along with greater stability of the carbon topcoat at higher potentials, and as such, would make a good, non-noble metal candidiate for the cathode side of the bipolar plate.

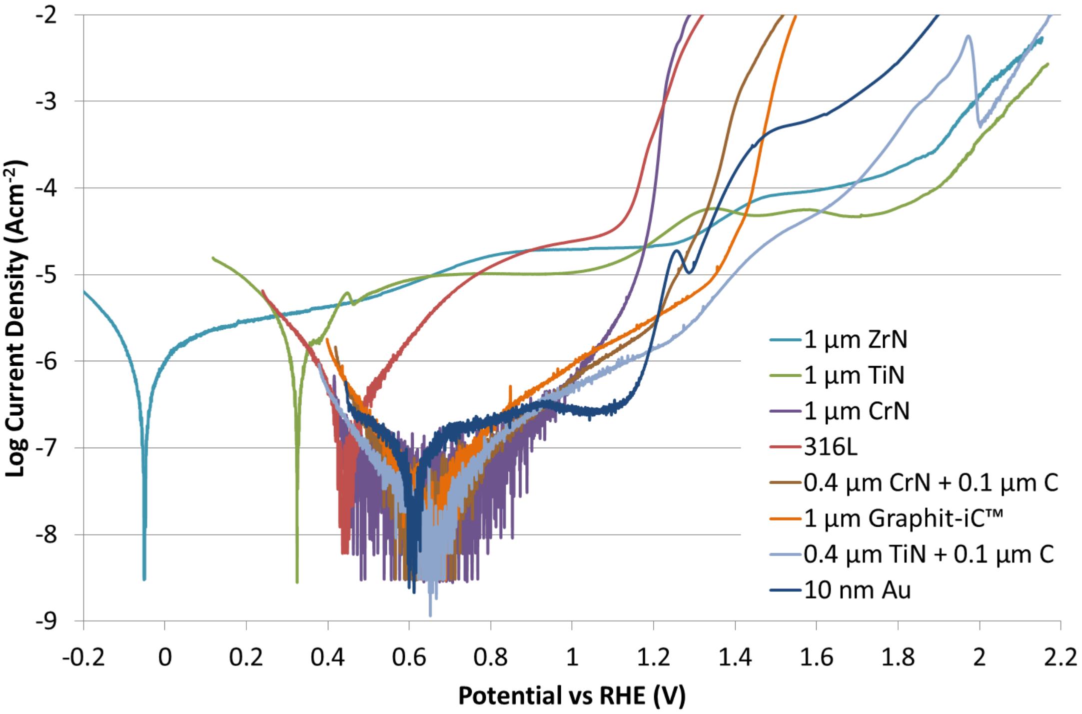

Figure 6.16 Potentiodynamic measurements of PVD coatings at 1 mV/s in 70°C 0.5 M H_2SO_4 bubbled with air

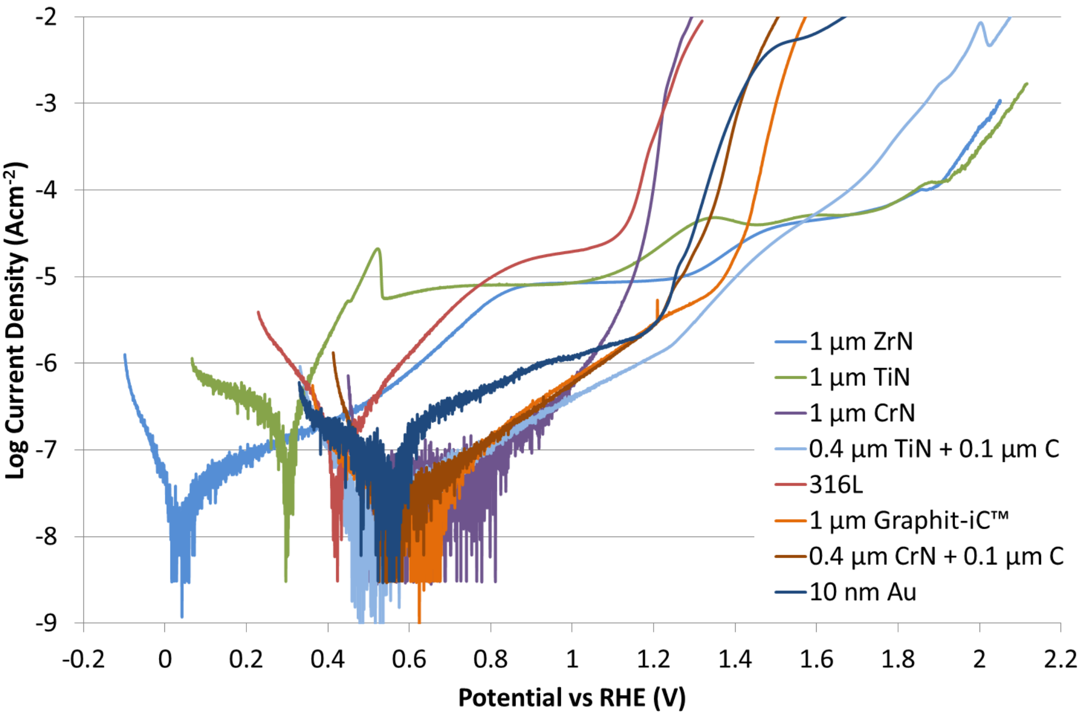

Figure 6.17 Potentiodynamic measurements of PVD coatings at 1 mV/s in 70 °C 0.5 M H_2SO_4 bubbled with hydrogen

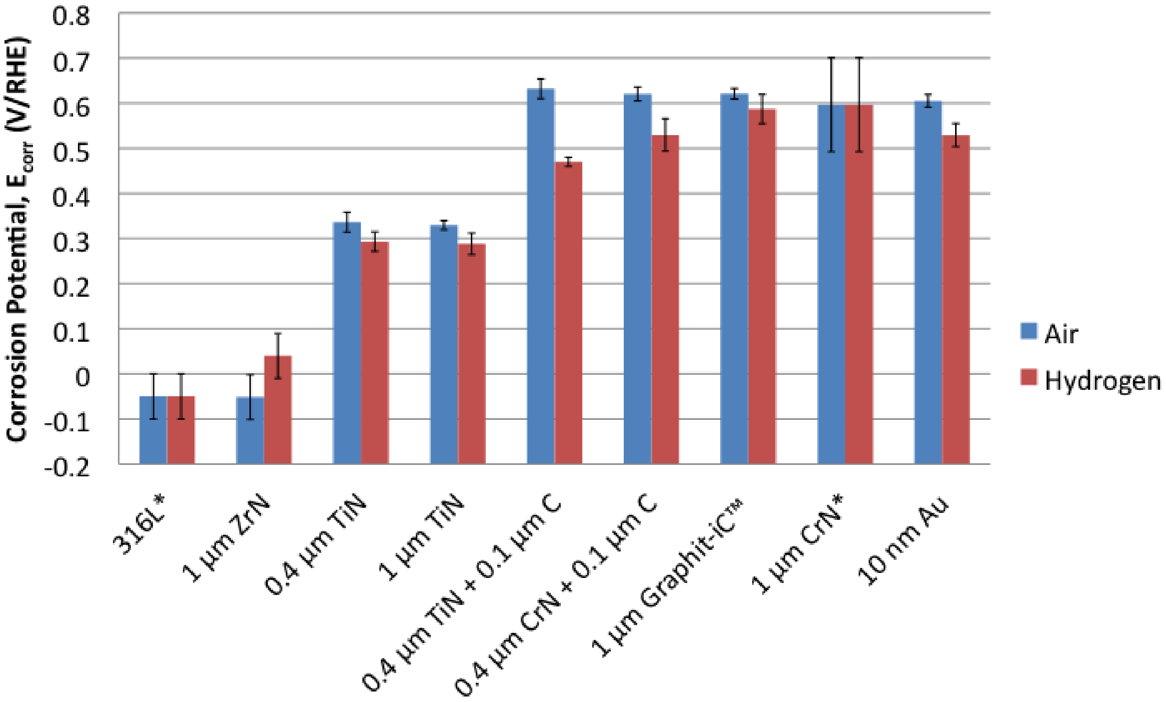

Figure 6.18 Summary of PVD coatings' E_{corr} when bubbled with air or hydrogen in 70 °C 0.5 M H_2SO_4

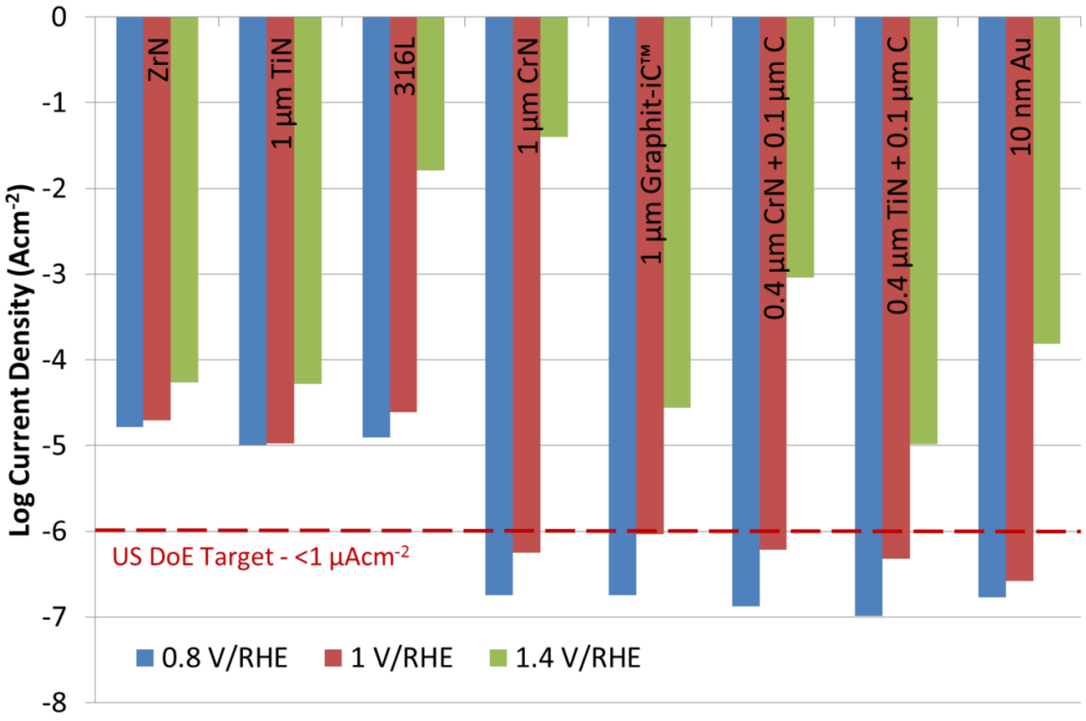

Figure 6.19 Summary of PVD coatings' current density at anodic potentials expected during fuel cell operation (0.8 V/RHE), stand-by (1 V/RHE) and start up conditions (1.4 V/RHE) when bubbled with air in 0.5 M H_2SO_4 at 70 °C

6.2 Potentiostatic Measurements

A simulated cathodic standby condition of 1 V/RHE was chosen rather than the less severe operating condition of 0.8 V/RHE as it seemed reasonable to assume that a fuel cell may spend some time on standby, especially if used in conjunction with a battery as is often done for automotive applications. The higher potentials experienced during start up/shut down or fuel starvation (<1.4 V/RHE) conditions were not examined as it is unclear at this time how effective system mitigation strategies are and consequently how significant an issue this is. Figure 6.20 shows the change in current density during a 1 V/RHE potentiostatic test over a period of 14 h.

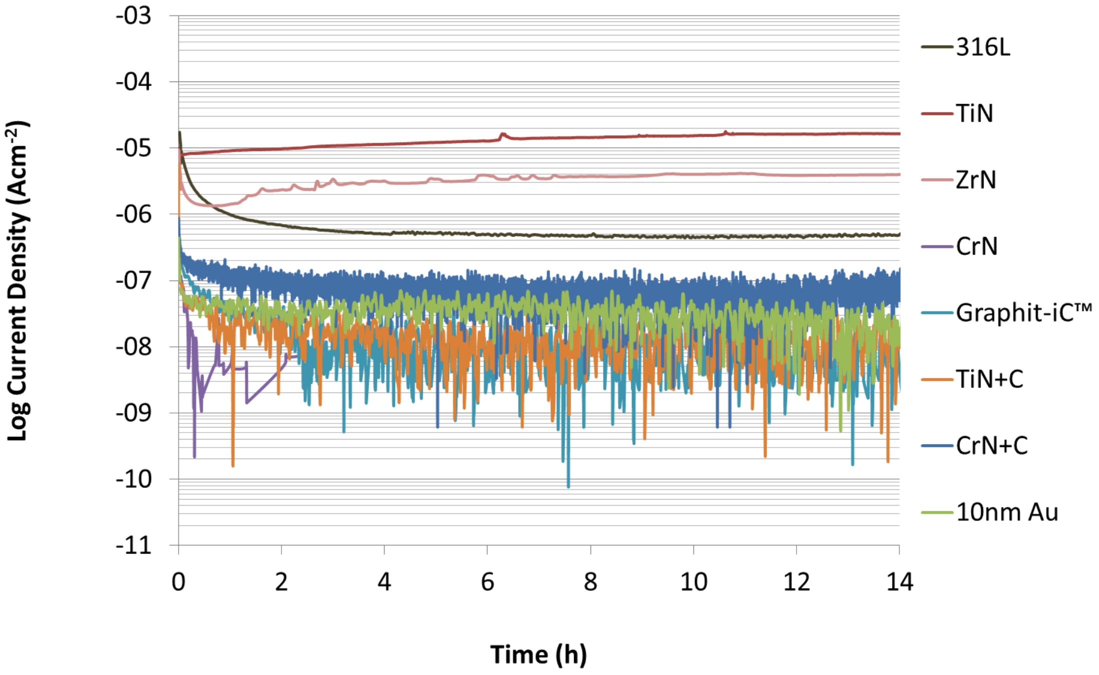

Figure 6.20 Potentiostatic measurement under cathodic simulated standby conditions of PVD coatings (1 V/RHE bubbled with air in 70 °C 0.5 M H_2SO_4 for 14 h)

The current density recorded for the samples in this test was the culmination of both the coating and any defects which may have exposed any interlayers or the substrate. The carbon based (Graphit-iC™, CrN+C, TiN+C) and Au coated AISI 316L showed the lowest current densities of <0.1 μAcm^{-2} at 1 V/RHE, although the exact current densities were obscured by possible electrical noise at this very low level. The carbon based coatings' current density was slightly lower than other values in the literature, as shown in

Table 6.6, but this was attributed to either slightly different testing conditions or deposition methods.

Table 6.6 Carbon based coatings' cathodic corrosion current densities

Coating and deposition method	Cathodic Conditions	Current density (μAcm^{-2})	Reference
Carbon (with Cr transition layer) deposited on 316L by CFUBMSIP	80°C, purged with air, 8.9 h, 0.6 V/SCE, 0.5 M H_2SO_4 + 2 ppm F^-	2.4	Feng et al. [178]
Carbon deposited on 316L by CFUBMSIP	80°C, purged with air, 8.9 h, 0.6 V/SCE, 0.5 M H_2SO_4 + 2 ppm F^-	2.4	Feng et al. [179]
Carbon (with Cr) deposited on 316L by pulsed bias arc ion plating (S6)	70°C, purged with air, 7 h, 0.6 V/SCE, 0.5 M H_2SO_4 + 5 ppm F^-	1	Wu et al. [202]
Carbon deposited on 304 by CFUBMSIP	80°C, purged with air, 8.9 h, 0.6 V/SCE, 0.5 M H_2SO_4 + 2 ppm F^-	2.1	Jin et al. [180]

The CrN coated AISI 316L current density was even lower than the carbon based coatings as also observed in the literature (see Table 6.7) and could not be plotted on the log axis entirely due to the frequent excursions below 0 $\mu A/cm^2$ after 0.25 h due to electrical noise.

Table 6.7 CrN coatings' cathodic corrosion current densities

Coating and deposition method	Cathodic Conditions	Current density ($\mu A/cm^2$)	Reference
CrN deposited on 316L by pulsed bias arc ion plating	70°C, purged with air, 2.8 h, 0.6 V/SCE, 0.5 M H_2SO_4 + 5 ppm F^-	0.1	Fu et al. [211]
CrN/Cr multilayer deposited on 316L by pulsed bias arc ion plating	70°C, purged with air, 7.5 h, 0.6 V/SCE, 0.5 M H_2SO_4 + 5 ppm F^-	0.025	Zhang et al. [174]

The AISI 316L substrate also showed a current density of <1 μAcm^{-2} after one hour suggesting reasonable protection by the passive oxide layer under these conditions. This finding may initially seem to contradict the work of Andre et al. [124] who suggested that cathodic stand-by conditions of 1 V/RHE resulted in excessive cation release compared to operating conditions of 0.8 V/RHE. However, this may be explained by the aging tests done in their work being considerably longer in duration of 500 h.

The ZrN coated AISI 316Ls' current density seemed to be relatively stable at a higher value of 4 μAcm^{-2} after 14 h. In contrast, the TiN coating which did not seem to stabilise over the duration of the test was 16.5 μAcm^{-2} and still rising after 14 h. Although the TiN coating appeared to have been visually removed after the test, XPS quantification of the surface did not detect any Fe or Cr at the surface as previously shown in Section 4.4.1. Similarly to this work, high current densities of TiN PVD coatings AISI 316L have been reported elsewhere; however, there have also been reports of relatively low values in less concentrated solutions as shown in Table 6.8.

Table 6.8 TiN coatings' cathodic corrosion current densities

Coating deposition method	**Cathodic Conditions**	**Current density (μA/cm^2)**	**Reference**
PVD	70°C, purged with air, 4 h, 0.6 V/SCE, 1 M H_2SO_4	18	Wang et al. [152]
Electron beam physical vapor deposition	70°C, purged with O_2, 1 h, 0.6 V/SCE, 0.5 M H_2SO_4	~30	Wang & Northwood [117]
Multi-arc ion plating	70°C, purged with air, 4 h, 0.6 V/SCE, 0.05 M H_2SO_4 + 2 ppm F^-	2.4	Tian & Sun [201]

From these results it would appear that TiN coatings may be particularly sensitive to changes in electrolyte concentration, although a more systematic study is needed. If this were found to be the case, then the use of electrolyte concentration as an accelerated stress variable would not be appropriate as reactions may be occuring that would not normally under fuel cell conditions. This could result in the unnecessary elimination of TiN as a viable coating option.

Limitations

Whilst the results suggest that several coatings achieve the DoE target of <1 μAcm^{-2} under cathodic simulated standby conditions, there are several important qualifications.

- Historically the DoE target has not stated the conditions under which the target is to be met. Only relatively recently have conditions been specified [212], although the reasons for these particular conditions and their validity for in-situ tests have not yet been explained that the author is aware of.
    - Anode corrosion conditions – pH 3, 0.1 ppm HF, 80°C, peak active current $< 1\text{x}10^{-6}$ A/cm^2 (potentiodynamic test at 0.1 mV/s, -0.4V to +0.6V(Ag/AgCl)), de-aerated with Ar purge.
    - Cathode corrosion conditions – pH 3, 0.1 ppm HF, 80°C, passive current $< 5\text{x}10^{-8}$ A/cm^2 (potentiostatic test at +0.6 V (Ag/AgCl) for >24 h, aerated solution.

- The design of experiment may not be realistic when compared to in-situ conditions as previously discussed in section 2.5.3

- Some areas of crevice corrosion were observed under the area of the PTFE gasket for some samples which may have resulted in higher than recorded current density values. This issue may be avoided in the future by using an Avesta cell to create a crevice free border by using a filter paper ring flooded with distilled water.

- This approach cannot distinguish between the corrosion current generated from the coating material itself and from that of defect sites. The overall current seen is likely to be dependant on the relationship between the particular coating and substrate materials. A solution to this problem may be the implementation of electrochemical impedance spectroscopy (EIS).

6.3 Summary

The method carried out in this work gives a qualitative indication under these simplified conditions of the PVD coatings' resistance to corrosion in the fuel cell environment. It serves as a benchmark test for the identification of promising materials without having to carry out long term in-situ fuel cell testing, which would take ~7 months for an automotive simulation (5000 hrs). In the potentiodynamic tests the corrosion potential (E_{corr}) increased in the following order (ZrN << TiN < Graphit-iC™, CrN+C ≈ TiN+C ≈ CrN ≈ Au. Similarly, although not quite identically in the cathodic simulation of 1 V/RHE standby potentials the corrosion current density decreased in the order TiN > ZrN > Graphit-iC™ ≈ TiN+C ≈ CrN+C ≈ CrN ≈ Au. The addition of a carbon topcoat to TiN was found to have two beneficial effects, dramatically improving the free corrosion potential and improving the stability of carbon at higher potentials. Not excluding the limitations of this work as previously highlighted, these results have shown that carbon based, CrN and Au coatings were the most suitable PVD coating candidates for bipolar plates. It was also established that the US DoE target of <1 μAcm^{-2} was not a particularly helpful target as the test conditions or relation to in-situ realities have not as of yet been clearly defined.

Further work

This chapter has established that there are many further avenues to explore including;

- Improving the quality of data for carbon based, CrN and Au coated samples through better electronic shielding, using larger sample surface areas (10 cm^2) and higher temperatures (80 °C).

- Potentiostatic tests under anodic working conditions (H_2 and 0.1 V/RHE)

- A systematic investigation of the effect of electrolyte concentration and potential on the corrosion of coatings.

- The impact of crevice and galvanic localised corrosion mechanisms on the corrosion of the coatings.

- The measurement of metal ion concentrations in the elecrolyte after corrosion tests.

- The use of a potentiodynamic load cycling profile to mimic potentials experienced in an operating fuel cell stack and long term *in-situ* tests to validate these test protocols.

CHAPTER 7

GENERAL DISCUSSION

7 General Discussion

The aim of this brief chapter is to discuss the most favourable coating/s in light of the combined data from the last three chapters on interfacial contact resistance (ICR), stamping and corrosion.

The metal nitride coatings (ZrN, TiN and CrN) all showed better ICRs than their metal oxide equivalents. However, the ICR of ZrN and TiN did not appear to be low enough to meet the current US DoE target of < 20 mΩ cm^2 at 140 N/cm^2 from the data shown in Chapter 4. CrN showed a both an acceptable ICR before the corrosion test and good performance during the potentiostatic corrosion test; however, after the test, the ICR was found to have increased beyond the US DoE target. The stability of CrN beyond 1 V/RHE during the potentiodynamic test was also of concern. The current densities of ZrN and TiN coatings were higher than the US DoE target during the potentiostatic test (in 0.5 M H_2SO_4); however, in contrast to CrN, the potentiodynamic tests showed some improved stability at higher potentials which could provide some protection to the substrate at higher potentials up to 1.5 V/RHE. Whilst not all of the nitrides were tested in the stamping trials, metal nitride coatings are typically used as hard, wear resistant coatings, which may indicate a similarly poor behaviour in the stamping trials.

The gold based coating showed the best ICR before and after potentiostatic corrosion tests (in which it also performed well). A potential issue in terms of performance with this coating could be incomplete surface coverage due the very low thickness which may lead to the attack of the substrate at high potentials. This would promote the idea of a thicker protective interlayer to protect the substrate from any defects in the gold coating. A second, more considerable area of concern, is the cost of gold for mass production. Even after a drop in price around 2012/13, the cost was still ~£28 per gram in August 2013. It is questionable if gold will ever be a viable coating option if the US DoE target of $3/kW for the entire bipolar plate is to met (the target includes manufacturing, material and processing costs). These two arguments would appear to have been addressed with the Treadstone ‘coating’ concept, as previously discussed in Section 2.6.2. This has a protective insulating oxide under layer and nano dots of gold rather than a continuous coating, although public data on in-situ performance is limited. The effect of stamping on this type of coating is also not known.

The carbon based coating, Graphit-iC™, gave excellent ICR values both before and after the potentiostatic corrosion test. However, it gave poorer protection to the substrate at higher potentials during the potentiodynamic corrosion test due to the attack at defect sites and the subsequent exposure of the substrate. This could be an issue for automotive applications that may experience many start up/shut downs and their associated high potentials. Another potential concern that may exacerbate the problem is that cost effectiveness would dictate that the thinnest possible coating is used and this would be likely to exacerbate the situation. The addition of a carbon topcoat to a nitride (TiN+C or CrN+C) was seen as a potential solution. The carbon effectively sealed the nitride layer from becoming oxidised and gave excellent ICR. With regards to corrosion, the potentiostatic tests showed current densities below the US DoE target for both coatings. The potentiodynamic test showed improved corrosion resistance at higher potentials in the case of the TiN+C. Finally, the addition of a carbon topcoat was also found to give benefits in the stamping tests with the coating showing less damage than the nitride only coating. Further validation of this coating in in-situ field trials is necessary to optimise the coating thickness and ensure that the conclusions drawn from the ex-situ data in this work are sound.

CHAPTER 8
CONCLUSIONS

8 CONCLUSIONS

This work investigated the suitability of thin film bipolar plate coatings produced by Physical Vapour Deposition (PVD) for PEM fuel cells. Due to the multifunctional nature of this component, it was not considered prudent to look exclusively at one attribute in isolation. For example, a coating with excellent corrosion resistance may not have sufficient conductivity, or a coating with both these qualities may not have other relevant properties such as good adhesion. Consequently, a more comprehensive approach was used where the bipolar plate coatings were more widely studied to determine several different properties.

Whilst the Interfacial Contact Resistance (ICR) of the bipolar plate provides a relatively small contribution to the overall ohmic losses in a fuel cell, it is important to minimise these in order to give optimal performance. As a result, several different substrate (AISI 316L) and coating factors were examined.

Similarly to the results found in the literature, the substrate surface roughness was found to influence the ICR, particularly when the surface was very smooth. However, it was also found that the addition of a conductive Graphit-iC™ coating to said surfaces negated any previously observed effect. Manufacturing conditions, such as chemical etching, were also found to have an effect on the measured ICR of the substrate, with greater etching times being associated with a lower ICR. This was presumably due to the modification of the passive oxide film although further surface analysis was not carried out in this work. Similarly to the influence of surface roughness on ICR, the addition of a conductive Graphit-iC™ coating to the etched surfaces negated any previously observed effect. It was presumed that any chemical modification of the surface caused by chemical etching was made redundant by the ion cleaning process prior to coating deposition.

PVD coating type was found to have a significant effect, with the ICR of 1 μm PVD coatings decreasing over orders of magnitude in the following order; ZrN > TiN > CrN > Carbon based coatings > Au. The variation of coating thicknesses from 0.1 – 1.1 μm resulted in no significant effect on the ICR for the Graphit-iC™ coating. The addition of a thin layer (0.1 – 0.2 μm) of amorphous carbon to the surface of TiN and CrN coatings resulted in a striking reduction in the ICR to a comparable level to that of Graphit-iC™. This suggested that the primary resistance of the metal nitride coatings was located at the GDL/coating interface, rather than the coating/substrate interface. Further examination of the nitride coatings by XPS confirmed the existence of a metal oxide, the percentage of which could be linked directly to the ICR. The addition of oxygen to a carbon coating via oxygen plasma treatment was also found to have a detrimental effect on the ICR of carbon coatings with changes to the surface morphology and chemistry. After anodic potentiostatic tests for 14 h at 1 V/RHE the ICR was found to increase across all of the coating types, the extent of which could be broadly correlated with the increase in surface oxygen as determined by XPS. The short term in-situ test results were qualitatively in accordance with the ex-situ ICR results, with a lower ICR resulting in increased fuel cell performance. However, a quantitative correlation was not possible due to a number of factors as previously described. Longer term in-situ tests with application specific load profiles should be carried out to ensure the stability of the coatings in future work.

The viability of pre-coated PVD coatings for serial production via stamping was assessed in collaboration with an industrial partner. The coating durability was found to be influenced by several factors. In terms of coating type, the Graphit-iC™ coating, that is widely known to be softer and with a lower coefficient of friction, was found to be more suitable than the TiN coating. Rib position was also found to be a major factor in the degree of cracking experienced. This was attributed to a locally reduced strain at the outside edge ribs, due to the edges of the foil being drawn inwards during the stamping action. Coating thickness was found to play a lesser role. The addition of a thin carbon topcoat to the TiN coating noticeably improved the stamping behaviour compared to TiN only coatings.

The corrosion resistance of the coatings was simulated under simplified corrosion conditions to avoid having to carry out long term in-situ fuel cell testing, which would take ~7 months for an automotive simulation (5000 hrs). In the potentiodynamic tests the corrosion potential (E_{corr}) increased in the following order (ZrN << TiN < 316L < Graphit-iC™, CrN+C ≈ TiN+C ≈ CrN ≈ Au. Similarly, although not quite identically in the cathodic fuel cell simulation of 1 V/RHE standby potentials, the corrosion current density decreased in the order TiN > ZrN > 316L > Graphit-iC™ ≈ TiN+C ≈ CrN+C ≈ CrN ≈ Au. The addition of a carbon topcoat to TiN was found to have two beneficial effects, dramatically improving the E_{corr} and reducing the current density at higher potentials. Carbon based coatings with improved resistance ot oxidation at high potentials would appear to be a potential alternative to other expensive, but high performance noble metal coatings. Whilst these corrosion results were helpful in providing a qualitative indication of the PVD coatings corrosion resistance, caution in applying these results directly to in-situ performance is suggested due to a number of other factors that were not addressed in the design of experiment as elaborated previously.

In summary, a multi-layered coating with a thin (~200 nm) carbon topcoat was shown to have numerous benefits relevant to bipolar plate coating performance, providing improvements in electrical contact resistance, stampability, corrosion resistance and material cost reduction.

Further Work

The scope of this work has been very broad due to the abundance of factors that must be considered in the manufacture of bipolar plates. As a result, this approach has identified many avenues for further work as described in more detail at the end of each chapter. More broadly speaking these included;

- The development and validation of more accurate ex-situ ICR and corrosion tests.
- The development of a suitable in-situ accelerated stress test derived from long term tests with application specific load profiles.
- The investigation of bipolar plate forming methods on coating properties when applied before or after coating.
- Cost modelling of optimised multilayer coatings using serial PVD production methods and a comparison with alternative coating technologies.

9 REFERENCES

[1] Global Oil Depletion: An assessment of the evidence for a near-term peak in global oil production, http://www.ukerc.ac.uk/support/tiki-index.php?page=Global+Oil+Depletion, **2009**

[2] Intergovernmental Panel on Climate Change, Climate Change 2007 Fourth Assessment Report, http://www.ipcc.ch/ipccreports/assessments-reports.htm, **2008**

[3] D. Luthi, M. Le Floch, B. Bereiter, T. Blunier, J.-M. Barnola, U. Siegenthaler, D. Raynaud, J. Jouzel, H. Fischer, K. Kawamura and T.F. Stocker, *Nature*, **2008**, 453, 7193, 379-382

[4] UK Climate Change Act of 2008, http://www.official-documents.gov.uk/document/cm70/7040/7040.pdf, **2008**

[5] Health Effects of Climate Change in the UK, http://www.dh.gov.uk/en/publicationsandstatistics/Publications/PublicationsPolicyAndGuidance/DH_080702, **2008**

[6] N.H. Stern, *The Economics of Climate Change: The Stern Review*, Cambridge University Press **2007**

[7] A. Zuttel, A. Remhof, A. Borgschulte and O. Friedrichs, *Philosophical Transactions of the Royal Society A: Mathematical, Physical and Engineering Sciences*, **2010**, 368, 1923, 3329-3342

[8] J.M. And˙jar and F. Segura, *Renewable and Sustainable Energy Reviews*, **2009**, 13, 9, 2309-2322

[9] Fuel Cell System Cost - 2010, http://hydrogen.energy.gov/pdfs/10004_fuel_cell_cost.pdf, **2010**

[10] R. Mukundan, R. Borup, J. Davey, R. Lujan, D. Torraco, D. Langlois, F. Garzon, W. Yoon, A. Weber, M. Brady, G. James and S. Grot, *Accelerated Testing Validation, FY 2011 Annual Progress Report, DOE Hydrogen and Fuel Cells Program*, **2011**

[11] DoE Publication Table 3.4.14, http://www1.eere.energy.gov/hydrogenandfuelcells/mypp/pdfs/fuel_cells.pdf, p. 26, **2007**

[12] A.S. Woodman, E.B. Anderson, K.D. Jayne and M.C. Kimble, *AESF SUR/FIN Proceedings*, **1999**

[13] I. Bar-On, R. Kirchaina and R. Roth, *J. Power Sources*, **2002**, 109, 71-75

[14] K.S. Jeong and B.S. Oh, *J. Power Sources*, **2002**, 105, 58-65

[15] H. Tsuchiya and O. Kobayashi, *International Journal of Hydrogen Energy*, **2004**, 29, 985-990

[16] K. Jayakumar and N.R. S. Pandiyan, K.S. Dhathathreyan, *J. Power Sources*, **2006**, 161 454-459

[17] S.K. Kamarudin and A.M.S. W.R.W. Daud, M.S. Takriff, A.W. Mohammad, *J. Power Sources*, **2006**, 157, 641-649

[18] B. James, J. Kalinoski and K. Baum, *Mass Production Cost Estimation for Automotive Fuel Cell Systems*, Washington, DC, **June 9th 2010**

[19] J. Sinha and Y. Yang, Washington, DC **June 9, 2010**

[20] W. Gu, D.R. Baker, Y. Liu and H.A. Gasteiger, *Proton exchange membrane fuel cell (PEMFC) down-the-channel performance model. In Handbook of Fuel Cells – Fundamentals, Technology and Applications*, John Wiley & Sons, Ltd, Chichester, **2009**

[21] X.G. Li and I. Sabir, *Int. J. Hydrogen Energy*, **2005**, 30, 4, 359-371

[22] P.J. Hamilton and B.G. Pollet, *Fuel Cells*, **2010**, 10, 4, 489-509

[23] X.G. Li, I. Sabir and J. Park, *J. Power Sources*, **2007**, 163, 2, 933-942

[24] C.Y. Wang, *Chem. Rev.*, **2004**, 104, 4727-4766

[25] D.L. Wood, J.S. Yi and T.V. Nguyen, *Electrochim. Acta*, **1998**, 43, 24, 3795-3809

[26] G. Zhang, L. Guo, B. Ma and H. Liu, *J. Power Sources*, **2009**, 188, 1, 213-219

[27] J. Park and X. Li, *J. Power Sources*, **2007**, 163, 2, 853-863

[28] C. Xu and T.S. Zhao, *Electrochem. Comm.*, **2007**, 9, 3, 497-503

[29] H. Li, Y. Tang, Z. Wang, Z. Shi, S. Wu, D. Song, J. Zhang, K. Fatih, J. Zhang, H. Wang, Z. Liu, R. Abouatallah and A. Mazza, *J. Power Sources*, **2008**, 178, 1, 103-117

[30] J.P. Owejan, T.A. Trabold, D.L. Jacobson, M. Arif and S.G. Kandlikar, *Int. J. Hydrogen Energy*, **2007**, 32, 17, 4489-4502

[31] X.G. Yang, F.Y. Zhang, A.L. Lubawy and C.Y. Wang, *Electrochem. Solid-State Lett.*, **2004**, 7, 11, A408-A411

[32] R.N. Wenzel, *Industrial and Engineering Chemistry*, **1936**, 28, 988-994

[33] R.L. Borup and N.E. Vanderborgh, *Materials Research Society Proceedings*, **1995**

[34] V. Mehta and J.S. Cooper, *J. Power Sources*, **2003**, 114, 1, 32-53

[35] J.S. Cooper, *J. Power Sources*, **2004**, 129, 2, 152-169

[36] A. Hermann, T. Chaudhuri and P. Spagnol, *Int. J. Hydrogen Energy*, **2005**, 30, 12, 1297-1302

[37] X.Z. Yuan, H. Wang, J. Zhang and D.P. Wilkinson, *J. New Mat. Elect. Syst.*, **2005**, 8, 4, 257-267

[38] D.J.L. Brett and N.P. Brandon, *J. Fuel Cell Sci. Tech.*, **2007**, 4, 29-44

[39] N. de las Heras, E.P.L. Roberts, R. Langton and D. R. Hodgson, *Energy & Environmental Science*, **2009**, 2, 2, 206-214

[40] Superior Graphite, http://www.superiorgraphite.com/brands-formula-bt, **2011**

[41] Timcal Graphite & Carbon, www.timcal.com/scopi/group/timcal/timcal.nsf/Attachment/A20B378FA3CF6D69C125745000501211/$file/Brochure_Carbon_Powders_for_Bipolar_Plates_of_Fuel_Cell.pdf, **2011**

[42] Entegris & Poco FFPs, http://www.entegrisfuelcells.com/Default.aspx, http://www.poco.com/, **2009**

[43] GrafTech International FFPs, http://www.graftechaet.com/GRAFCELL/GRAFCELL-Home.aspx, **2009**

[44] Mersen, http://www.mersen.com/en.html, **2011**

[45] Huntsman Advanced Materials GmbH, http://www.jeccomposites.com/directory/1004/Huntsman-Advanced-Materials-(Switzerland)-GmbH-profile.html, **2009**

[46] Ticona, http://www.ticona.com/home/markets/innovation/fuel_cell.htm, **2011**

[47] SGL Carbon Group FFPs, http://www.sglgroup.com, **2009**

[48] Schunk FFPs, http://www.schunk-group.com/en/sgroup/schunk01.c.42452.en,, **2009**

[49] Bac2 FFPs http://www.bac2.co.uk/, **2009**

[50] ZBT FFPs, http://www.zbt-duisburg.de/en/Technology/RD/fuelcells/BPP/, **2009**

[51] GraphTek LLC, http://graphtekllc.com/, **2011**

[52] Nisshinbo, http://www.nisshinbo-chem.co.jp/english/products/sepa.html, **2011**

[53] A.M. Abdullah, A.M. Mohammad, T. Okajima, F. Kitamura and T. Ohsaka, *J. Power Sources*, **2009**, 190, 2, 264-270

[54] BMC FFPs http://www.bulkmolding.com/datasheets/informational/BMC_940.pdf, **2009**

[55] Engineered Fibers Technology, USA, http://www.eftspectracorp.com/, **2011**

[56] Dana FFPs http://www.dana.com/, **2009**

[57] Sumitomo Metals, http://www.sumitomometals.co.jp/e/csr/program/pdf/report-e-2010-k1.pdf, **2011**

[58] Teer Coatings Ltd., www.teercoatings.co.uk, **2012**

[59] Precision Micro Ltd, http://www.precisionmicro.com/, **2010**

[60] Brandauer, http://www.brandauer.co.uk/, **2011**

[61] Cellimpact FFPs, http://www.morphic.se/en/Cellimpact/, **2009**

[62] Sandvik, www.sandvik.com, **2012**

[63] Impact Coatings AB, www.impactcoatings.se, **2012**

[64] http://www.tech-etch.com/photoetch/fuelcell.html,

[65] Borit, http://www.borit.be/, **2011**

[66] R. Taipalus, T. Harmia, M.Q. Zhang and K. Friedrich, *Compos. Sci. Technol.*, **2001**, 61, 6, 801-814

[67] P. Tsotra and K. Friedrich, *Compos. Sci. Technol.*, **2004**, 64, 15, 2385-2391

[68] R.A. Antunes, M.C.L.d. Oliveira, G. Ett and V. Ett, *J. Power Sources*, **2011**, 196, 2945–2961

[69] W. Thongruang, R.J. Spontak and C.M. Balik, *Polymer*, **2002**, 43, 8, 2279-2286

[70] S.R. Dhakate, R.B. Mathur, B.K. Kakati and T.L. Dhami, *Int. J. Hydrogen Energy*, **2007**, 32, 17, 4537-4543

[71] R.B. Mathur, S.R. Dhakate, D.K. Gupta, T.L. Dhami and R.K. Aggarwal, *J. Mater. Process. Tech.*, **2008**, 203, 1-3, 184-192

[72] J.A. King, R.L. Barton, R.A. Hauser and J.M. Keith, *Polym. Compos.*, **2008**, 29, 4, 421-428

[73] J.H. Lee, Y.K. Jang, C.E. Hong, N.H. Kim, P. Li and H.K. Lee, *J. Power Sources*, **2009**, 193, 2, 523-529

[74] S.I. Heo, J.C. Yun, K.S. Oh and K.S. Han, *Advanced Composite Materials*, **2006**, 15, 115-126

[75] R.A. Mercuri and J.J. Gough, *US Patent, 6,037,074,* **2000**

[76] GrafTech FFP worldwide use, http://www.graftechaet.com/grafcell/grafcell-Home.aspx, **2009**

[77] D. Li, Y. Wang, L. Xu, J. Lu and Q. Wu, *J. Power Sources*, **2008**, 183, 2, 571-575

[78] US DOE Progress, http://www.hydrogen.energy.gov/annual_progress09_fuelcells.html, **2009**

[79] L. Song and A.Z. J. Guo, B. Z. Jang, *US Patent, 7,566,410,* **2009**

[80] A. Heinzel, F. Mahlendorf, O. Niemzig and C. Kreuz, *J. Power Sources*, **2004**, 131, 1-2, 35-40

[81] M. Wu and L.L. Shaw, *J. Power Sources*, **2004**, 136, 1, 37-44

[82] R. Dweiri and J. Sahari, *J. Power Sources*, **2007**, 171, 2, 424-432

[83] S. Bouatia, F. Mighri and M. Bousmina, *Fuel Cells*, **2008**, 8, 2, 120-128

[84] F. Mighri, M.A. Huneault and M.F. Champagne, *Polym. Eng. Sci.*, **2004**, 44, 9, 1755-1765

[85] J. Huang, D.G. Baird and J.E. McGrath, *J. Power Sources*, **2005**, 150, 110-119

[86] B.D. Cunningham, J. Huang and D.G. Baird, *J. Power Sources*, **2007**, 165, 2, 764-773

[87] S. Radhakrishnan, B.T.S. Ramanujam, A. Adhikari and S. Sivaram, *J. Power Sources*, **2007**, 163, 2, 702-707

[88] L.G. Xia, A.J. Li, W.Q. Wang, Q. Yin, H. Lin and Y.B. Zhao, *J. Power Sources*, **2008**, 178, 1, 363-367

[89] T. Derieth, G. Bandlamudi, P. Beckhaus, C. Kreuz, F. Mahlendorf and A. Heinzel, *J. New Mat. Elect. Syst.*, **2008**, 11, 21-29

[90] R. Blunk, M.H.A. Elhamid, D. Lisi and Y. Mikhail, *J. Power Sources*, **2006**, 156, 2, 151-157

[91] L. Du and S.C. Jana, *J. Power Sources*, **2007**, 172, 2, 734-741

[92] I.U. Hwang, H.N. Yu, S.S. Kim, D.G. Lee, J.D. Suh, S.H. Lee, B.K. Ahn, S.H. Kim and T.W. Lim, *J. Power Sources*, **2008**, 184, 1, 90-94

[93] C. Du, P. Ming, M. Hou, J. Fu, Q. Shen, D. Liang, Y. Fu, X. Luo, Z. Shao and B. Yi, *J. Power Sources*, **2010**, 195, 3, 794-800

[94] S.I. Heo, K.S. Oh, J.C. Yun, S.H. Jung, Y.C. Yang and K.S. Han, *J. Power Sources*, **2007**, 171, 2, 396-403

[95] P.H. Maheshwari, R.B. Mathur and T.L. Dhami, *J. Power Sources*, **2007**, 173, 1, 394-403

[96] B.K. Kakati and V. Mohan, *Fuel Cells*, **2008**, 1, 45-51

[97] S.R. Dhakate, S. Sharma, M. Borah, R.B. Mathur and T.L. Dhami, *Int. J. Hydrogen Energy*, **2008**, 33, 23, 7146-7152

[98] C. Hui, L. Hong-bo, Y. Li and L. Jian-xin, *Int. J. Hydrogen Energy*, **2010**, 35, 7, 3105-3109

[99] B.K. Kakati, V.K. Yamsani, K.S. Dhathathreyan, D. Sathiyamoorthy and A. Verma, *Carbon*, **2009**, 47, 2413-2418

[100] L. Du, *Ph.D Thesis*, The University of Akron, Ohio, US, **2008**

[101] K. Immonen and J.H. K. Nättinen, J. Repo, J. Sarlin, , *PPS-24*, Salerno, Italy, **2008**

[102] R.H.J. Blunk, D.J. Lisi, Y.E. Yoo and C.L. Tucker III, *AIChE J.*, **2003**, 49, 18-29

[103] T.M. Besmann, J.J. Henry, J.W. Klett, E. Lara-Curzio and I.P. Kosacki, *Hydrogen and Fuel Cells Merit Review Meeting*, Berkeley, California, US, **2003**

[104] S.S. Hsieh, S.H. Yang, J.K. Kuo, C.F. Huang and H.H. Tsai, *Energ. Convers. Manage.*, **2006**, 47, 1868-1878.

[105] B. Luo, M. Hu, F. Li and G. Cao, *Int. J. Hydrogen Energy*, **2010**, 35, 7, 2643-2647

[106] A. Pozio, R.F. Silva, M. De Francesco and L. Giorgi, *Electrochim. Acta*, **2003**, 48, 11, 1543-1549

[107] The electrochemistry of corrosion, www.npl.co.uk/upload/pdf/the_electrochemistry_of_corrosion.pdf, **2013**

[108] H. Wang, M.A. Sweikart and J.A. Turner, *J. Power Sources*, **2003**, 115, 2, 243-251

[109] H. Wang and J.A. Turner, *Fuel Cells*, **2010**, 10, 4, 510-519

[110] D.P. Davies, P.L. Adcock, M. Turpin and S.J. Rowen, *J. Appl. Electrochem.*, **2000**, 30, 101-105

[111] P.L. Hentall, J.B. Lakeman, G.O. Mepsted, P.L. Adcock and J.M. Moore, *J. Power Sources*, **1999**, 80, 1-2, 235-241

[112] D.R. Hodgson, B. May, P.L. Adcock and D.P. Davies, *J. Power Sources*, **2001**, 96, 233-235

[113] S.-H. Wang, J. Peng, W.-B. Lui and J.-S. Zhang, *J. Power Sources*, **2006**, 162, 1, 486–491

[114] S.-J. Lee, C.-H. Huang and Y.-P. Chen, *J. Mater. Process. Tech.*, **2003**, 140, 1-3, 688-693

[115] M. Sulek, J. Adams, S. Kaberline, M. Ricketts and J.R. Waldecker, *J. Power Sources*, **2011**, 196, 8967 - 8972

[116] D.P. Davies, P.L. Adcock, M. Turpin and S.J. Rowen, *J. Power Sources*, **2000**, 86, 1-2, 237-242

[117] Y. Wang and D.O. Northwood, *J. Power Sources*, **2009**, 191, 483-488

[118] A. Kraytsberg, M. Auinat and Y. Ein-Eli, *J. Power Sources*, **2007**, 164, 2, 697-703

[119] B. Avasarala and P. Haldar, *J. Power Sources*, **2009**, 188 225–229

[120] J. Andre, L. Antoni, J.-P. Petit, E.D. Vito and A. Montani, *Int. J. Hydrogen Energy*, **2009**, 34, 3125 – 3133

[121] G. Hinds and E. Brightman, *Electrochem. Comm.*, **2012**, 17, 26-29

[122] H. Tawfik, Y. Hung and D. Mahajan, *J. Power Sources*, **2007**, 163, 2, 755-767

[123] R.A. Antunes, M.C.L. Oliveira, G. Ett and V. Ett, *Int. J. Hydrogen Energy*, **2010**, 35, 8, 3632–3647

[124] J. Andre, L. Antoni and J.-P. Petit, *Int. J. Hydrogen Energy*, **2010**, 35, 3684-3697

[125] C.A. Reiser, L. Bregoli, T.W. Patterson, J.S. Yi, J.D. Yang, M.L. Perry and T.D. Jarvi, *Electrochem. Solid-State Lett.*, **2005**, 8, 6, 273-276

[126] Y. Yu, H. Li, H. Wang, X.-Z. Yuan, G. Wang and M. Pan, *J. Power Sources*, **2012**, 205, 10–23

[127] K. Feng, G. Wu, Z. Li, X. Cai and P.K. Chu, *Int. J. Hydrogen Energy*, **2011**, 36, 13032-13042

[128] Y. Wang and D.O. Northwood, *Electrochim. Acta*, **2007**, 52, 6793–6798

[129] A. Agneaux, M.H. Plouzennec, L. Antoni and J. Granier, *Fuel Cells*, **2006**, 6, 1, 47-53

[130] D.E. Curtin, R.D. Lousenberg, T.J. Henry, P.C. Tangeman and M.E. Tisack, *J. Power Sources*, **2004**, 131, 41–48

[131] M. Inaba, H. Yamada, J. Tokunaga and A. Tasaka, *Electrochem. Solid-State Lett.*, **2004**, 7, 12, A474-A476

[132] W. Liu and D. Zuckerbrod, *J. Electrochem. Soc.*, **2005**, 152, A1165-A1170

[133] V.A. Sethuraman, J.A. Weidner, A.T. Haug, S. Motupally and L.V. Protsailo, *J. Electrochem. Soc.*, **2008**, 155, B50-B57

[134] C. Mele and B. Bozzini, *J. Power Sources*, **2010**, 195, 11, 3590-3596

[135] S.-J. Lee and J.-J. Lai, *J. Mater. Process. Tech.*, **2003**, 206–210

[136] J.-H. Huang, F.-Y. Ouyang and G.-P. Yu, *Surf. Coat. Technol.*, **2007**, 201, 7043-7053

[137] E. Dur, O.M. Cora and M. Koç, *J. Power Sources*, **2011**, 196, 3, 1235-1241

[138] M. Kumagai, S.-T. Myung, S. Kuwata, R. Asaishi and H. Yashiro, *Electrochim. Acta*, **2008**, 53, 4205-4212

[139] J. Wu, X.Z. Yuan, J.J. Martin, H. Wang, J. Zhang, J. Shen, S. Wu and W. Merida, *J. Power Sources*, **2008**, 184, 1, 104-119

[140] D.-H. Han, W.-H. Hong, H.S. Choi and J.J. Lee, *Int. J. Hydrogen Energy*, **2009**, 34, 2387 – 2395

[141] H. Wang, M.P. Brady, G. Teeter and J.A. Turner, *J. Power Sources*, **2004**, 138, 1-2, 86-93

[142] H. Wang, M.P. Brady, K.L. More, H.M. Meyer and J.A. Turner, *J. Power Sources*, **2004**, 138, 1-2, 79-85

[143] B. Yang, M.P. Brady, H. Wang, J.A. Turner, K.L. More, D.J. Young, P.F. Tortorelli, E.A. Payzant and L.R. Walker, *J. Power Sources*, **2007**, 174, 1, 228-236

[144] M.P. Brady, H. Wang, J.A. Turner, H.M. Meyer, K.L. More, P.F. Tortorelli and B.D. McCarthy, *J. Power Sources*, **2010**, 195, 5610-5618

[145] T.J. Toops, M.P. Brady, P.F. Tortorellia, J.A. Pihl, F. Estevez, D. Connors, F. Garzon, T. Rockward, D. Gervasio, W. Mylan and S.H. Kosaraju, *J. Power Sources*, **2010**, 195, 5619-5627

[146] M.P. Brady, T.J. Toops, K.L. More, H.M.M. III, P.F. Tortorelli, M.A. Elhamid, G. Dadheech, J. Bradley, H. Wang and J.A. Turner, *PEM Fuel Cell Metallic Bipolar Plates:*

Technical Status and Nitridation Surface Modification for Improved Performance, Trondheim, **2012**

[147] H. Wang and J.A. Turner, *Int. J. Hydrogen Energy*, **2011**, 36, 20, 13008-13013

[148] O. Lavigne, C. Alemany-Dumont, B. Normand, P. Delichère and A. Descamps, *Surf. Coat. Technol.*, **2010**, 205, 1870-1877

[149] K. Feng, Z. Li, X. Cai and P.K. Chu, *Materials Chemistry and Physics*, **2011**, 126, 6-11

[150] M.P. Brady, H. Wang, B. Yang, J.A. Turner, M. Bordignon, R. Molins, M.A. Elhamid, L. Lipp and L.R. Walker, *Int. J. Hydrogen Energy*, **2007**, 32, 16, 3778-3788

[151] A. Kumar, M. Ricketts and S. Hirano, *J. Power Sources*, **2010**, 195, 5, 1401-1407

[152] L. Wang, D.O. Northwood, X. Nie, J. Housden, E. Spain, A. Leyland and A. Matthews, *J. Power Sources*, **2010**, 195, 3814–3821

[153] I. Iordanova, P.J. Kelly, R. Mirchev and V. Antonov, *Vacuum*, **2007**, 81, 830–842

[154] J.-H. Huang, K.-W. Lau and G.-P. Yu, *Surf. Coat. Technol.*, **2005**, 191, 17-24

[155] K. Sarakinos, J. Alami and S. Konstantinidis, *Surf. Coat. Technol.*, **2010**, 204, 1661-1684

[156] K. Nygren, M. Samuelsson and B. Wälivaara, *MaxPhase™ coatings on bipolar plates deposited by magnetron sputtering techniques in a high throughput industrial coating system*, Trondheim, **2012**

[157] J. Wind, R. Spah, W. Kaiser and G. Bohm, *J. Power Sources*, **2002**, 105, 2, 256-260

[158] W. Yoon, X. Huang, P. Fazzino, Kenneth. L. Reifsnider and M.A. Akkaoui, *J. Power Sources*, **2008**, 179, 265–273

[159] I. Zafar and J.V.G. R. Timothy, N. Dave, , *World Patent, 0,128,019,* **2001**

[160] Y. Li and S.S. W.J. Meng, S.J. Harris, G.L. Doll, *US, 5,624,769,* **1995**

[161] T. Matsumoto and H.O. J. Niikura, M. Uchida, H. Gyoten, K. Hatoh, E. Yasumoto, T. Kanbara, K. Nishida, Y. Sugawara,, *European Patent 1,094,535,* **2001**

[162] R.F. Silva, D. Franchi, A. Leone, L. Pilloni, A. Masci and A. Pozio, *Electrochim. Acta*, **2006**, 51, 17, 3592-3598

[163] A. Pozio, F. Zaza, A. Masci and R.F. Silva, *J. Power Sources*, **2008**, 179, 2, 631-639

[164] Y. Wang and D.O. Northwood, *Int. J. Hydrogen Energy*, **2007**, 32, 7, 895-902

[165] M. Li, S. Luo, C. Zeng, J. Shen, H. Lin and C. Cao, *Corros. Sci.*, **2004**, 46, 6, 1369-1380

[166] B. Wu, Y. Fu, J. Xu, G. Lin and M. Hou, *J. Power Sources*, **2009**, 194, 976–980

[167] H.S. Choi, D.H. Han, W.H. Hong and J.J. Lee, *J. Power Sources*, **2009**, 189, 966-971

[168] M.M. Larijani, M. Elmi, M. Yari, M. Ghoranneviss, P. Balashabadi and A. Shokouhy, *Surf. Coat. Technol.*, **2009**, 203, 2591-2594

[169] J. Barranco, F. Barreras, A. Lozano, A.M. Lopez, V. Roda, J. Martin, M. Maza, G.G. Fuentes and E. Almandoz, *Int. J. Hydrogen Energy*, **2010**, 35, 11489-11498

[170] E. Dur, O.M. Cora and M. Koc, *Int. J. Hydrogen Energy*, **2011**, 36, 7162-7173

[171] C. Choe, H. Choi, W. Hong and J.-J. Lee, *Int. J. Hydrogen Energy*, **2011**,

[172] L. Wang, J. Sun, J. Sun, Y. Lv, S. Li, S. Ji and Z. Wen, *J. Power Sources*, **2012**, 199, 195–200

[173] L. Wang, J. Sun, P. Li, J. Sun, Y. Lv, B. Jing, S. Li, S. Ji and Z. Wen, *Int. J. Hydrogen Energy*, **2012**,

[174] H. Zhang, G. Lin, M. Hou, L. Hu, Z. Han, Y. Fu, Z. Shao and B. Yi, *J. Power Sources*, **2012**, 198, 176-181

[175] R.N.J. K. Natesan, *Surf. Coat. Technol.*, **1987**, 33, 341-351

[176] Y. Hung, H. Tawfik and D. Mahajan, *J. Power Sources*, **2009**, 186, 1, 123-127

[177] K. Sasaki, T. Tsutsumi and N. Takada, *Japanese Journal of Applied Physics*, **2011**, 50, 08KE05

[178] K. Feng, Y. Shen, H. Sun, D. Liu, Q. An, X. Cai and P.K. Chu, *Int. J. Hydrogen Energy*, **2009**, 34, 16, 6771-6777

[179] K. Feng, X. Cai, H. Sun, Z. Li and P.K. Chu, *Diam. Relat. Mater.*, **2010**, 19, 11, 1354-1361

[180] W. Jin, K. Feng, Z. Li, X. Cai, L. Yu and D. Zhou, *J. Power Sources*, **2011**, 196, 10032–10037

[181] S. Kitta, H. Uchida and M. Watanabe, *Electrochim. Acta*, **2007**, 53, 4, 2025–2033

[182] S. Joseph, J.C. McClure, R. Chianelli, P. Pich and P.J. Sebastian, *Int. J. Hydrogen Energy*, **2005**, 30, 12, 1339-1344

[183] S. Joseph, J.C. McClure, P.J. Sebastian, J. Moreira and E. Valenzuela, *J. Power Sources*, **2008**, 177, 1, 161-166

[184] Y. Show, *Surf. Coat. Technol.*, **2007**, 202, 1252-1255

[185] T. Fukutsuka, T. Yamaguchi, S.-I. Miyano, Y. Matsuo, Y. Sugie and Z. Ogumi, *J. Power Sources*, **2007**, 174, 1, 199-205

[186] C.-Y. Chung, S.-K. Chen, P.-J. Chiu, M.-H. Chang, T.-T. Hung and T.-H. Ko, *J. Power Sources*, **2008**, 176, 1, 276-281

[187] C.-Y. Chung, S.-K. Chen, T.-S. Chin, T.-H. Ko, S.-W. Lin, W.-M. Chang and S.-N. Hsiao, *J. Power Sources*, **2009**, 186 393–398

[188] P. Yi, L. Peng, L. Feng, P. Gan and X. Lai, *J. Power Sources*, **2010**, 195, 20, 7061-7066

[189] M.M. Larijani, M. Yari, A. Afshar, M. Jafarian and M. Eshghabadi, *Journal of Alloys and Compounds*, **2011**, 509, 7400–7404

[190] T. Wang, J. He, D. Sun, Y. Guo, Y. Ma, Y. Hu, G. Li, H. Xue, J. Tang and X. Sun, *J. Power Sources*, **2011**, 196, 22, 9552-9560

[191] M.H. Fronk and J.S.H. R.L. Borup, B.K. Brady, K.M. Cunningham, *US Patent, 6,372,376,* **1999**

[192] M.C. Kimble and E.B.A. A.S. Woodman, *AESF SUR/FIN Proceedings*, **1999**

[193] N. Cunningham, D. Guay, J.P. Dodelet, Y. Meng, A.R. Hlil and A.S. Hay, *J. Electrochem. Soc.*, **2002**, 149, 7, 905-911

[194] J.G. Gonzalez-Rodriguez, M.A. Lucio-Garcia, M.E. Nicho, R. Cruz-Silva, M. Casales and E. Valenzuela, *J. Power Sources*, **2007**, 168, 184–190

[195] D.G. Teer, *5,556,519,* **1996**

[196] K. Feng, Z. Li, H. Sun, L. Yu, X. Cai, Y. Wu and P.K. Chu, *J. Power Sources*, **2013**, 222, 351-358

[197] D.G. Teer, D. Camino and A.H.S. Jones, *WO 1999027893,* **1997**

[198] J. Stallard, *PhD Thesis*, Nottingham University,

[199] http://www.testbourne.com/,

[200] N.D. Nam, J.G. Kim and W.-S. Hwang, *Thin Solid Films*, **2009**, 517, 4772-4776

[201] R. Tian and J. Sun, *Int. J. Hydrogen Energy*, **2011**, 36, 6788-6794

[202] B. Wu, G. Lin, Y. Fu, M. Hou and B. Yi, *Int. J. Hydrogen Energy*, **2010**, 35, 13255 - 13261

[203] O. Lavigne, C. Alemany-Dumont, B. Normand, M.H. Berger, C. Duhamel and P. Delichére, *Corros. Sci.*, **2011**, 53, 2087-2096

[204] http://www.bio-logic.info/potentiostat/fct.html, **2012**

[205] M.A. Pimenta, S.D.M.B. A. Jorio, A.G.S. Filho, G. Dresselhaus, J.H. Hafner, C.M. Lieber, R. Saito and M.S. Dresselhaus, *Phys. Rev.B*, **2001**, 64, 041401, 1-4

[206] XPS Database, http://www.lasurface.com/database/elementxps.php, **2013**

[207] A. Oyarce, *Technoport - Hydrogen session*, Trondheim, Norway, **2012**

[208] E.M. Gabreab, G. Hinds, S. Fearn, D. Hodgson, J. Millichamp, P.R. Shearing and D.J.L. Brett, *J. Power Sources*, **2014**, 245, 1014 - 1026

[209] O. Lavigne, C. Alemany-Dumont, B. Normand, S. Berthon-Fabry and R. Metkemeijer, *Int. J. Hydrogen Energy*, **2012**, 37, 14, 10789–10797

[210] J. Menghani, K.B. Pai, M.K. Totlani and N. Jalgoankar, *Proceedings of the World Congress on Engineering*, London, U.K., **2010**

[211] Y. Fu, M. Hou, G. Lin, J. Hou, Z. Shao and B. Yi, *J. Power Sources*, **2008**, 176, 282-286

[212] US Department of Energy, Technical Plan - Fuel Cells, Accessed June 2012, http://www1.eere.energy.gov/hydrogenandfuelcells/mypp/,